1. Report No. **FHWA/LA.09/450**	2. Government Accession No.	3. Recipient's Catalog No.
4. Title and Subtitle **Evaluation of the Base/Subgrade Soil under Repeated Loading: Phase 1 – Laboratory Testing and Numerical Modeling of Geogrid Reinforced Bases in Flexible Pavement**	5. Report Date **October 2009** 6. Performing Organization Code	
7. Author(s) **Murad Y. Abu-Farsakh, Ph.D., P.E., and Munir Nazzal Ph.D., P.E.**	8. Performing Organization Report No.	
9. Performing Organization Name and Address **Louisiana Transportation Research Center** **4101 Gourrier Avenue** **Baton Rouge, LA 70808**	10. Work Unit No. 11. Contract or Grant No. **LTRC Number: 05-5GT** **State Project Number: 736-99-1312**	
12. Sponsoring Agency Name and Address **Louisiana Transportation Research Center** **4101 Gourrier Avenue** **Baton Rouge, LA 70808**	13. Type of Report and Period Covered **Interim Report** **Aug 2003- May 2007** 14. Sponsoring Agency Code	
15. Supplementary Notes **Conducted in Cooperation with the U.S. Department of Transportation, Federal Highway Administration**		

16. Abstract

This report documents the results of a study that was conducted to characterize the behavior of geogrid reinforced base course materials. The research was conducted through an experimental testing and numerical modeling programs. The experimental testing program included performing different laboratory tests to evaluate the effect of various factors on the performance geogrid reinforced base course materials. Finite element models were also developed to investigate the benefits of placing geogrids within the base course layer in a flexible pavement structure. The results of the experimental testing demonstrated that the inclusion of the geogrid reinforcement layer(s) improved the compressive strength and stiffness of base course materials under static loading. This improvement was more pronounced at higher strain levels. Furthermore, the results showed that the geogrid significantly reduced the base course material permanent deformation under cyclic loading, but it did not show appreciable effect on their resilient deformation. The finite modeling program showed that the geogrid reinforcement reduced the lateral, vertical, and shear strains within the base course and subgrade layers. Furthermore, the geogrid had an appreciable reduction in permanent deformation for pavement sections built on top of weak subgrade soils with medium to thin base layer thickness, with the thin base layer thickness showing greater values of improvement. However, negligible to modest reinforcement effect on permanent deformation was obtained for sections having a firm subgrade or thick base layer thickness. The geogrid reinforcement had modest to high values of improvement in fatigue life of pavement structure.

17. Key Words **Geogrid reinforcement, Crushed limestone, Base coarse layer, Triaxial test, Resilient modulus, Permanent deformation, Finite element analysis, Statistical analysis.**		18. Distribution Statement **Unrestricted. This document is available through the National Technical Information Service, Springfield, VA 21161.**	
19. Security Classif. (of this report) **Unclassified**	20. Security Classif. (of this page) **Unclassified**	21. No. of Pages **141**	22. Price

Evaluation of the Base/Subgrade Soil under Repeated Loading: Phase I – Laboratory Testing and Numerical Modeling of Geogrid Reinforced Bases in Flexible Pavement

by

Murad Abu-Farsakh, Ph.D., P.E.
and
Munir Nazzal, Ph.D., P.E.

Louisiana Transportation Research Center
4101 Gourrier Avenue
Baton Rouge, LA 70808

LTRC Project No. 05-5GT
State Project No. 736-99-1312

conducted for

Louisiana Department of Transportation and Development
Louisiana Transportation Research Center

October 2009

ABSTRACT

This report documents the results of a study that was conducted to characterize the behavior of geogrid reinforced base course materials. The research was conducted through an experimental testing and numerical modeling programs. The experimental testing program included performing different laboratory tests to evaluate the effect of various factors on the performance geogrid reinforced base course materials. Finite element models were also developed to investigate the benefits of placing geogrids within the base course layer in a flexible pavement structure. The results of the experimental testing demonstrated that the inclusion of the geogrid reinforcement layer(s) improved the compressive strength and stiffness of base course materials under static loading. This improvement was more pronounced at higher strain levels. Furthermore, the results showed that the geogrid significantly reduced the base course material permanent deformation under cyclic loading, but it did not show appreciable effect on their resilient deformation. The finite modeling program showed that the geogrid reinforcement reduced the lateral, vertical, and shear strains within the base course and subgrade layers. Furthermore, the geogrid had an appreciable reduction in permanent deformation for pavement sections built on top of weak subgrade soils with medium to thin base layer thickness, with the thin base layer thickness showing greater values of improvement. However, negligible to modest reinforcement effect on permanent deformation was obtained for sections having a firm subgrade or thick base layer thickness. The geogrid reinforcement had modest to high values of improvement in fatigue life of pavement structure.

ACKNOWLEDGMENTS

This research project was funded by the Louisiana Department of Transportation and Development (LADOTD) and the Louisiana Transportation Research Center (LTRC). The comments and suggestions of Mark Morvant, associate director of research, and Zhongjie "Doc" Zhang, pavement and geotechnical administrator of LTRC, are gratefully acknowledged.

IMPLEMENTATION STATEMENT

Experimental and numerical modeling programs were conducted to characterize the behavior of geogrid reinforced base course materials for application to flexible pavements. The experimental testing program included performing laboratory tests to evaluate the performance of geogrid reinforced base course specimens. The finite element modeling was used to investigate the benefits of placing geogrids within the base course layer in a flexible pavement structure. The results of this study demonstrated the potential benefits of reinforcing the base aggregate layer in flexible pavements through improving the strength and stiffness of the base course material, reducing the pavement's permanent deformation (rutting) and fatigue cracking under cyclic loading. The improvement due to geogrid reinforcement was also assessed using a mechanistic empirical approach.

Analyses of test results and numerical modeling enabled researchers to identify the best location of geogrid layer and to develop models that can predict the geogrid benefits as a function of base layer thickness, geogrid modulus, and subgrade CBR value. The findings of this research study can be implemented in the design of flexible pavements built on top of soft subgrades with resilient modulus $M_r < 2000$ psi by reinforcing the base aggregate layers with one layer of geogrid, especially in cases where it is difficult to stabilize/treat the soft subgrade soil with cement or lime. The use of geogrids with elastic tensile modulus at 2 percent strain, $E_{2\%} \geq 250$ lb/ft, is recommended. The geogrid layer should be placed at the base-subgrade interface for pavements with a base thickness of less than 18 in. and at the middle of the base aggregate layer for base thicknesses equal or greater than 18 in.

TABLE OF CONTENTS

LIST OF TABLES

LIST OF FIGURES

INTRODUCTION

The United States of America has one of the largest highway systems in the world with over 3.9 million miles of roads as of the year 2004. Its highways have reached almost 2.7 trillion vehicle-miles in 2000. This is equivalent to 7.4 billion vehicle-miles of travel every day. Truck travel (single-unit and combinations) has increased by 231 percent from 1970 to 2004, while the combination truck travel has increased by 285 percent to account for 4.9 percent of the total annual vehicle-miles of travel versus 3.2 percent in 1970 *[1]*.

The inadequacy of many of the existing roads due to the rapid growth in traffic volume and the escalating costs of materials and energy provide motivation for exploring alternatives to existing methods of building and rehabilitating roads. Stabilizing paved and unpaved roads with fabrics offers one such alternative. In recent years, polymer geogrids have been proposed and used to improve the performance of paved roadways. Many experimental and analytical studies have been conducted to validate the improvements associated with geogrid reinforcement of roadways. It was reported that the use of geogrid reinforcement of pavement structures has three main benefits: (1) help in construction over soft subgrades, (2) improvement or extension of the pavement's projected service life, and (3) reduction of the pavement structural cross section for a given service life.

Several design methods have been proposed for flexible pavements with geogrid reinforced unbound base aggregate layer. These design methods were based on empirical or analytical approaches. Empirical design methods are usually based on obtaining a performance level from a laboratory model test, which is then extrapolated to the field conditions for application in the design *[2]*. This makes these methods limited to the conditions associated with the experiments of the study. The geogrid reinforced pavement design methods based on analytical solutions do not address all the variables (location of geogrid, stiffness of geogrid, base course layer thickness, and strength/stiffness of subgrade, etc.) that affect the performance of these pavements, which have been validated by experimental data *[3]*.

Given the complex nature of a geogrid reinforced flexible pavement and the introduction of a new variables associated with the reinforcement, a mechanistic procedure is needed for providing a design procedure expressed in terms of material properties of the pavement layers (asphalt concrete, base, and subgrade) and the geogrid materials

composing the pavement system. The mechanistic design procedure should consider the influencing variables on the performance of geogrid reinforced flexible pavements.

In order to develop such mechanistic design procedures for reinforced pavement structures, a better understanding and characterization of the geogrid reinforced mechanisms should be established. In addition, the factors that affect the geogrid reinforced pavement structure should be investigated and evaluated.

This study aimed at evaluating the benefits of geogrid reinforcement of the base course aggregate layer in a flexible pavement structure through conducting extensive experimental testing and numerical modeling programs. The experimental testing included small-scale laboratory testing of geogrid reinforced base aggregate specimens and large-scale in-box cyclic plate load testing of geogrid base reinforced pavement sections. The numerical modeling included finite element analyses to evaluate the effect of geogrid stiffness and location, thickness of the base course layer, and strength of the subgrade material on the performance of geogrid reinforced flexible pavement structures.

This interim report will present the results of small-scale testing and finite element numerical modeling. The results of large-scale testing on geogrid base reinforced pavement sections will be presented in another report.

OBJECTIVE

The main objective of this research study is (1) to evaluate the behavior of geogrid reinforced base course aggregate layer and (2) to investigate the effects of different variables and parameters that significantly influence the performance/benefit of geogrid reinforced base course layer in a flexible pavements structure through experimental testing and numerical modeling. This part of the study has the following specific objectives:

1. Assess the behavior of geogrid reinforced unbound granular base course material under monolithic and cyclic loading, and evaluate the following factors:
    a. geogrid stiffness
    b. geogrid location
    c. number of geogrid layers
2. Assess the benefits of reinforcing the base course layer in a flexible pavement structure with geogrid, and evaluate the influence of the different variables on the degree of improvement in the performance of pavement structures. These variables include:
    a. strength of the subgrade soil
    b. thickness of the base course layer
    c. stiffness and location of the geogrid layer

SCOPE

The stated objectives of this research study were achieved through conducting both experimental testing and numerical modeling programs. The experimental testing program included conducting small-scale laboratory triaxial testing on geogrid reinforced base aggregate specimens and large-scale in-box cyclic plate load testing on geogrid base reinforced pavement sections.

This report will discuss only the results of small-scale testing. This testing include the following variables: base course material type, geogrid type, and geogrid layer arrangements. Different laboratory tests were conducted to investigate the performance of unreinforced and reinforced base aggregate specimens, which included monotonic compression triaxial, resilient modulus repeated loading triaxial (RLT) tests, and single-stage RLT tests.

The numerical modeling program included developing finite element models using ABAQUS software for typical pavement sections that were used to evaluate the effect of the location of the reinforcement material, the thickness of the base course layer, the stiffness of the reinforcement material, and the strength of the subgrade material on the geogrid reinforced flexible pavements.

METHODOLOGY

General Consideration

Flexible Pavement Structures

A conventional flexible pavement structure consists of a surface layer of hot mix asphalt and a base course layer of granular materials built on top of a subgrade layer. The two main structural failure mechanisms for flexible pavements are permanent deformation (rutting) and fatigue cracking. These two failure modes are shown in Figure 1. Rutting is the result of an accumulation of irrecoverable strains in the various pavement layers. For thin to moderately thick pavements, subgrade and granular base layers contribute most to rutting of a pavement. Fatigue cracking has been defined as the phenomenon of fracture under repeated or fluctuating stress having a maximum value generally less than the tensile strength of the material *[4]*.

Base course layer can be the cause of pavement failures due to inadequate provision of support to upper layers or by being insufficiently stiff, such that they fail to transfer the load uniformly to the subgrade, leading to localized overloading of the subgrade, and resulting in excessive pavement rutting. Therefore, when constructing a pavement structure on a weak subgrade soil layer, it may be required to increase the thickness of base layers or use good quality base course material. However, the depletion of high quality aggregates is at a rapid pace as a consequence of the increasing demands on highway systems. In addition, there are usually limitations on the thickness of the pavement structures. These problems provide a motivation for exploring alternatives to existing methods of building and rehabilitating roads. Geogrid reinforcement in base course layer offers one such alternative. Geogrids have been studied and used for the last two decades as reinforcement in the base course layer of flexible pavements primarily since its application improves the performance of base course material layer and consequently may extend the service life of flexible pavements.

Response of Base Course Material under Repeated Loads

Unbound granular base course material as well as other pavement materials exhibit a combination of resilient strains, which are recovered after each load cycle, and permanent strains, which accumulate with every load cycle. Even at small stresses, resilient and permanent strains can arise. In pavement design it is anticipated that the resilient deformation increases more than the permanent deformation as more load cycles are

applied, such that after a large number of cycles the deformation under each cycle is nearly recoverable *[5]*.

(a) **(b)**

Figure 1
Distresses in flexible pavements (a) rutting (b) fatigue cracking

Therefore, the resilient modulus has gained recognition by the pavement community as a good property that describes the base course materials. The Mechanistic Empirical Pavement Design Guide (MEPDG) has adopted the use of the resilient modulus of base layers as a material property in characterizing pavements for their structural analysis and design *[1]*. However, recent studies showed that resilient modulus alone cannot properly characterize base course materials since the base course materials depend on resilient modulus and permanent deformation properties that are affected by other factors, such as environmental and traffic conditions *[6]*, *[7]*, *[8]*, and *[9]*. These properties are typically determined in a RLT test.

The factors affecting both the resilient modulus and permanent deformation properties of granular materials have been studied by many researchers. These include state of stress, the number of load applications, moisture content, stress history, density, and particle size distribution *[9]*-*[31]*.

Geogrid Reinforced Base Course Materials

Currently, three main geosynthetic families of products are used as soil reinforcement: geogrids, geotextiles, and synthetic fibers. The most commonly used type of geosynthetics for reinforcement of base course layers in flexible pavements is geogrid.

The key feature of geogrids is that the apertures are large enough to allow soil strike through from one side of the geogrid to the other. The ribs of the geogrids are often stiff compared to the fibers of geotextiles. The rib strength and junction strength are important parameters. The reason for this is that the soil strike-through within the apertures bears against the transverse ribs, which transmit the forces to the longitudinal ribs via the junctions.

The benefits of applying geogrid reinforcement to the base course layers of flexible reinforcement have been addressed by many researchers during the last two decades. Validating these benefits was accomplished either through indoor (reduced-scale) testing, or outdoor (large-scale) testing. The results of these studies showed that geogrids were able to extend the service lives for reinforced sections by reducing the amount of permanent deformation (rutting) in these sections. The increase in service life of pavement structure has been usually defined using the Traffic Benefit Ratio (TBR). The TBR is defined as the ratio of the number of load cycles needed to achieve a particular rut depth in reinforced section to that of an unreinforced section of identical thickness, material properties, and loading characteristics. The results of these studies also showed that the required base course thickness for a given design may be reduced when a geogrid is included in their design This reduction is usually defined by the Base Course Reduction (BCR) factor, which is defined as the reinforced base thickness divided by the unreinforced base thickness for a given traffic level.

Results of experimental studies demonstrated that geogrid base reinforcement benefits were dependent on a number of factors. These include the location of the geogrid layer within the base course layer, which depends on the base course thickness, strength/stiffness of subgrade layer, and the geometric and engineering properties of the geogrids *[32]*, *[33]*, *[34]*, *[35]*, *[36]*, *[37]*, and *[38]*.

Geogrid Reinforcement Mechanism

Previous studies involving geogrid reinforcement of base course layer have identified three fundamental reinforcement mechanisms: lateral confinement, increased bearing capacity, and tension membrane effect. These mechanisms are described next.

Lateral Confinement Mechanism. The lateral restraint is considered the primary function of geogrid reinforcement, and it develops mainly through shear interaction of the base course layer and geogrid layer or layers contained in or at the bottom of base aggregates as shown in Figure 2. By laterally restraining the soil, four components of

reinforcement are potentially achieved. The first component is related to direct prevention of lateral spreading of the base course. The cohesion-less materials that make up the base have little tensile resistance and generally depend on the subgrade to provide lateral restraint. In weak subgrades, very little lateral restraint is provided. Thus, the aggregate particles at the bottom of the base tend to move apart. The placement of geogrids layer or layers in the base course allows for shear interaction to develop between the aggregate and the geogrid as the base attempts to spread laterally; this most likely comes from particles of granular material becoming wedged in the aperture of the geogrids Tensile load is effectively transmitted from the base course aggregate to the geogrid since the geogrid is considerably stiffer in tension compared to aggregate; consequently this will reduce the developed lateral tensile strain.

The second component of the lateral restraint mechanism results from the increase in stiffness of the base course aggregate when adequate interaction develops between the base and the geogrids. The shear stress developed between the base course, aggregate, and geogrids provides an increase in lateral stress within the base *[36]*. This tends to increase in the modulus of the base course material *[39]*. This increase in stiffness of this layer results also in lower vertical strains in the base.

The third lateral reinforcement component results from an improved vertical stress distribution on the subgrade. The presence of geogrid layer in the base can lead to a change in the state of stress and strain in the subgrade. For layered systems, a weaker subgrade material lies beneath the base and an increase in the stiffness of base course layer results in an improved vertical stress distribution on the subgrade. In general, the vertical stress in the base and subgrade layer directly beneath the applied load should decrease as the base layer stiffness increases, such that the vertical stress on the subgrade will become more widely distributed.

Finally, the fourth reinforcement mechanisms results from the reduction of shear stress in subgrade soil. It is expected that shear stress transmitted from base course to the subgrade would decrease as shearing of the base transmits tensile load to the reinforcement.

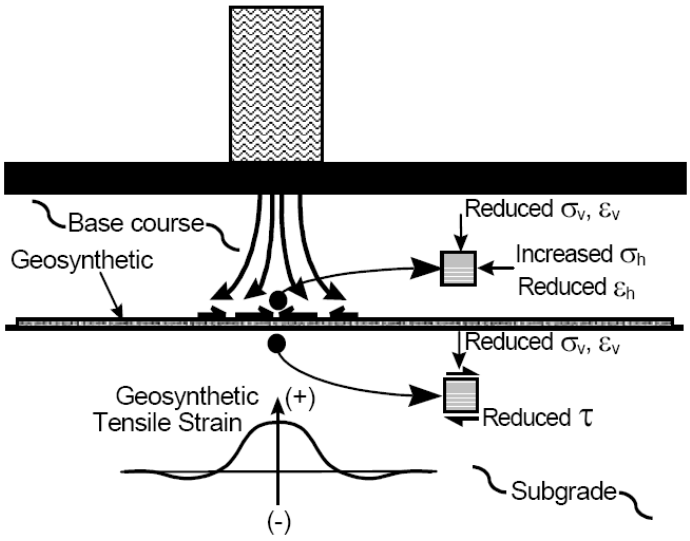

(a) Reinforcement at base/subgrade interface

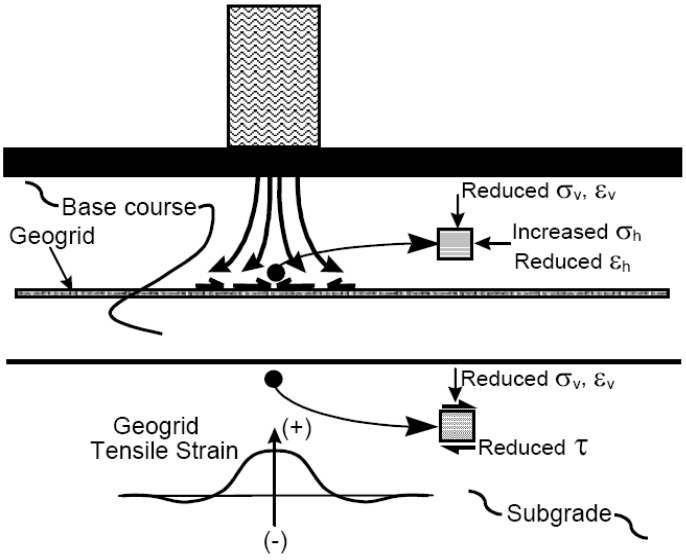

(b) Reinforcement in base coarse layer

Figure 2
Illustration of lateral restraint reinforcement mechanisms

Increase of the Bearing Capacity Mechanism. The improved bearing capacity is achieved by shifting the failure envelope of the pavement system from the relatively weak subgrade to the relatively stiff base layer as illustrated in Figure 3. The bearing failure model of subgrade may change from punching failure without reinforcement to general failure with ideal reinforcement. Binquet and Lee initially established this finding *[4]*.

Tension Membrane Mechanism. The tension membrane effect develops as a result of vertical deformation creating a concave shape in the tensioned geogrid layer; this is demonstrated in Figure 4. The vertical component of the tension membrane force can reduce the vertical stress acting on the subgrade. Some displacement is needed to mobilize the tension membrane effect. Generally, a higher deformation is required for the mobilization of tensile membrane resistance as the stiffness of the geosynthetic decreases. In order for this type of reinforcement mode to be significant, there is a consensus that the subgrade CBR should be less than 3 *[41]*.

Small-Scale Controlled Laboratory Studies

In order to better understand the reinforcement mechanisms acting in a large-scale reinforced soil structure, studies were also conducted to evaluate such mechanisms at a small-scale controlled laboratory environment *[42]*, *[43]*, *[44]*, *[45]*, *[46]* and *[47]*. These studies have investigated the effect of geosynthetics on the deformation and strength behavior of reinforced materials using both monotonic and cyclic triaxial tests. Gray and Al-Refeai conducted triaxial compression tests on dry reinforced sand using five different types of geotextile *[44]*. Test results demonstrated that reinforcement increased peak strength, axial strain at failure, and, in most cases, reduced post-peak loss of strength. At very low strain (< 1 percent), reinforcement resulted in a loss of compressive stiffness. Failure envelope of the reinforced sand showed a clear break with respect to the confining pressure. After the point of break, failure envelope for the reinforced sand paralleled the unreinforced sand envelope.

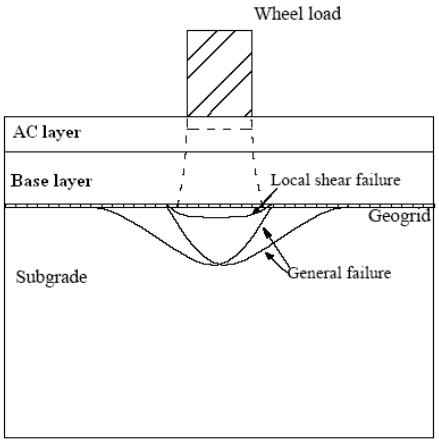

Figure 3
Improved bearing capacity

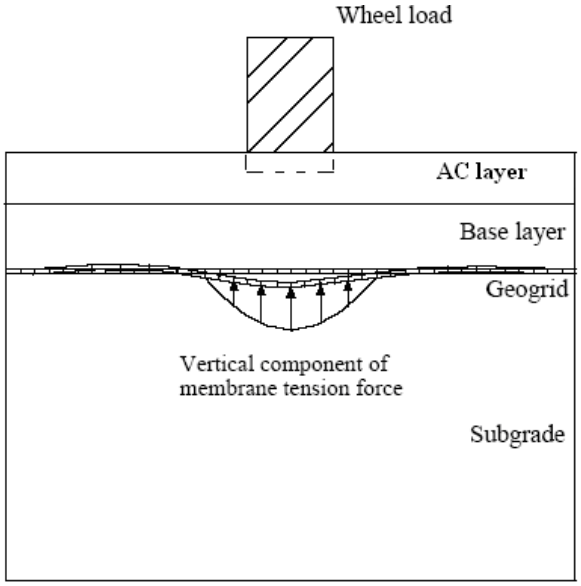

Figure 4
Tension membrane mechanism

Ashmawy et al. conducted monotonic and cyclic triaxial tests on geotextile-reinforced silt and sand samples that were 71 mm in diameter and 170 mm in length *[45]*. The results of these studies showed that the presence of geosynthetics significantly improved the strength of tested samples. In addition, the geosynthetic layer tended to reduce the accumulated plastic strains under cyclic loading. Ashmawy et al. investigated the effects of reinforcement layers spacing and reinforcement material properties on the achieved improvement. Their results showed that the amount of improvement depends on the spacing of the geotextile layers and, to a lesser extent, on the geotextile and interface properties *[45]*.

Moghaddas-Nejad and Small also conducted drained repeated triaxial compression tests on two granular materials (sand and fine gravel) reinforced by geogrid *[46]*. The geogrid layer was placed at the mid-height of the sample, which was 200 mm in diameter and 400 mm in length. The results of this study showed that for a particular confining stress, the effect of a geogrid on the reduction in permanent deformation increases rapidly with an increase in the deviator stress until a peak is reached and then decreases gradually. However, the geogrid did not have a considerable effect on the resilient deformation of the tested materials.

Perkins et al. have performed cyclic triaxial tests on reinforced and unreinforced aggregate specimens *[47]*. The specimens were 600 mm in height and 300 mm in

diameter and were compacted inside a rigid compaction mold using a vibrating plate compactor. For the reinforced specimens, a single layer of reinforcement was placed at mid-height of the sample. Four different types of reinforcements were used in the tests (two geogrids, one geotextile, and one geocomposite). Their findings supported the previous work reported by Moghaddas-Nejad and Small, where it showed that the reinforcement does not have an effect on the resilient modulus properties of unbound aggregates, while it also showed an appreciable effect on the permanent deformation properties of unbound aggregate as measured in repeated load permanent deformation tests *[46]*. Perkins et al. also indicted that the relatively poor repeatability seen in permanent deformation tests made it difficult to distinguish between tests with different reinforcement products *[47]*. Their results also showed that the reinforcement did not have an appreciable effect on the permanent deformation until a mobilized friction angle of approximately 30 degrees is reached.

Numerical Modeling of Geogrid Reinforced Flexible Pavements

Several numerical studies were performed by other researchers to analyze pavement sections and assess the improvements due to the geosynthetic reinforcement *[38]*, *[41]*, *[48]*, *[49]*, *[50]* and *[51]*. Most of the numerical studies were performed using the finite element method. Different constitutive models were used to determine the model that is most capable of representing the stresses and deformations in a reinforced pavement. Table 1 summarizes the numerical studies that were reported in literature to investigate reinforced flexible pavement and major features associated with each study.

Table 1
Summary of finite element studies on geosynthetic reinforced pavements

	Author									
	Barksdale et al. (1989)	Burd and Houlsby (1986)	Burd and Brocklehurst (1990)	Burd and Brocklehurst (1992)	Dondi (1994)	Miura et al. (1990)	Wathugala et al. (1996)	Perkins (2001)	Leng and Gabr (2003)	Kwon et al. (2005)
Analysis type	Axi-symmetric	Plane strain	Plane strain	Plane strain	Three-dimensional	Axi-symmetric	Axi-symmetric	Three-dimensional	Axi-symmetric	Axi-symmetric
AC constitutive model	Isotropic, nonlinear elastic	None	None	None	Isotropic, linear elastic	Isotropic, linear elastic	Isotropic, D.P.	Transversely isotropic elastic perfectly plastic	None	Isotropic, linear elastic
AC thickness (mm)	Variable	None	None	None	120	50	89	75	None	76
Base constitutive model	Anisotropic, linear elastic	Isotropic, lastoplastic, Matusoka	Isotropic, elastoplastic, Matusoka	Isotropic, elastoplastic, Matusoka	Isotropic, D.P.	Isotropic, linear elastic	Isotropic, D.P.	Bounding Surface model	Isotropic, D.P.	Nonlinear Elastic
Base thickness (mm)	Variable	75	300	300	300	150	140	300	Variable	254
Geosynthetic constitutive model	Linear elastic	Isotropic, linear elastic	Isotropic, linear elastic	Isotropic,linear elastic	Isotropic, linear elastic	Isotropic, linear elastic	Isotropic, von Mises	orthotropic linear elastic	Isotropic linear elastic perfectly plastic	Isotropic, linear elastic
Geosynthetic element type	Membrane	Membrane	Membrane	Membrane	Membrane	Truss	Solid continuum	Membrane	Membrane	Membrane
Geosynthetic thickness (mm)	None	None	None	None	None	None	2	2	3	1.27
Interface elements and model	Linear elastic-perfectly plastic	None	None	Elastoplastic, Mohr-Coulomb	Elastoplastic, Mohr-Coulomb	Linear elastic joint element	None Isotropic, elastoplastic,	Elastoplastic, Mohr-Coulomb	Elastoplastic, Mohr-Coulomb	linear elastic spring interface element
Subbase constitutive model	None	None	None	None	None	Isotropic, linear elastic	HiSS δo	None	None	None
Subbase thickness (mm)	None	None	None	None	None	200	165	None	None	None
Subgrade constitutive model	Isotropic, non-linear elastic	Von Mises	Von Mises	Von Mises	Cam-Clay	Isotropic, linear elastic	HiSS δo	Bounding Surface model	D.P.	Isotropic, linear elastic
Load application	Monotonic	Monotonic, footing width =75mm	Monotonic, footing width = 500 mm	Monotonic, footing width = 500 mm	Monotonic, two rectangular areas, 240 mm × 180 mm	Monotonic, 200 mm diameter plate	Single cycle, peak pressure=725 kPa on 180 mm diameter plate	Montonic,304 mm plate	Montonic,304 mm plate	Monotonic, a pressure of 828 on 200 mm circular area

D.P.: Drucker Prager Model

Experimental Testing Program

Experimental testing program was conducted to evaluate the effects of the different factors on the performance of geogrid reinforced base course granular materials. These factors include the geogrid stiffness, geogrid location, number of geogrid layers, and the effect of state of stress and moisture content. Two types of triaxial tests were used for this evaluation, namely Static Triaxial Compression (STC) tests and Repeated Loading Triaxial (RLT) tests. The following sections provide detailed information on the materials used and their properties. They also highlight the laboratory procedures for the triaxial tests performed.

Materials

Base Course Materials. Experimental testing was performed on two types of crushed limestone aggregate materials used in the construction of base course layers in Louisiana: crushed limestone I, which is Kentucky limestone obtained from Martin Marietta Company and crushed limestone II which is Mexican limestone obtained from Vulcan Material Company. Standard compaction, specific gravity (G_s), absorption, and California Bearing Ratio (CBR) tests were performed on the base materials in accordance with ASTM standards D 792, D 698, D 570, and D 1883, respectively.

Geogrid Reinforcement

The reinforcement materials used in this study included five different types of biaxial geogrids, namely BX-6100, BX-1100, BX-6200, BX-1200, and BX-1500, where BX-6100 represents the lowest stiffness geogrid and BX-1500 represents the stiffest geogrid. These geogrids are manufactured of a stress resistant polypropylene material and are typically used to reinforce a base course layer in pavement structures. The physical and mechanical properties of these products as reported by the manufacturer are presented in Table 2 *[52]*. Type I, II, III, IV, and V will be used hereafter in this report to refer to BX-6100, BX-1100, BX-6200, BX-1200, and BX-1500, respectively.

Testing Setup

All triaxial tests were performed using the Material Testing System (MTS) 810 machine with a closed loop and a servo hydraulic loading system. The applied load was measured using a load cell installed inside the triaxial cell. Placing the load cell inside the triaxial chamber eliminates the push-rod seal friction and pressure area errors, which results in reducing the testing equipment error. An external load cell is affected by changes in confining pressure and by load rod friction, and the internal load cell therefore gives

more accurate readings. The capacity of the load cell used was ± 22.25 kN (± 5000 lbf.). The axial displacement measurements were made using two Linearly Variable Differential Transducers (LVDT) placed between the top platen and base of the cell to reduce the amount of extraneous axial deformation measured compared to external LVDTs. Air was used as the confining fluid to the specimens. Figure 5 depicts a picture of the testing setup used in this study.

Table 2
Physical and mechanical properties of geogrids

Geogrid	Tensile Stiffness @ (strain %)[a]		Aperture Dimension		Flexural Stiffness [b]
	MD (lb/ft)	CMD (lb/ft)	MD (in.)	CMD (in.)	(g-cm)
BX-1500	580 (2%) 1200 (5%)	690 (2%) 1370 (5%)	1	1.3	2000
BX-1200	410 (2%) 810 (5%)	650 (2%) 1340 (5%)	1	1.3	750
BX-6200	380 (2%) 720 (5%)	510 (2%) 1000 (5%)	1.3	1.3	250
BX-1100	280 (2%) 580 (5%)	450 (2%) 920 (5%)	1	1.3	750
BX-6100	250 (2%) 550 (5%)	380 (2%) 720 (5%)	1.3	1.3	250

[a] Measured in accordance with ASTM standard method for determining tensile properties of geogrids ASTM D6637 [52].
[b] Measured in accordance with ASTM Standard Test Method for determining stiffness of non-woven fabrics using the cantilever test ASTM D-5732-95 *[52]*.
MX: Machine direction.
CMD: Cross- machine direction.

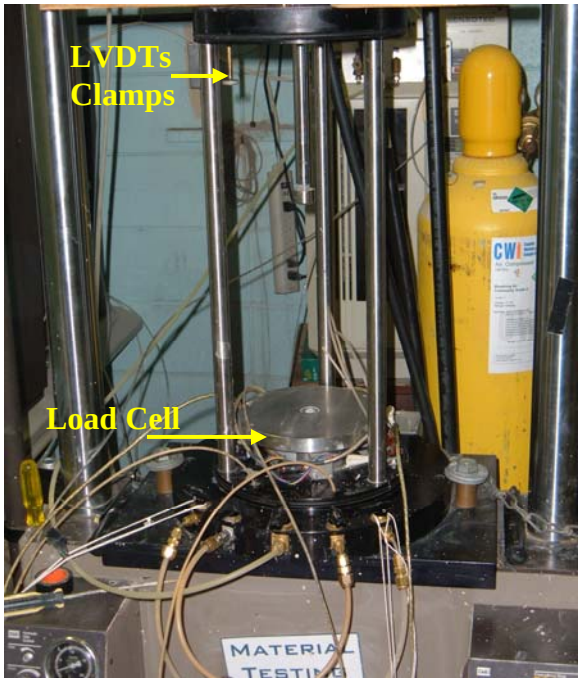

Figure 5
MTS triaxial testing machine

Sample Size

Dimensions of the sample tested in the triaxial experiment are based on the maximum particle size of its material. AASHTO recommends that for untreated granular base material, the tested sample should have a diameter greater than five times the maximum particle size of that material. In addition, other studies recommend the use of samples with 6-in. (150 mm) diameters and that are 12 in. (300 mm) in height for a base material with a maximum particle size greater than 0.75 in. (19 mm) (NCHRP, 2004). Since the base course material used in this study had a maximum particle size of 0.75 in. (19.0 mm), all samples were prepared with 6-in. (150 mm) diameters and 12 in. (300 mm) in height.

Sample Preparation

AASHTO recommends that a split mold be used for compaction of granular materials. Therefore, all samples were prepared using a split mold with an inner diameter of 6 in. (150 mm) and a height of 12 in. (350 mm). The material was first oven dried at a pre-specified temperature and then mixed with water at the optimum moisture content. The achieved water contents were within ± 0.5 percent of the target value. The material was then placed within the split mold and compacted using a vibratory compaction device to achieve the maximum dry density measured in the standard Proctor test. To achieve a

uniform compaction throughout the thickness, samples were compacted in six 2-in. (50 mm) layers. Each layer was compacted until the required density was obtained; this was done by measuring the distance from the top of the mold to the top of the compacted layer. The smooth surface on top of the layer was lightly scratched to achieve good bonding with the next layer. The achieved dry densities of the prepared samples were within ±1 percent of the target value. Samples were enclosed in two latex membranes with a thickness of 0.12 in. (0.305 mm). Figure 6 illustrates the preparation procedure of crushed limestone samples. For reinforced samples, the geogrid was placed horizontally between layers at the desired locations. Four different arrangements of reinforcement were investigated in this study namely single layer placed at the sample mid-height (middle arrangement), single layer placed at the upper one-third of the sample height (upper one-third arrangement), single layer placed at the lower one-third of the sample height (lower one-third arrangement), and two layers placed at one and two thirds of the sample height (double arrangement). A sketch describing the four reinforcement arrangements investigated in this study is shown in Figure 7.

Monotonic Triaxial Compression Tests

Although the repeated load triaxial tests are considered more representative of the actual performance in the road, the monotonic triaxial compression tests can provide valuable parameters needed to evaluate strength and stiffness of pavement materials. Furthermore, it is commonly thought that safe stress states for a pavement material are related to their ultimate shear strength.

Monotonic triaxial compression tests were conducted using a strain rate less than 10 percent strain per hour. This rate was chosen to ensure that no excess pore water was developed during testing. The drained triaxial compression tests were performed under 3 psi (21 kPa) confinement pressures on both unreinforced and reinforced samples. In each test, the sample was loaded to a strain level of one percent, unloaded, and then reloaded to failure.

The value of the confinement pressure was chosen to match the field measurement of the lateral confining pressure within the base course layer as reported in different studies. Three replicate samples were tested for each case to ensure repeatability. Four response parameters were obtained from each triaxial test to quantitatively evaluate the improvement achieved due to reinforcement under monotonic loading. The parameters are: the secant elastic moduli at one percent strain level ($E_{s1\%}$), the secant elastic moduli at two percent strain level ($E_{s2\%}$), the ultimate shear strength (USS), and residual shear strength (RSS). These parameters were chosen to assess the reinforcement benefit on the

behavior of the tested material at different strain levels. Improvement factors IM-$E_{s1\%}$, IM-$E_{s2\%}$, IM-USS, and IM-RSS were then determined using the following equation:

$$\text{IM} = \frac{\text{parameter from reinforced sample}}{\text{parameter from unreinforced sample}} \quad (1)$$

Figure 6
Preparation and testing of crushed limestone sample

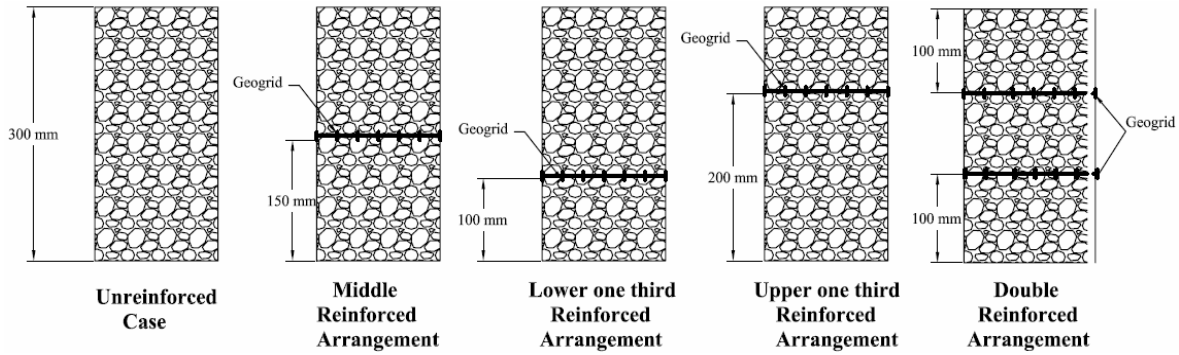

Figure 7
Reinforcement Arrangements investigated in this study

Resilient Modulus Tests

Resilient modulus tests were performed in accordance with AASHTO-T307 standard method for determining the resilient modulus of base course material *[53]*. In this test, a repeated axial cyclic stress with a haversine-shaped load-pulse and fixed magnitude was applied to 150 mm diameter cylindrical samples. The load pulse used in this study has a 0.1 sec. load duration and 0.9 sec. rest period as shown in Figure 8. The samples were first conditioned by applying 1,000 load cycles with a deviator stress of 93.0 kPa and a confining stress of 103.4 kPa to remove most irregularities on the top and bottom surfaces of the test sample. This is followed by a sequence of loading with varying confining and deviator stresses. The confining pressure is set constant, and the deviator stress is increased. Subsequently, the confining pressure is increased, and the deviator stress varied. The resilient and permanent deformations of the samples were measured during this test to calculate the resilient and plastic strains, respectively. The resilient modulus values are calculated at specified deviator stress and confining pressure values as the ratio of the cyclic stress to the measured resilient strain:

$$M_r = \frac{\sigma_{cyc}}{\varepsilon_r} \qquad (2)$$

where, σ_{cyc} is the maximum cyclic stress, and ε_r is the recoverable elastic strain.

In order to determine the resilient modulus parameters of unreinforced and reinforced samples, the average value of the resilient modulus for all stress sequence was first calculated. A regression analysis was then carried out to fit each test data to the generalized constitutive model given in equation (3), which was adopted by the new *Mechanistic-Empirical Design Guide [1]*.

$$M_r = p_a k_1 \left(\frac{\theta}{p_a} \right)^{k_2} \left(\frac{\tau_{oct}}{p_a} + 1 \right)^{k_3} \quad (3)$$

where, M_r is the resilient modulus p_a is the atmospheric pressure (101.3 kPa), $\theta = (\sigma_1 + \sigma_2 + \sigma_3)$, $\sigma 1$, $\sigma 2$, $\sigma 3$ are principal stress components, τ_{oct} is the octahedral shear stress defined as: $\tau_{oct} = \frac{1}{3}\sqrt{(\sigma_1 - \sigma_2)^2 + (\sigma_1 - \sigma_3)^2 + (\sigma_2 - \sigma_3)^2}$, and k_1, k_2, and k_3 are the material properties.

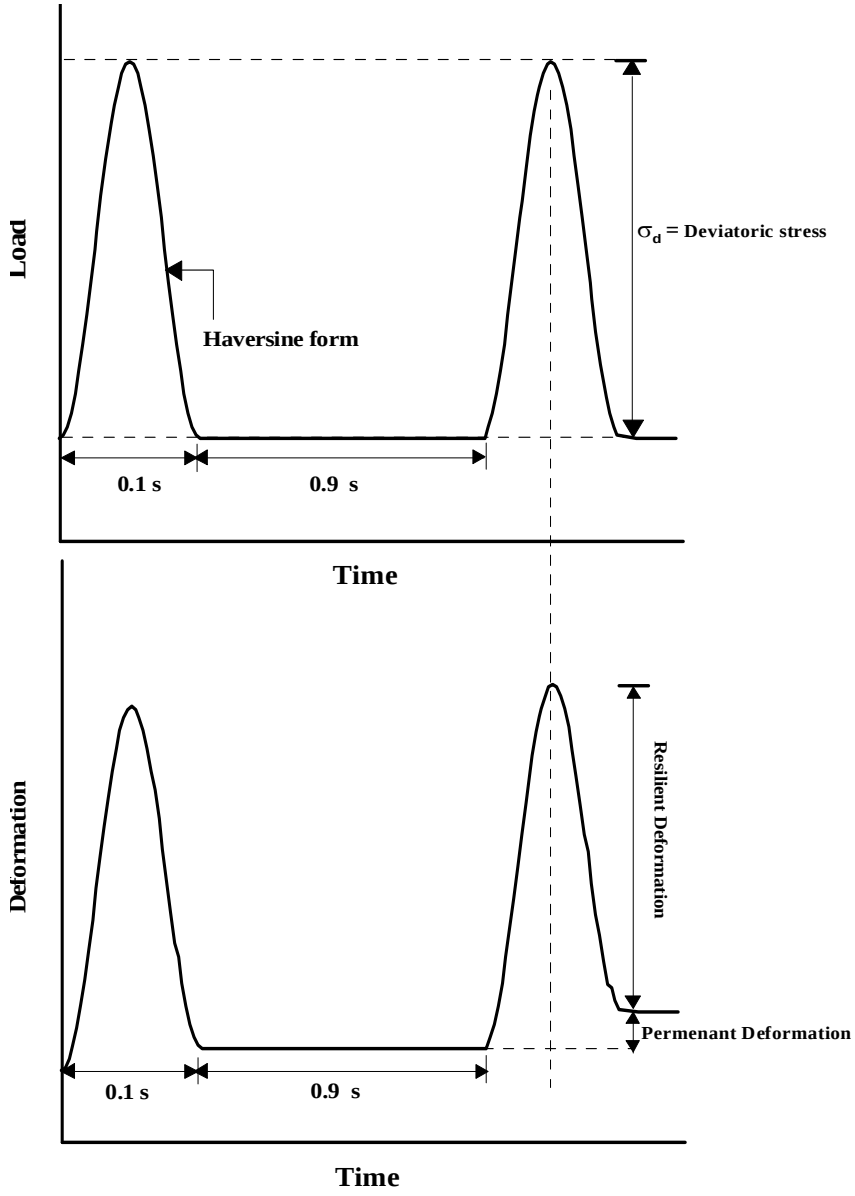

Figure 8
Applied load and response of sample in RLT tests

Repeated Loading Triaxial Tests (RLT) Tests

RLT tests were conducted to determine the properties of granular materials under repeated loading that significantly influence the structural response and performance of base course layers under traffic loading.

Single-stage RLT tests were performed to determine the permanent and resilient deformations of unreinforced and reinforced crushed limestone samples at a different number of load cycles. The tests consisted of conditioning the samples in the same procedure used in the resilient modulus tests. This is followed by applying 10,000 load cycles at a constant confining pressure of 21 kPa and a peak cyclic stress of 230 kPa. The peak cyclic stress was selected based on finite element analysis that was conducted in this second part of this work and will be discussed later. Tests were stopped after 10,000 load cycles or when the sample reached a permanent vertical strain of 7 percent. Each cycle consisted of the same load pulse used in resilient modulus tests.

During single-stage RLT test, at pre-set regular intervals of loading, vertical deformation was recorded at a frequency of 1000 times per second during load cycle intervals of: 0-10, 50-100, 190-200, 290-300, 390-400, 490-500, 590-600, 690-700, 790-800, 890-900, 990-1000, 1490-1500, 1990-2000, 2490-2500, 2990-3000, 3990-4000, 4990-5000, 7990-8000, and 9990-10000. The recorded data were processed in a FORTRAN subroutine code, which was written to calculate the permanent and resilient strains.

Based on the results of the single stage tests, the reduction in the vertical permanent strain (RPS) due to geogrid reinforcement was determined at 100; 1,000; 5,000; and 10,000 load cycles using the following equation:

$$\text{RPS (\%)} = \frac{\text{permanent strain without geogrid -permanent strain with geogrid}}{\text{permanent strain without geogrid}} \times 100\% \qquad (4)$$

Statistical Analysis

Statistical analysis of variance (ANOVA) was conducted to assess the effects of geogrid type and arrangement on the IM-$E_{s1\%}$, IM-$E_{s2\%}$, and IM-USS obtained from the triaxial compression tests. The linear model used in these analyses was a completely randomized factorial design (geogrid arrangements × geogrid types) as shown in the following equation:

$$Y_{ijk} = \mu + \tau_{1i} + \tau_{2j}\ \tau_1\tau_{2ij} + \varepsilon_{ijk} \qquad (5)$$

where, μ is the overall mean; τ_{1i} is the effect of geogrid arrangement; τ_{2j} is the effect of geogrid type; $\tau_1\tau_{2ij}$ is effect of the interaction between the geogrid arrangement and type; ϵ_{ijk} is the random sampling variation for observation k, at any location case and stiffness level ij; and Y_{ijk} is the dependent variable.

ANOVA analyses were also conducted to detect the effect of geogrid stiffness and arrangement on the reduction of RPS values at 100; 1,000; 5,000; and 10,000 load cycles. The linear Completely Random Design (CRD) model used in this analysis is shown in equation (6). The dependent variable used in the analysis was RPS%.

$$RPS\% = \mu + \tau_{1i} + \tau_{2j} + \tau_{3k} + \tau_1\tau_{2ij} + \tau_1\tau_{3ik} + \tau_2\tau_{3jk} + \tau_1\tau_2\tau_{3ijk} + \varepsilon_{ijkl} \quad (6)$$

In equation (6), μ is the overall mean; τ_{1i} is the effect of geogrid arrangement; τ_{2j} is the effect of geogrid type/stiffness; τ_{3k} is the effect of number of load cycles; $\tau_1\tau_{2ij}$ is the effect of the interaction between the geogrid arrangement and type; $\tau_1\tau_{3ik}$ is the effect of the interaction between the geogrid arrangement and number of load cycles; $\tau_2\tau_{3ik}$ is the effect of the interaction between the type/stiffness and number of load cycles; $\tau_1\tau_2\tau_{3ijk}$ is the effect of the interaction between the geogrid arrangement, geogrid stiffness, and the number of load cycles; and ϵ_{ijkl} is the random sampling variation.

Numerical Modeling

Numerical models were developed to simulate vehicular load using ABAQUS finite element software package for flexible pavement sections with unreinforced and geogrid reinforced base course layers *[54]*. These models were used to evaluate the benefits achieved by reinforcing pavement sections in terms of permanent deformations, stresses and strains within the pavement section. The numerical modeling program in this study aimed at investigating the effect of various variables on the design of flexible pavements with reinforced bases. The variables were the:

1. thicknesses of the base course layer
2. stiffness of reinforcement material
3. location of the reinforcement material
4. strength of the subgrade material

The description of the different features of the numerical models used in this study can be found in Appendix A.

Study Matrix

A finite element model was first developed for a pavement structure which consisted of a 50-mm (2-in.) AC layer, crushed limestone I base course layer, and subgrade layer. The developed model was used to investigate the effects of different variables on the degree of improvement achieved by reinforcing the base course layer with a geogrid layer. These variables included the strength of the subgrade material, the thickness of the base course layer as well as the stiffness, location, and interface properties of the geogrid reinforcement material. To study these variables, finite element analyses were first conducted on 15 unreinforced sections with 3 different subgrade strength properties and 5 base course layer thicknesses for use as reference. The three different subgrades included: a weak subgrade with a CBR value less than 1.5, a moderate subgrade with a CBR value of 6, and a stiff subgrade with a CBR of 13. While the five different base course layer thicknesses varied from 150 mm (6 in.) to 254 mm (10 in.) and included 150 mm (6 in.), 175 mm (7 in.), 200 mm (8 in.), 225 mm (9 in.), 254 mm (10 in.) base layer thicknesses. Table 3 presents a summary of the different sections investigated in this study. It should be noted that the different sections will be hereafter identified using the reference names (i.e., section IDs) provided in Table 3. Finite element analyses were then conducted on the different pavement sections reinforced with a geogrid layer placed at the bottom of the base course layer. Four geogrid types with stiffness properties were used in this study.

The finite element model was also used to investigate the effect of the location of the geogrid reinforcement within the base course layer on the reinforced section performance. Four different locations were investigated in this study as shown in Figure 7. Generally, the optimum location of geogrid layer depends on the thickness of the base course layer and the subgrade strength *[3]*. Therefore, to investigate the geogrid location effect, finite element analyses were conducted on section 1a and section 5c, which represent sections that have the combination of the lowest and highest base thickness and subgrade stiffness.

Another finite element model was of a pavement structure consisting of an asphalt layer with 75 mm thickness, crushed limestone II base course layer, and subgrade layer. The finite element model was used to analyze nine pavement sections with three different subgrade strength properties and three base course layer thicknesses. The sections were evaluated before and after placing geogrid reinforced layer at the bottom of the base course layer. Three types of geogrids representing the properties of Tensar BX 1100, Tensar BX 1200, and Tensar BX 1500 were used in this study.

Table 3
Investigated pavement sections

Section ID	Base Course Thickness (mm)	Subgrade Quality
Section 1a	150	Weak
Section 1b	150	Moderate
Section 1c	150	Stiff
Section 2a	175	Weak
Section 2b	175	Moderate
Section 2c	175	Stiff
Section 3a	200	Weak
Section 3b	200	Moderate
Section 3c	200	Stiff
Section 4a	225	Weak
Section 4b	225	Moderate
Section 4c	225	Stiff
Section 5a	250	Weak
Section 5b	250	Moderate
Section 5c	250	Stiff

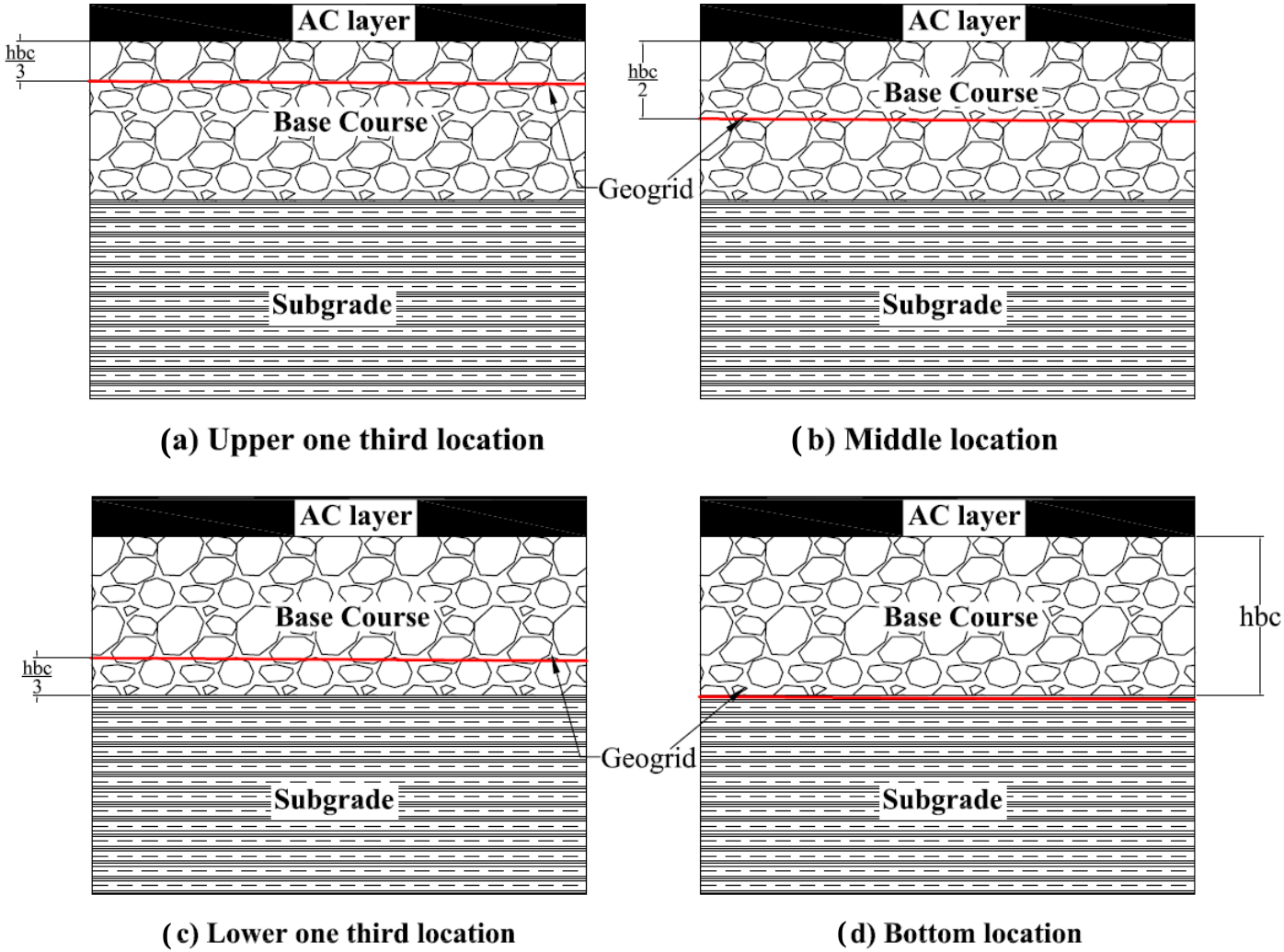

Figure 9

Geogrid Locations Investigated in the Parametric Study

DISCUSSION OF RESULTS

Analysis and Results of Experimental Testing Program

This section presents the results of the experimental testing program that was conducted to characterize the behavior of the geogrid reinforced base course materials under static as well as cyclic loading. Two base course materials were used: Kentucky limestone (crushed limestone I) taken from Martin Marietta quarry and Mexican limestone (crushed limestone II) taken from Vulcan quarry located near Baton Rouge.

Traditional Laboratory Tests

The results of compaction, specific gravity (G_s), CBR, and absorption tests performed on the base materials are summarized in Table 4, and the standard compaction curves for crushed limestone I and II are shown in Figure 10.

Sieve analyses tests were also performed before and after compaction of the two base course materials. Figure 10 compares the grain size distribution before and after compaction for crushed limestone I and II, respectively. It is noted that the crushed limestone I gradation was slightly changed by compaction. On the contrary, the compaction of crushed limestone II had a significant effect on its grain size distribution, such that the whole gradation curve was shifted to the right, indicating an increase in the fine content and demonstrating that a significant amount of crushing and abrasion of the crushed limestone II aggregates occurred during compaction.

Table 4
Properties of crushed limestone materials

Material	Bulk Specific of gravity	Apparent Specific of gravity	CBR	*OMC(%) and ** γ_{max} (psf)	Absorption %
Crushed limestone I (Kentucky limestone)	2.54	2.7	101	7.0, 139	2.14
Crushed limestone II (Mexican limestone)	2.24	2.56	72	9.2, 127.6	5.65

*OMC: optimum moisture content obtained in Standard Proctor Test

** γ_{max} : maximum unit weight obtained in Standard Proctor Test

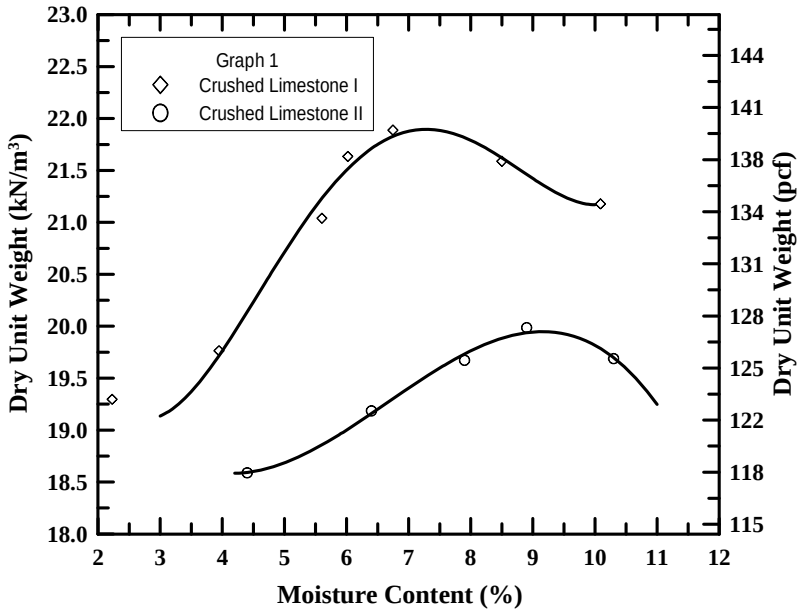

Figure 10
Compaction curve of crushed limestone I and II

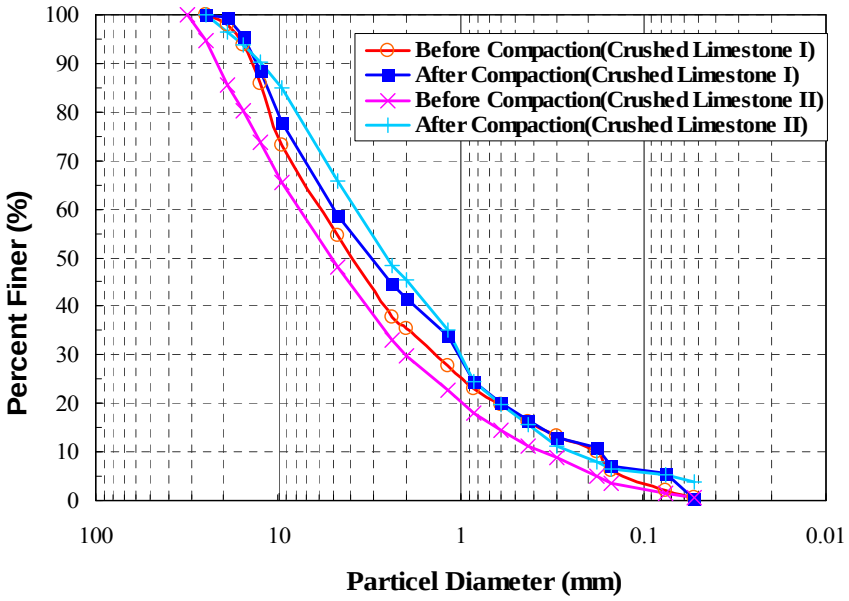

Figure 11
Particle size distribution of crushed limestone I and II

Triaxial Compression Test

Drained triaxial compression tests were conducted on unreinforced and samples reinforced with geogrid Types I through V for crushed limestone I and on unreinforced samples and samples reinforced with geogrid Types II, IV, and V for crushed limestone II.

For each geogrid type, the middle, upper one-third, and double arrangements were investigated.

Figure 12 depicts the average stress-strain curves obtained from the drained triaxial compression tests conducted on unreinforced crushed limestone I samples and samples reinforced with geogrid types I. However, the stress-strain curves obtained from the triaxial compression tests conducted on unreinforced crushed limestone II and reinforced crushed using geogrid II are presented in Figure 13. The test results for other geogrid reinforcements for the two materials are presented in Appendix B.

The figures show that at the confining pressures of 3 psi and maximum dry unit weight the crushed limestone I samples behave as a loose granular material, such that they exhibit an increase in shear strength with increasing strain, which is referred to as strain hardening, and eventually they stabilize at strain level of about 4 percent. A dense granular material behavior was observed for crushed limestone II samples. They exhibit an increase in the shear stress with strain increase until reaching an ultimate (peak) shear stress. Beyond the peak stress, they demonstrate strain softening behavior where the shear stress decrease with the strain increase until eventually stabilizing and reaching a constant value, which is referred to as the residual shearing strength (RSS). In contrast to crushed limestone I samples, the RSS of the crushed limestone II samples was much smaller than the ultimate shear strength. This reduction can be attributed to the development of large shear strains localized in a narrow zone called shear band.

Figure 14 presents a photo of tested unreinforced crushed limestone II sample. A close examination of the photo reveals that a thick shear band was formed in the unreinofrced sample. The plane of failure in these samples is observed to be close to that predicted in classical soil mechanics theories, which is $45 + \phi/2$.

It is clear that the inclusion of geogrid reinforcement layer(s) substantially improved the strength and stiffness of the crushed limestone materials. This improvement was more pronounced at strain levels greater than 1 percent. More significant improvement was observed for samples reinforced with two geogrid layers. The inclusion of a geogrid layer(s) within crushed limestone II samples increased the peak strength and reduced the post-peak loss of strength. However, the RSS still remains significantly less than the USS.

Figure 15 and 16 depict pictures of crushed limestone II samples reinforced with a geogrid layer placed at the middle and upper one-third locations taken at the end of the triaxial compression tests. The figures show that although the shear bands were

developed within the tested samples the orientation, location, and plane of these bands changed with the location of the geogrid layer in the sample.

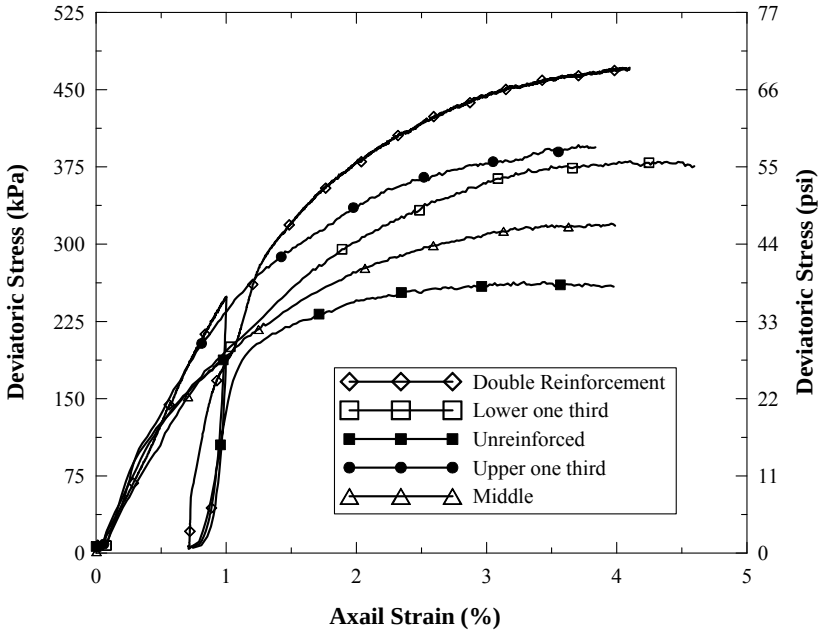

Figure 12
Stress-strain curves for crushed limestone I samples reinforced with geogrid Type I

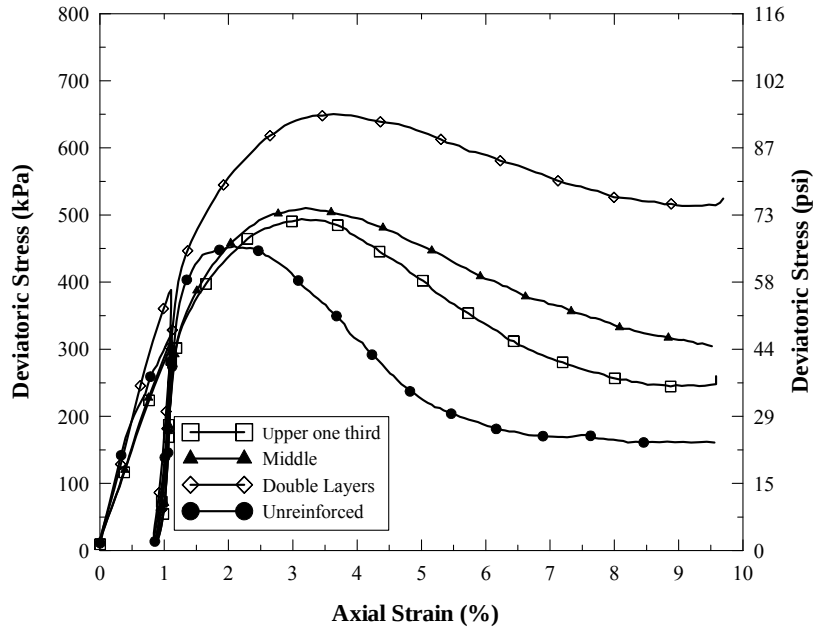

Figure 13
Stress-strain curve for crushed limestone II samples reinforced with geogrid Type II

Figure 17 depicts post testing photos of crushed limestone II samples reinforced with two geogrid layers. It is noted that the geogrid caused the development of clogging in the shear band within the samples, such that they failed by bulging between the two adjacent layers of geogrids. This suggests that the use of the reinforcement layers changed the pattern of deformation in the collapse mechanism of reinforced samples.

Figure 14
Unreinforced crushed limestone II sample after the end of triaxial compression test

Figure 15
Picture for samples reinforced at mid height

Figure 16
Picture for samples reinforced at upper one-third

Figure 17
Picture for samples reinforced with two geogrid layers

Four response parameters were obtained from each triaxial test, namely, $E_{s1\%}$, $E_{s2\%}$, the USS, and RSS.

Figure 18 through Figure 19 present the average improvement factors and the standard deviation values obtained for each reinforced case of crushed limestone I. The improvement factor for residual strength was not calculated for this material since the residual and ultimate shear strengths had similar values.

Figure 21 through Figure 24 present the average improvement factors and the standard deviation values obtained for each reinforced case of crushed limestone II. The figures show that the improvement in all three parameters (IM-$E_{s1\%}$, IM-$E_{s1\%}$, and IM-USS) depends on the type, location, and number of geogrid layers. It is also noted that the improvement increases with increasing the geogrid stiffness. In addition, the double arrangement had the maximum improvement. For crushed limestone I, The improvement was more appreciable in the E_{s2}% and USS than those in $E_{s1\%}$, and the maximum improvement was detected in the USS. The IM-$E_{s1\%}$ ranged from 0.95 to 1.82; the IM-E_{s2}% ranged from 0.99 to 2.32, and the IM-USS ranged from 1.163 to 2.42. For crushed limestone II, the reinforced samples had a slight improvement in $E_{s1\%}$, and $E_{s2\%}$, such that IM-$E_{s1\%}$, and IM-$E_{s2\%}$ ranged between 0.95 and 1.15 with a maximum improvement of 15 percent. The improvement due to geogrid reinforcement was more appreciable in the USS than $E_{s1\%}$ and $E_{s2\%}$ especially for double arrangement cases, and it ranged between 1.1 and 1.55. However, the effect of the reinforcement on the magnitude of IM-RSS was much greater than the other factors. For example, samples reinforced with two layer of geogrid Type V had four times higher RSS values than unreinforced samples. The IM-RSS ranged between 1.65 and 4, which suggests that the greatest contribution of the geogrid was in the residual strength.

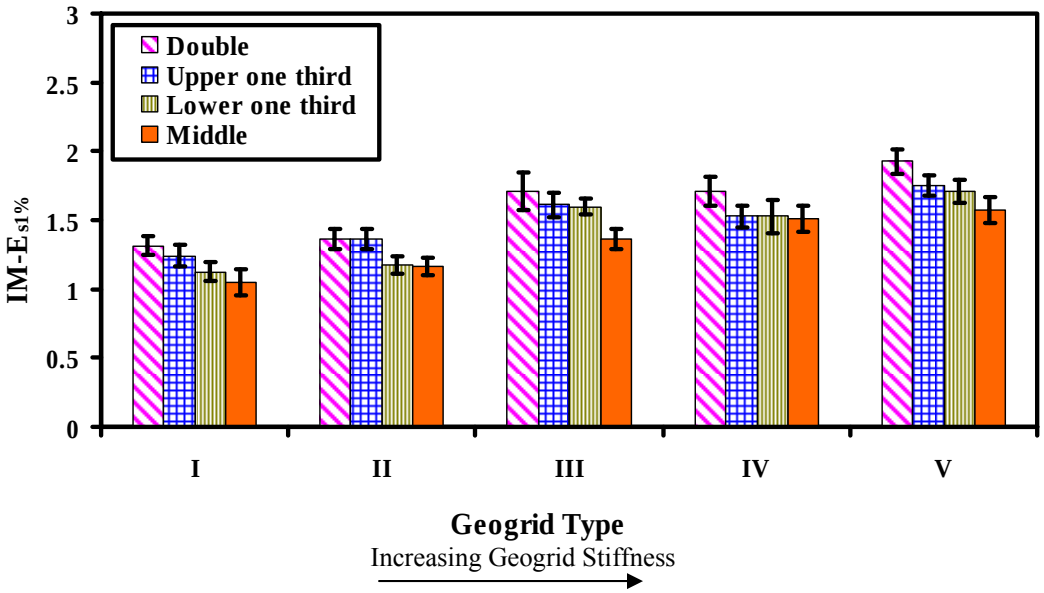

Figure 18
Improvement factor IM-$E_{s1\%}$ for reinforced crushed limestone I samples

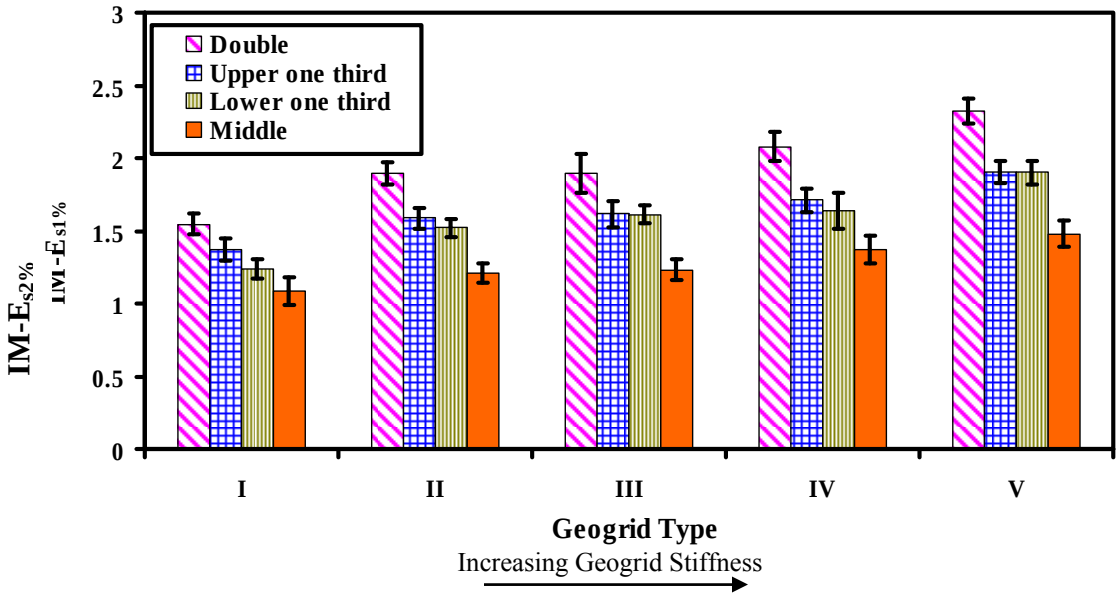

Figure 19
Improvement factor IM-$E_{s2\%}$ for reinforced crushed limestone I samples

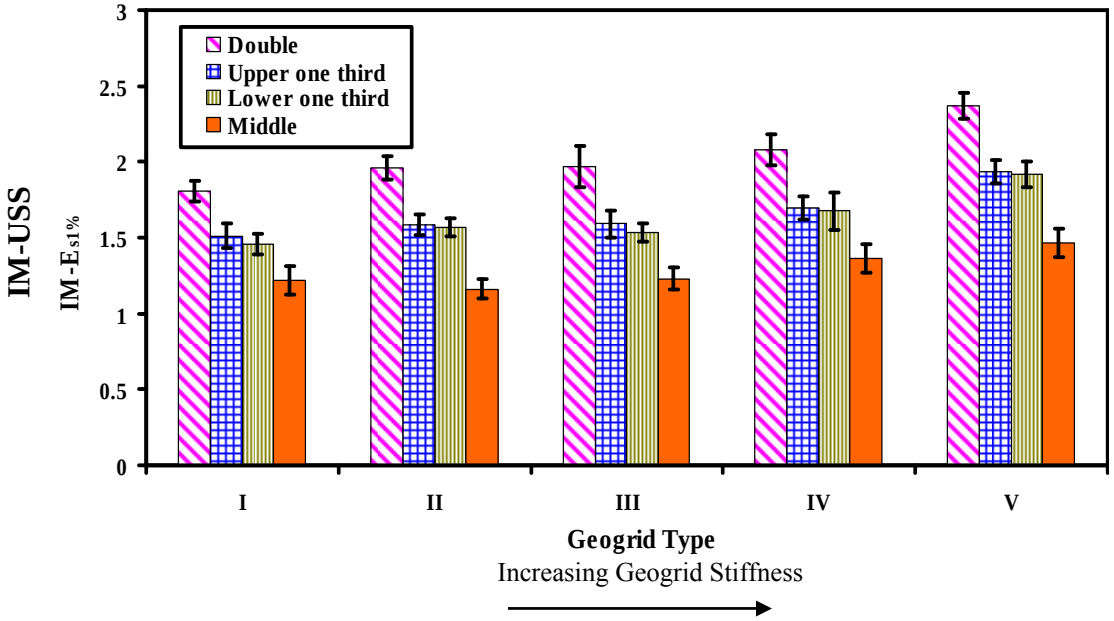

Figure 20
Improvement factor IM-USS for reinforced crushed limestone I samples

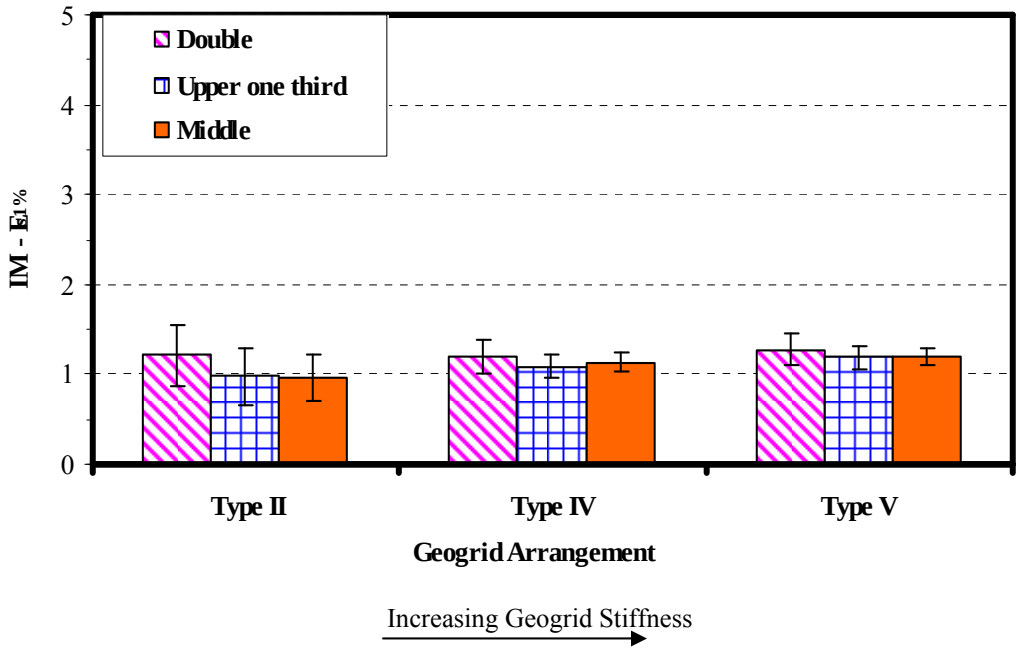

Figure 21
Improvement factor IM- $E_{s1\%}$ for reinforced crushed limestone II samples

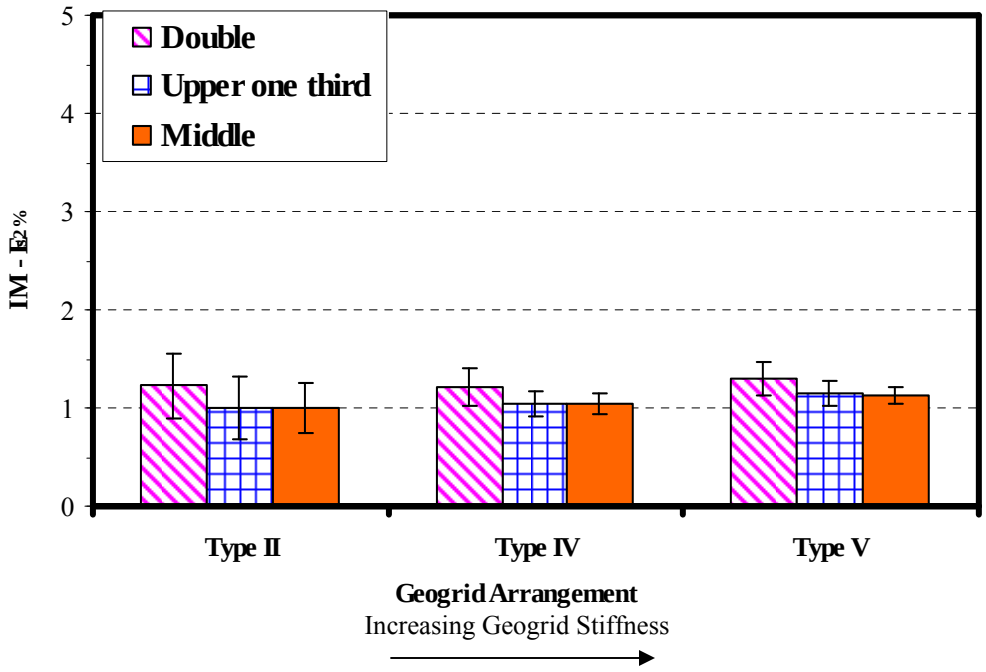

Figure 22
Improvement factor IM-$E_{s2\%}$ for reinforced crushed limestone II samples

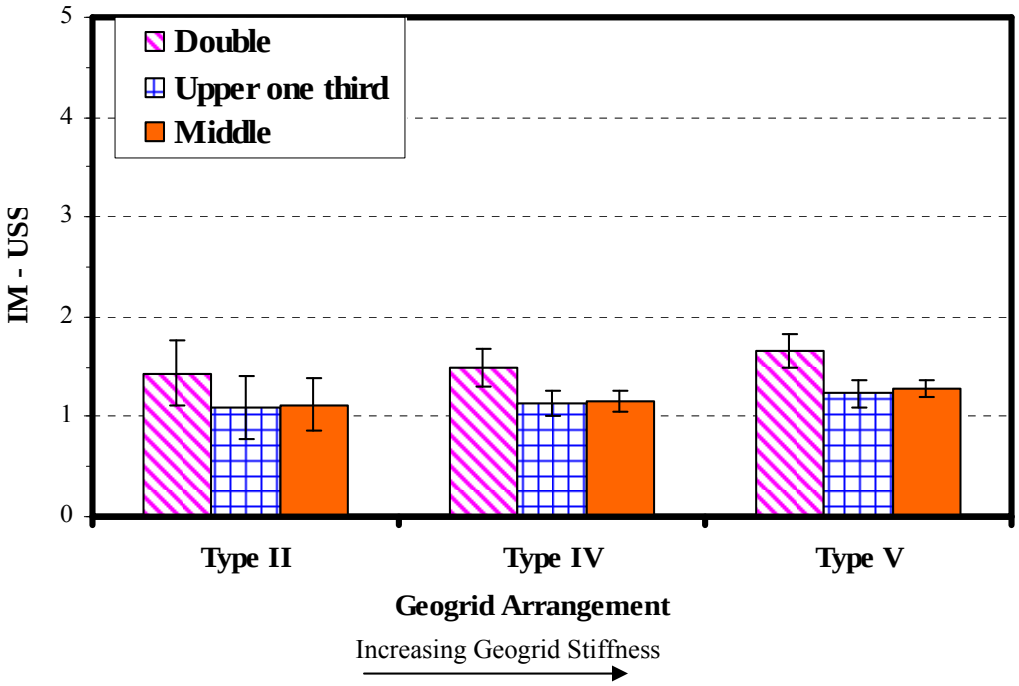

Figure 23
Improvement factor IM-USS for reinforced crushed limestone II samples

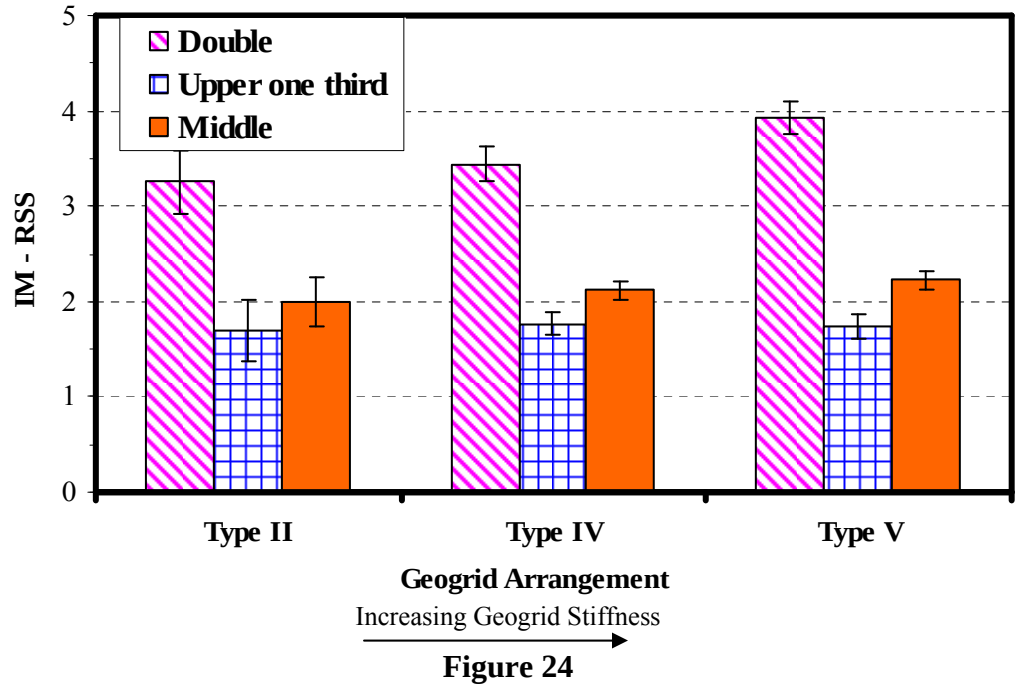

Figure 24
Improvement factor IM-RSS for reinforced crushed limestone II samples

An ANOVA analysis was performed on the triaxial test results for crushed limestone I and II. The results of ANOVA for crushed limestone I are presented in Table 5. It showed that at a 95 percent confidence level, the geogrid type and arrangement had a significant effect on the IM-$E_{s1\%}$, IM-$E_{s2\%}$, and IM-USS. The geogrid type had more a significant effect on IM-$E_{s1\%}$ than the geogrid arrangement, while the geogrid arrangement affected more significantly the IM-$E_{s2\%}$ and IM-USS, as indicated by the F-value. The interaction effect of the geogrid type-geogrid arrangement ($\tau_1\tau_{2ij}$) had significant effect only on the IM-$E_{s2\%}$ and IM-USS. The significance of interaction indicates that the behaviors of the two main effects (geogrid type and arrangement) are inconsistent, which means that they do not increase and decrease by the same rate. The results of ANOVA for crushed limestone II are presented in Table 6. It is noted that, at a 95 percent confidence level, the geogrid type did not have a significant effect on the IM-$E_{s1\%}$, and IM-$E_{s2\%}$, while it significantly affected the IM-USS and IM-RSS. This suggests that high deformation is needed to effectively mobilize the tensile membrane resistance, which the mechanism is dominated by the geogrid stiffness. The geogrid arrangement had a significant effect on all improvement factors. Furthermore, it had a more appreciable influence than geogrid type, especially for IM-USS and IM-RSS, as indicated by the F-value. Finally, the interaction effect of the geogrid type-geogrid arrangement ($\tau_1\tau_{2ij}$) had significant effects only on the IM-RSS.

Based on the result of the ANOVA analyses, post ANOVA Least Square Means (LSM) analyses were conducted to compare the effect of all the different geogrid types and arrangements on the IM-$E_{s1\%}$, IM-$E_{s2\%}$, IM-USS, and IM-RSS. The results of post ANOVA-LSM analyses are presented in Tables 7 and 8 for crushed limestone I and Tables 9 and 10 for crushed limestone II. In these tables, the groups are listed in descending order from the best improvement to the worst, and groups with same letter next to them are not significantly different.

Table 7 presents the grouping of the geogrid type effect on IM$E_{s1\%}$, IM-$E_{s2\%}$, and IM-USS for crushed limestone I. The maximum and minimum improvements were achieved when using geogrids Types V and I, respectively. These two geogrid types have the highest and the lowest stiffness, respectively. The effects of geogrid Types III and IV on IM-$E_{s1\%}$ were not statistically different from each other. However, the effect of geogrid Type III on IM$E_{s2\%}$ and IM-USS was significantly different from geogrid Type IV but not from geogrid Type II. The grouping of the effect of geogrid arrangement on the IM$E_{s1\%}$, IM-$E_{s2\%}$, and IM-USS for crushed limestone I is presented in Table 8. The highest benefit was achieved when the double arrangement was used while the lowest benefit was

observed for the middle arrangement. In addition, the upper and lower one-third arrangement effects on IM-USS were not statistically significantly from each other.

Table 5
ANOVA results for crushed limestone I

Type III Tests of Fixed Effects for IM-$E_{s1\%}$				
Effect	Num DF	Den DF	F Value	Pr > F
Geogrid Type	4	40	139.34	< .0001
Geogrid arrangement	3	40	43.19	< .0001
Interaction	12	40	1.91	0.0625
Type III Tests of Fixed Effects for IM-$E_{s2\%}$				
Effect	Num DF	Den DF	F Value	Pr > F
Geogrid Type	4	40	209.38	< .0001
Geogrid arrangement	3	40	394.00	< .0001
Interaction	12	40	3.07	0.0038
Type III Tests of Fixed Effects for IM-USS				
Effect	Num DF	Den DF	F Value	Pr > F
Geogrid Type	4	40	133.99	< .0001
Geogrid arrangement	3	40	563.00	< .0001
Interaction	12	40	3.04	0.0040

Table 6
ANOVA results for crushed limestone II

Type III Tests of Fixed Effects for IM-$E_{s1\%}$				
Effect	Num DF	Den DF	F Value	Pr > F
Geogrid Type	2	18	2.98	0.0761
Geogrid arrangement	2	18	19.09	<.0001
Interaction	4	18	0.38	0.8167
Type III Tests of Fixed Effects for IM-$E_{s2\%}$				
Effect	Num DF	Den DF	F Value	Pr > F
Geogrid Type	2	18	3.03	0.0684
Geogrid arrangement	2	18	12.22	0.0004
Interaction	4	18	0.71	0.5954
Type III Tests of Fixed Effects for IM-USS				
Effect	Num DF	Den DF	F Value	Pr > F
Geogrid Type	2	18	11.67	0.0006
Geogrid arrangement	2	18	49.45	<.0001
Interaction	4	18	0.27	0.8911
Type 3 Tests of Fixed Effects for IM-RSS				
Effect	Num DF	Den DF	F Value	Pr > F
Geogrid Type	2	18	13.63	0.0002
Geogrid arrangement	2	18	200.83	<.0001
Interaction	4	18	3.13	0.0407

Table 9 shows the grouping of the geogrid types' effect on IM-USS and IM-RSS for crushed limestone II. It can be seen that Type V geogrid, the geogrid with greatest stiffness, exhibited the highest IM-USS and IM-RSS values, while the other two geogrid types had almost similar values. The grouping of the effect of geogrid arrangement on the IM-$E_{s1\%}$, IM-$E_{s2\%}$, IM-USS, and IM-RSS for crushed limestone II is presented in Table 10. The highest benefit was achieved when the two layers of geogrids were used to reinforce the samples. The middle and upper one-third locations had similar IM-$E_{s1\%}$, IM-$E_{s2\%}$, and IM-USS values. However, it seems that the middle location was more effective than the upper one-third location in reducing the post peak strain softening, so it had higher IM-RSS value.

The results of the monotonic triaxial tests clearly showed that the geogrid improvement for the crushed limestone II was mobilized at a higher strain level compared to crushed limestone I. The greatest benefit obtained from reinforcing the crushed limestone II material was in altering the development of shear bands and minimizing the reduction in

residual strength. This difference in the behavior may be explained by the dense state that the crushed limestone II material compared to the loose state of the crushed limestone I. The difference between the optimum moisture contents (7 and 9.2 percent) for each material provides another reason for the dissimilarities between the geogrid improvements.

Table 7
Grouping of geogrid type effect on IM-$E_{s1\%}$, IM-$E_{s1\%}$, and IM-USS for crushed limestone I

Dependent	Geogrid Type	Estimate	Standard Error	Letter
IM-$E_{s1\%}$	Type V	1.7413	0.01978	A
	Type III	1.5705	0.01978	B
	Type IV	1.5681	0.01978	B
	Type II	1.2658	0.01978	C
	Type I	1.1817	0.01978	D
IM-$E_{s2\%}$	Type V	1.9013	0.01532	A
	Type IV	1.6640	0.01532	B
	Type III	1.5888	0.01532	C
	Type II	1.5526	0.01532	C
	Type I	1.2847	0.01532	D
IM-USS	Type V	1.9215	0.01438	A
	Type IV	1.7038	0.01438	B
	Type III	1.5810	0.01438	C
	Type II	1.5682	0.01438	C
	Type I	1.4986	0.01438	D

Table 8
Grouping of geogrid arrangement effect on IM-$E_{s1\%}$, IM-$E_{s1\%}$, and IM-USS for crushed limestone I

Dependent Variable	Geogrid Arrangement	Estimate	Standard Error	Letter Group
IM-$E_{s1\%}$	Double Layers	1.6049	0.01769	A
	Upper one-third	1.4993	0.01769	B
	Lower one-third	1.4286	0.01769	C
	Middle	1.3291	0.01769	D
IM-$E_{s2\%}$	Double Layers	1.9187	0.01371	A
	Upper one-third	1.6378	0.01371	B
	Lower one-third	1.5813	0.01371	C
	Middle	1.2554	0.01371	D
IM-USS	Double Layers	2.0358	0.01286	A
	Upper one-third	1.6633	0.01286	B
	Lower one-third	1.6302	0.01286	B
	Middle	1.2892	0.01286	C

Table 9
Grouping of geogrid type effect for crushed limestone I

Dependent Variable	Geogrid Type	Estimate	Standard Error	Letter Group
IM-USS	Type V	1.4125	0.03047	A
	Type IV	1.2487	0.03047	B
	Type II	1.2194	0.03047	B
IM-RSS	Type V	2.7277	0.07398	A
	Type IV	2.3406	0.07398	B
	Type II	2.2004	0.07398	B

Table 10
Grouping of geogrid arrangement effect for crushed limestone I

Dependent Variable	Geogrid Arrangement	Estimate	Standard Error	Letter Group
IM-$E_{s1\%}$	Double Layers	1.1904	0.02208	A
	Upper one-third	1.0254	0.02208	B
	Middle	1.0214	0.02208	B
IM-$E_{s2\%}$	Double Layers	1.2265	0.02960	A
	Upper one-third	1.0556	0.02960	B
	Middle	1.0400	0.02960	B
IM-USS	Double Layers	1.5405	0.03047	A
	Upper one-third	1.1829	0.03047	B
	Middle	1.1571	0.03047	B
IM-RSS	Double Layers	3.6068	0.07398	A
	Middle	2.0502	0.07398	B
	Upper one-third	1.6118	0.07398	C

Resilient Modulus RLT Test Results

Resilient modulus tests were performed on unreinforced crushed lime stone I samples and samples reinforced with geogrid Types I through V. Based on the results of these tests, a regression analysis was carried out to determine the parameters of resilient modulus generalized constitutive model adopted by the Mechanistic Empirical Pavement Design Guide equation (3) *[1]*. The results of this analysis are presented in Tables 11 through 13.

The parameters presented in the tables were used to compute the resilient modulus at the stress state applied in the single-stage RLT tests [confining pressure of 3 psi (21 kPa) and deviatoric stress of 33 psi (230 kPa)] for the different unreinforced and reinforced samples. An improvement factor (IM-M_r) was then determined using equation (1). Figure 25 presents the average improvement factor and the standard deviation values obtained for all reinforced cases. It is noticed that only samples reinforced with two geogrid layers had a slight improvement in the resilient modulus values calculated at the selected stress state. However, no conclusion can be drawn since this improvement lies within the margin of error of the calculated values.

ANOVA and Post ANOVA-LSM analyses with a single factor CRD design and 17 levels (16 reinforced cases and 1 unreinforced case) was conducted to compare the resilient modulus of the reinforced samples to those of the unreinforced sample. Duntte's adjustment was used in this analysis since it is usually used to compare a control effect to

all other effects *[55]*. The showed that at 95 percent confidence level, only the resilient modulus values of samples reinforced with double layers of geogrid Type V were higher than those of unreinforced samples. This suggests that the reinforcement did not have much effect on the resilient modulus properties of crushed limestone.

Table 11
Resilient modulus model coefficients for unreinforced and reinforced samples

Material parameter	Variable	Unreinforced	Geogrid Type I		
			Middle	Upper One-Third	Double
k_1	Average	1788.9	1781.1	1834.6	1813.6
	Stdv	85.7	78.2	99.0	93.6
	COV	4.8	4.4	5.4	5.2
k_2	Average	0.382	0.381	0.385	0.412
	Stdv	0.017	0.017	0.021	0.020
	COV	4.3	4.5	5.3	4.8
k_3	Average	-0.149	-0.385	-0.377	-0.290
	Stdv	0.007	0.016	0.022	0.013
	COV	4.7	4.0	5.7	4.5

Table 12
Resilient modulus model coefficients for samples with geogrid Type II and III

Material parameter	Variable	Geogrid Type II			Geogrid Type III		
		Middle	Upper One-Third	Double	Middle	Upper One-Third	Double
k_1	Average	1790.6	1815.9	1851.9	1793.2	1811.4	1855.3
	Stdv	71.5	82.4	91.7	65.2	116.2	62.7
	COV	4.0	4.5	4.9	3.6	6.4	3.4
k_2	Average	0.408	0.401	0.393	0.384	0.392	0.424
	Stdv	0.016	0.020	0.021	0.019	0.024	0.014
	COV	4.0	4.9	5.2	5.0	6.2	3.3
k_3	Average	-0.199	-0.226	-0.192	-0.295	-0.281	-0.224
	Stdv	0.009	0.010	0.010	0.014	0.019	0.008
	COV	4.3	4.4	5.2	4.7	6.7	3.5

Table 13
Resilient modulus model coefficients for samples with geogrid Type IV and V

Material parameter	Variable	Geogrid Type IV			Geogrid Type V		
		Middle	Upper One-Third	Double	Middle	Upper One-Third	Double
k_1	Average	1796.9	1862.9	1909.1	1815.7	1860.7	1993.8
	Stdv	116.1	103.4	99.3	58.9	70.2	104.7
	COV	6.5	5.6	5.2	3.2	3.8	5.3
k_2	Average	0.399	0.398	0.441	0.415	0.431	0.446
	Stdv	0.027	0.021	0.023	0.016	0.015	0.022
	COV	6.7	5.2	5.3	3.9	3.5	4.8
k_3	Average	-0.257	-0.248	-0.207	-0.232	-0.246	-0.339
	Stdv	0.017	0.014	0.012	0.008	0.010	0.015
	COV	6.5	5.5	5.7	3.4	4.0	4.5

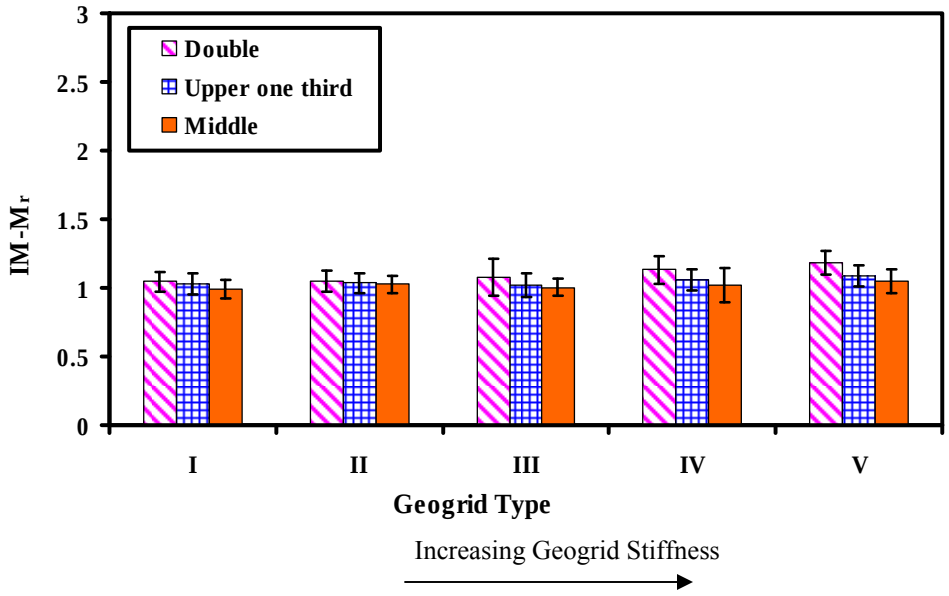

Figure 25
IM-M_r values at stress state applied in single stage RLT tests

Single-Stage RLT Tests

Single-stage RLT tests were performed on unreinforced crushed limestone I and II samples and samples reinforced with geogrid Types II, IV, and V. Three reinforcement

arrangements were investigated for each geogrid type, namely, middle, upper one-third, and double arrangements.

Figures 26 and 27 present the curves of the average permanent strain value versus the number of load cycles for unreinforced samples and samples reinforced with geogrid Type II for crushed limestone I and II, respectively. The test results for samples reinforced with geogrids IV and V are presented in Appendix B. The permanent deformation curve can be divided into two stages. During the first stage, which is referred as the primary post-compaction stage, the material exhibits a high rate of permanent strain. This can be explained by the material densification process that occurs during this stage that results in a great volume change and closure of voids between the particles and the development of high permanent deformation. While the second stage of the permanent deformation, which is referred as the secondary stage, involved a progressive reduction of the rate of permanent deformation accumulation until the permanent strain curve almost reached an asymptote, a steady state behavior was achieved.

The figures demonstrate that there was no distinction between the behavior of unreinforced and reinforced samples during the primary post-compaction stage. However, the geogrids were able to reduce the rate of permanent deformation accumulation in the secondary stage, hence the reinforced samples developed less permanent strain. This improvement was also affected by the geogrid type and arrangement. The figures also showed that, although the crushed limestone II demonstrated higher peak strength values (e.g., Figure 13 on page 31) in monotonic triaxial tests, it developed a much higher permanent strain than the crushed limestone I samples at the same cyclic stress. This indicates that the base course peak strength cannot be used alone to predict the permanent deformation response of base course materials under cyclic loading.

Figure 28 through Figure 31 present the mean and error bars of the RPS values for crushed limestone I obtained at 100, 1000, 5000, and 10,000 load cycles, respectively, while Figure 32 through Figure 35 present the mean and standard deviation values of the RPS for crushed limestone II obtained at 100, 1000, 5000, and 10,000 load cycles, respectively. As seen in the figures, the inclusion of geogrid reinforcement resulted in a reduction in the permanent strain of up to 65 percent. Furthermore, at a certain number of load cycles, the geogrid improvement in permanent deformation test depended on the geogrid type, location, and the number of reinforcement layers, such that stiffer geogrids exhibited higher reductions in permanent strains than the ones with the least stiffness, as can be seen for Type V geogrid compared to Type II geogrid. The figures also show that the upper one-third location had a better improvement than the middle location. In

addition, increasing the number of geogrid layers resulted in a great reduction in the permanent strain. The reduction in permanent strain due to the geogrid reinforcement also varied with the number of load cycles. The reduction was very small at 100 load cycles, especially for samples reinforced with a single geogrid layer. However, the RPS value increased with increasing the number of load cycles.

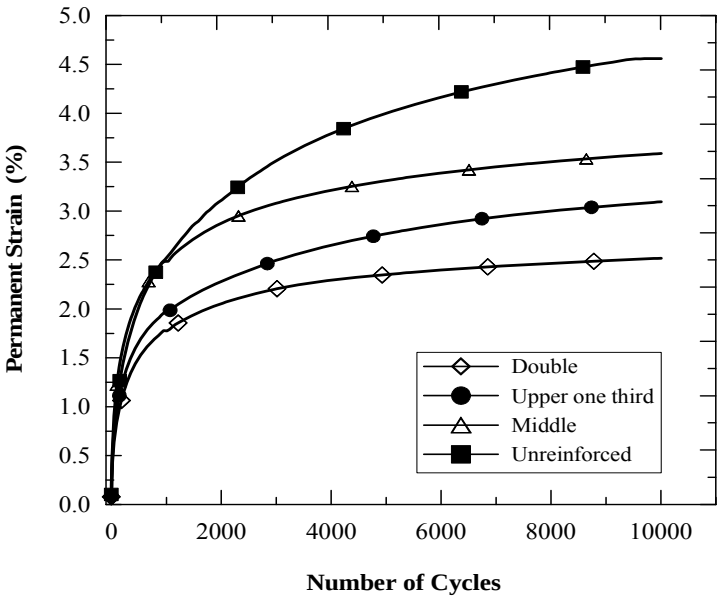

Figure 26
Permanent deformation curves for crushed limestone I samples reinforced with geogrid Type II

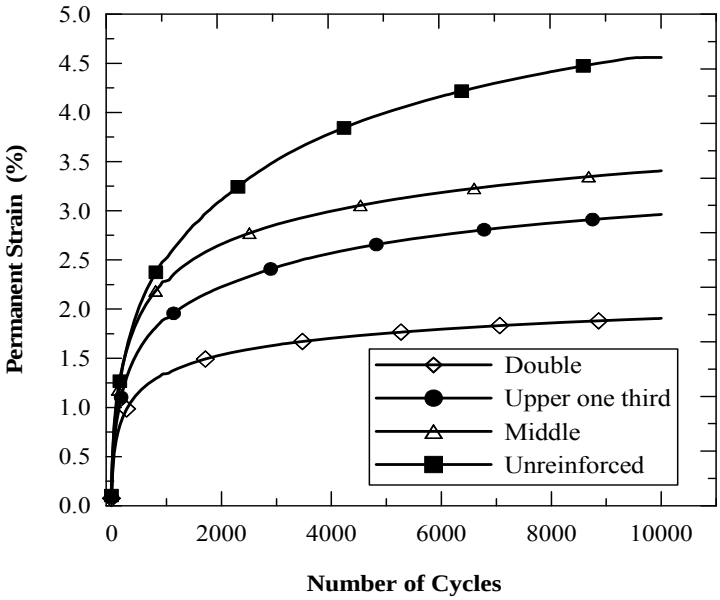

Figure 27
Permanent deformation curves for crushed limestone II samples reinforced with geogrid Type II

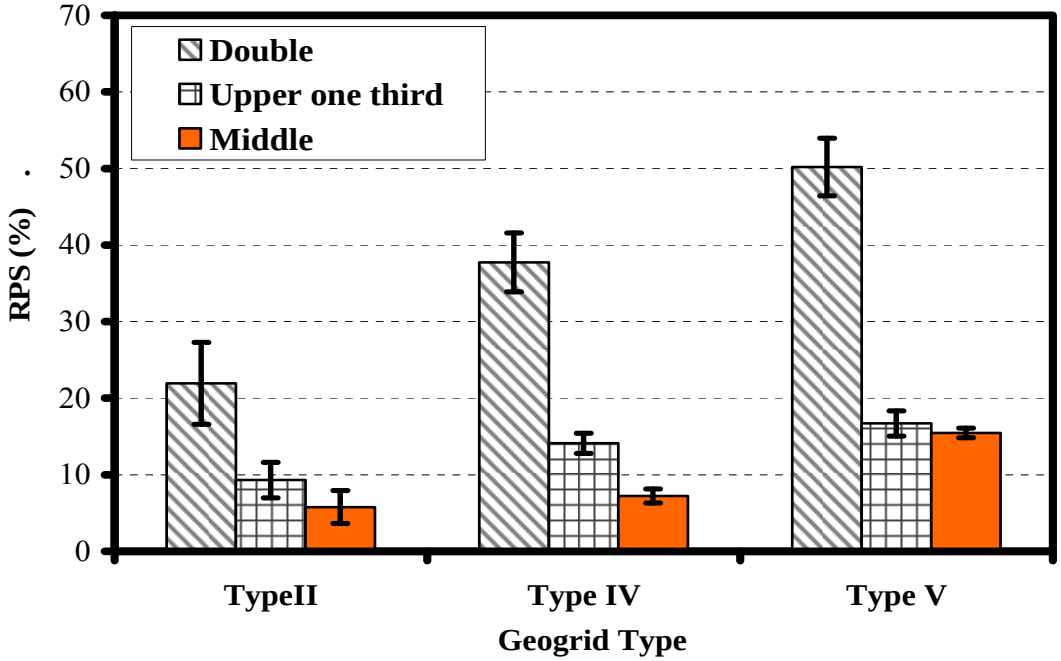

Figure 28
RPS at 100 load cycles for crushed limestone I

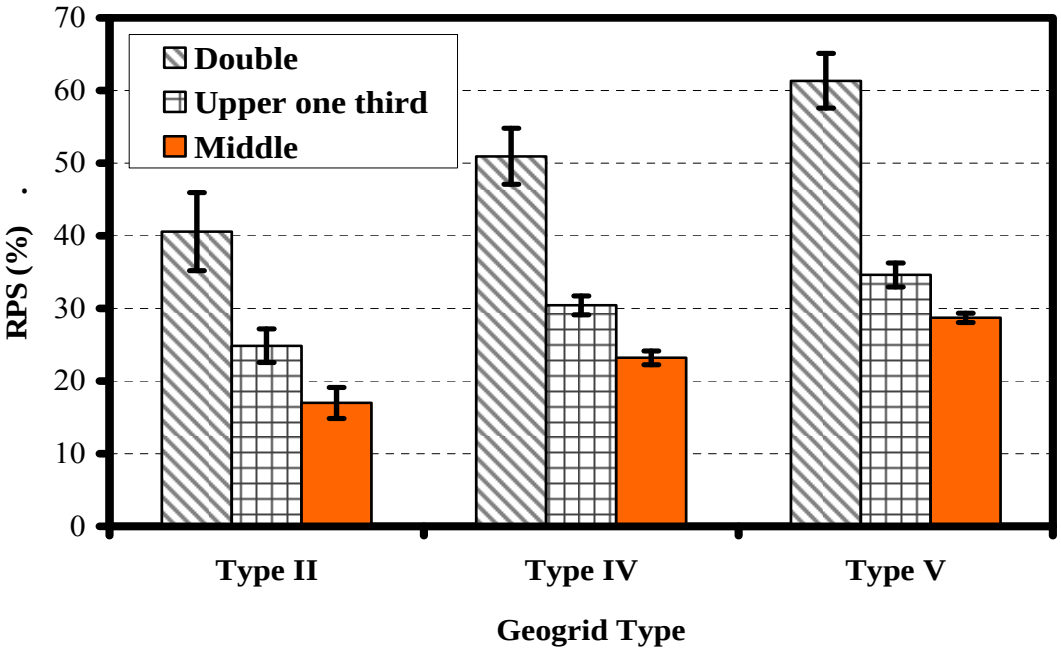

Figure 29
RPS at 1000 load cycles for crushed limestone I

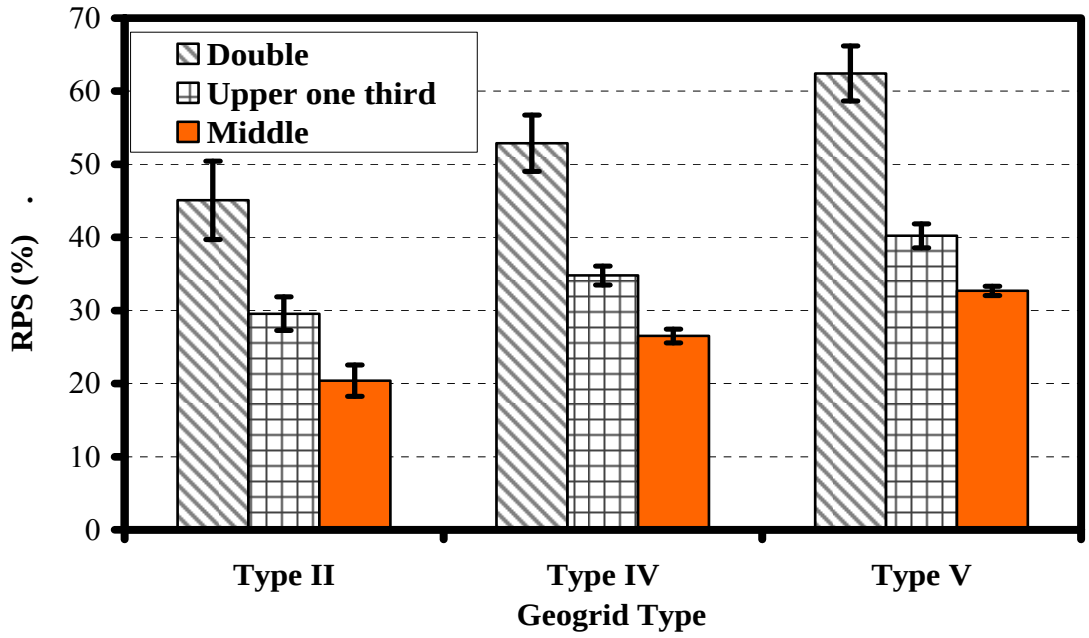

Figure 30
RPS at 5000 load cycles for crushed limestone I

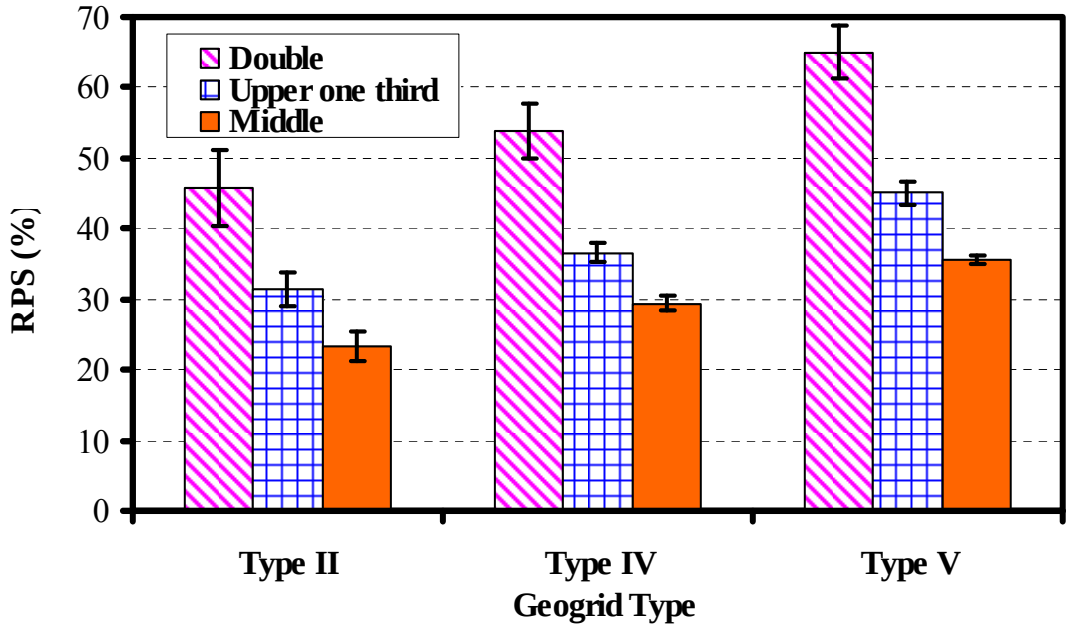

Figure 31
RPS at 10,000 load cycles for crushed limestone I

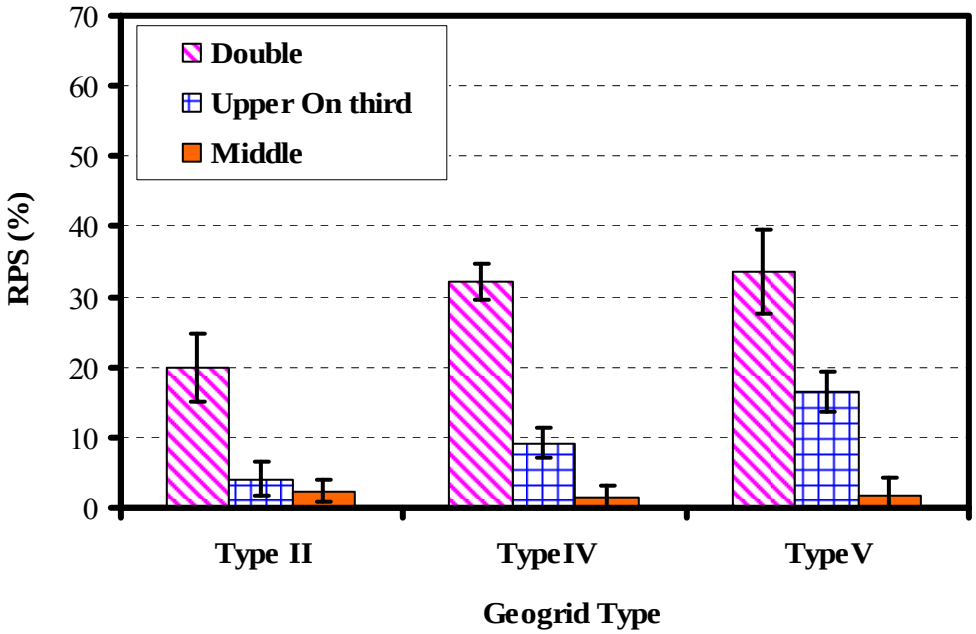

Figure 32
RPS at 100 of load cycles for crushed limestone II

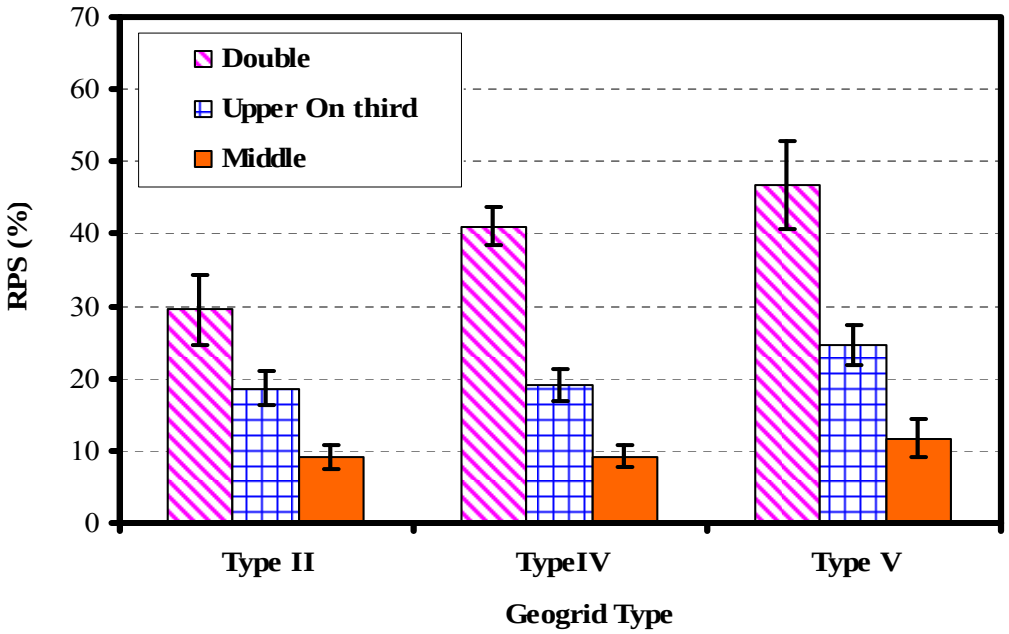

Figure 33
RPS at 1000 of load cycles for crushed limestone II

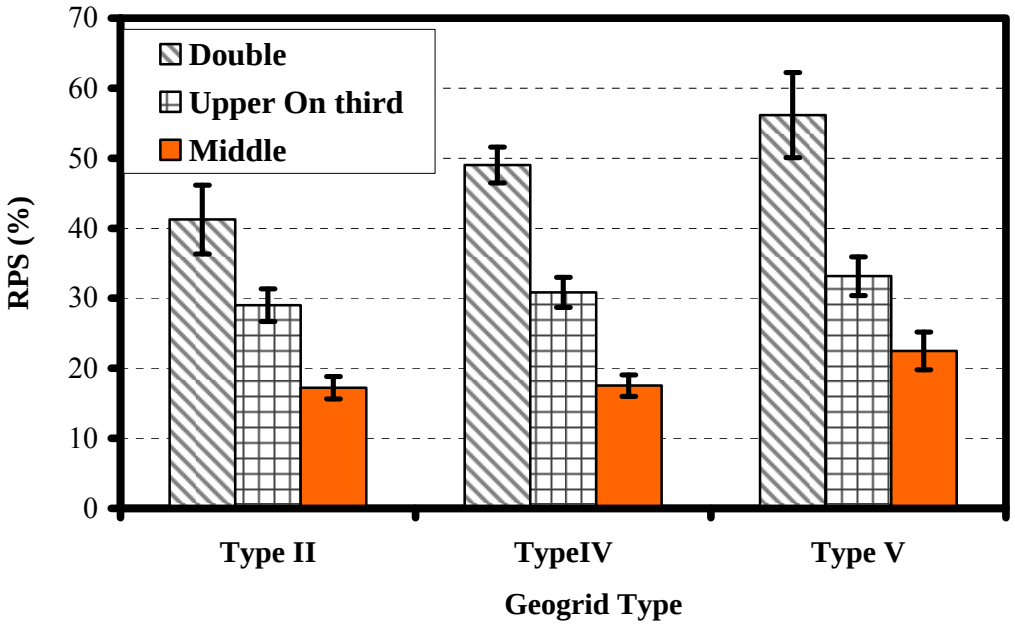

Figure 34
RPS at 5000 of load cycles for crushed limestone II

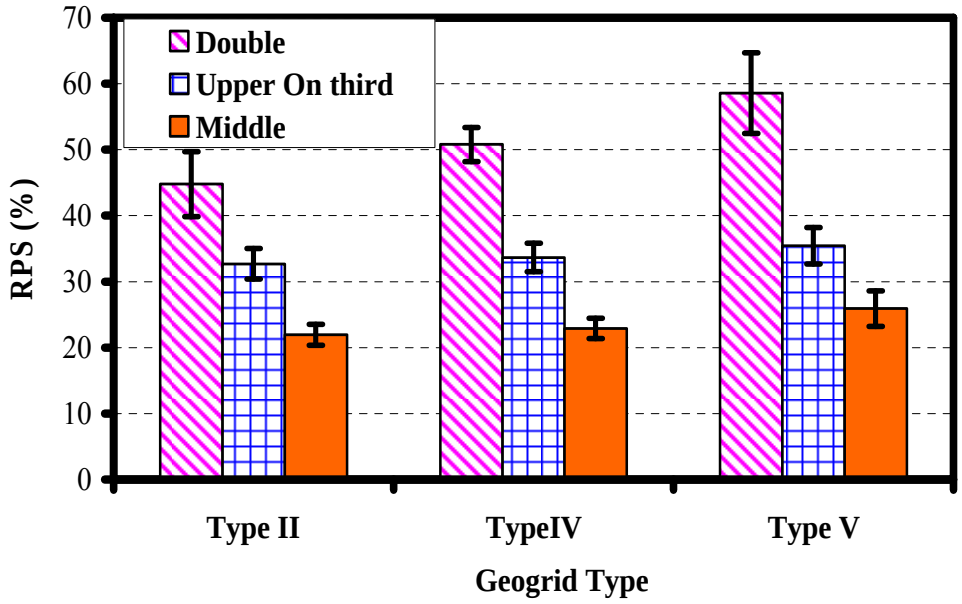

Figure 35
RPS at 10,000 of load cycles for crushed limestone II

ANOVA analysis was conducted to evaluate the effect of geogrid stiffness and geogrid arrangement on RPS% at different number of load cycles. The results showed that at a 95 percent confidence level the geogrid stiffness, geogrid arrangement, and number of load cycles had significant effect on the reduction of permanent deformation. The geogrid arrangement was the most significant factor affecting the geogrid benefit values, while the geogrid stiffness had a more significant effect than the number of load cycles. The geogrid stiffness-geogrid arrangement interaction ($\tau_1\tau_{2ij}$) had significant effects, which indicates that the effect of geogrid stiffness varied with the geogrid arrangement.

Furthermore, the geogrid arrangement-number of load cycle interaction was also significant. This may suggest that the improvement for the different geogrid arrangements depends on the number of load cycles applied.

Based on the results of the ANOVA analyses, post ANOVA-LSM analyses were conducted to compare the different level for each effect. Table 14 through Table 17 present the results of post ANOVA-LSM analyses conducted on reinforced crushed limestone I; Table 18 through Table 20 presents the results of post ANOVA-LSM analyses conducted on reinforced crushed limestone II.

Table 14 and 18 present the grouping of geogrid stiffness effect for crushed limestone I and II, respectively. The maximum and minimum improvements were achieved when using geogrids Type V and II, respectively. These two geogrid types have the highest and the lowest stiffness, respectively. This finding agrees with the results from large-scale reinforced pavement test sections reported in different studies, which showed that high modulus geogrids provides better improvement to the stress distribution transferred to the subgrade and the surface permanent deformation compared to low modulus geogrids *[36]*, and *[38]*.

Table 15 and 19 present the grouping of the effect of the geogrid arrangement on the reduction in permanent deformation for crushed limestone I and II, respectively. It is clear that the double arrangement has a much greater LSM value of RPS compared to other arrangement, while the lowest LSM value of RPS, and the least improvement, is observed for the middle arrangement.

Table 16 and 20 compare the geogrid benefits at different number of load cycles for crushed limestone I and II, respectively. It is noted that improvement due to the geogrid was minimal values at 100 load cycles, and it increased significantly at the 1000^{th} cycle, eventually stabilizing after about 5000 load cycles.

Table 14
Grouping of geogrid type effect on RPS of crushed limestone I samples

Geogrid Type /Stiffness	Estimate of RPS%	Letter Group
Type V	41.1884	A
Type IV	32.0782	B
Type II	28.4862	C

Table 15
Grouping of geogrid arrangement effect on RPS of crushed limestone I samples

Arrangement	Estimate of RPS%	Letter Group
Double	49.5864	A
Upper one-third	29.6158	B
Middle	22.5507	C

Table 16
Grouping of cycle effect on RPS of crushed limestone I samples

Number Of Cycle	Estimate of RPS%	Letter Group
10000	40.1189	AB
5000	38.0126	B
1000	34.6196	C
100	19.8689	D

Table 17 presents the grouping of geogrid type-arrangement interaction effect on RPS for crushed limestone I. It was noticed that the highest improvements was always achieved when using two geogrid layers, while the lowest improvement was achieved when using a single geogrid layer placed at the sample mid-height**.**

Table 17
Grouping of geogrid type-arrangement interaction effect on RPS of crushed limestone I samples

Arrangement	Geogrid Type	Estimate	Letter Group
Double	Type V	60.1400	A
Double	Type IV	49.3747	B
Double	Type II	39.2447	C
Upper one-third	Type V	34.8240	D
Upper one-third	Type II	29.4260	E
Middle	Type V	28.6013	E
Upper one-third	Type IV	24.5973	F
Middle	Type IV	22.2627	F
Middle	Type II	16.7880	G

Table 18
Grouping of geogrid stiffness (crushed limestone II)

Geogrid Type /Stiffness	Estimate of RPS%	Letter Group
Type V	30.89	A
Type IV	25.20	AB
Type II	21.95	C

Table 19
Grouping of geogrid arrangement (crushed limestone II)

Arrangement	Estimate of RPS%	Letter Group
Double	42.73	A
Upper one-third	25.04	B
Middle	10.26	C

Table 20
RPS at different number of cycles (crushed limestone II)

Number of Cycles	Estimate of RPS%	Letter Group
10,000	36.30	A
5000	33.16	AB
1000	21.16	C
100	9.70	D

The single stage RLT test results clearly demonstrated that the inclusion of geogrid reinforcement within base course material samples resulted in a reduction in the permanent deformation accumulating under cyclic loading. This improvement can be attributed to the increase in the lateral confinement due to the presence of geogrid reinforcement. The stiffness of the geogrid is a key factor in doing this. However, looking at the results of the statistical analysis reveals that the geogrid stiffness was the least significant factor affecting the reduction in permanent deformation. Thus, the reduction in the permanent deformation cannot only be explained by the apparent confining pressure caused by the stiffness of the geogrid. This agrees with the findings of Konietzky et al., who indicated that only 10 percent of the permanent deformation reduction can be attributed to the geogrid stiffness *[56]*.

Many studies indicate that the dominant geogrid reinforcement mechanism in a pavement structure is interlocking *[56]*, *[57]*, and *[58]*. Interlocking is caused by the interaction between the aggregates and the geogrid (e.g., traverse ribs of geogrid). McGown et al. also recognized the existence of a dynamic geogrid–aggregate interlock mechanism under cyclic loading *[57]*, *[59]*. Recently, a discrete element analyses (DEM) of the geogrid reinforced samples demonstrated that the greatest effect of geogrid interlocking occurs in the immediate vicinity of the geogrid, extending to approximately 10 cm on either side of the geogrid *[60]*. Beyond that, the interlocking effect is restricted only to the central part of the cross-section. This may explain why the highest improvement in this study was achieved when reinforcing the crushed limestone samples with two geogrid layers were placed at 10 cm apart.

The results of the statistical analyses demonstrated that the improvement due to the geogrid reinforcement was small during the primary post-compaction stage; however, it significantly increased after that in the secondary stage. This can be explained by the fact that the geogrid improvement mainly results from the confinement effect caused by the geogrid-aggregate interlocking, so it is expected to mainly contribute to the rotation and sliding mechanisms of the aggregate particles, which are mostly dominant in the secondary stage.

Figure 36 and Figure 37 present the average resilient strain curves for unreinforced crushed limestone I and II samples and samples reinforced with geogrid Type II. The resilient strain had a similar trend in both reinforced and unreinforced samples, in that it decreased with increasing the number of load cycles until reaching an asymptote and then maintaining the same magnitude for the rest of the test, hence reaching a steady resilient response. The reason for this behavior is that in the primary post-compaction stage the

sample accumulates more deviatoric strain in the horizontal direction (perpendicular to the direction on which the cyclic load is applied), causing the Poisson ratio to decrease slightly. This will cause an increase in the samples' stiffness, hence causing a decrease in the resilient strain. The number of cycles needed for the sample to reach a steady resilient response increases as the imposed deviatoric stress is increased.

It can be noticed the crushed limestone I samples reached the steady resilient state at a lower number of load cycles (1000 cycles) compared to crushed limestone II samples (5000 cycles).

The figures also demonstrate that the geogrids did not have a significant effect on the resilient behavior of the crushed limestone samples. This result is consistent with the recent work reported by Moghaddas-Nejad and Small, and Perkins et al. where similar test results were reported on different granular materials (silica sand and aggregates) reinforced with geogrid layers *[33]*, *[47]*. The reason for this behavior is that the resilient deformation of a granular material is primarily due to the deformation of individual grains *[61]*. However, the presence of geogrids did not alter the deformation of individual grains significantly, thus they do not have a great contribution to the resilient deformation behavior of reinforced samples.

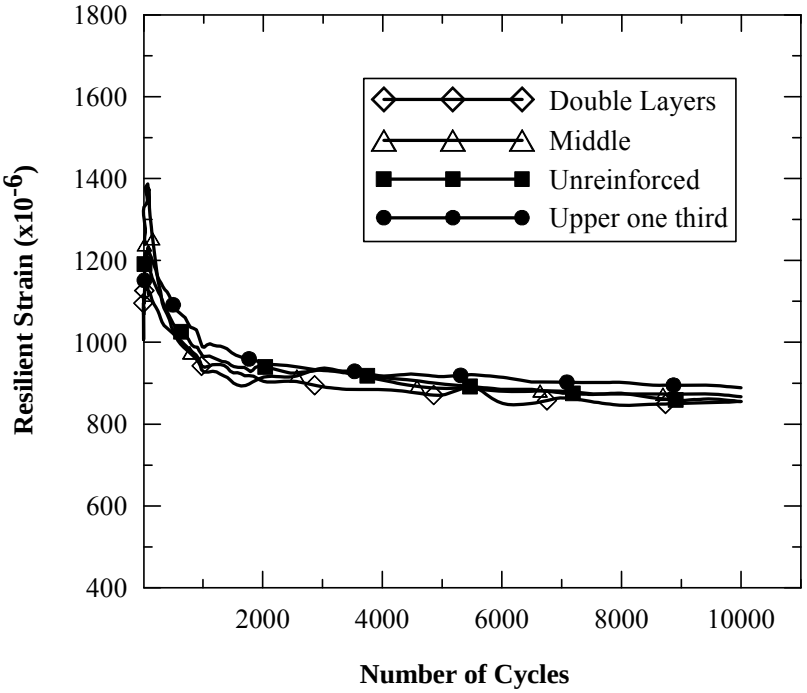

Figure 36
Resilient deformation curves of crushed limestone I samples reinforced with geogrid Type II

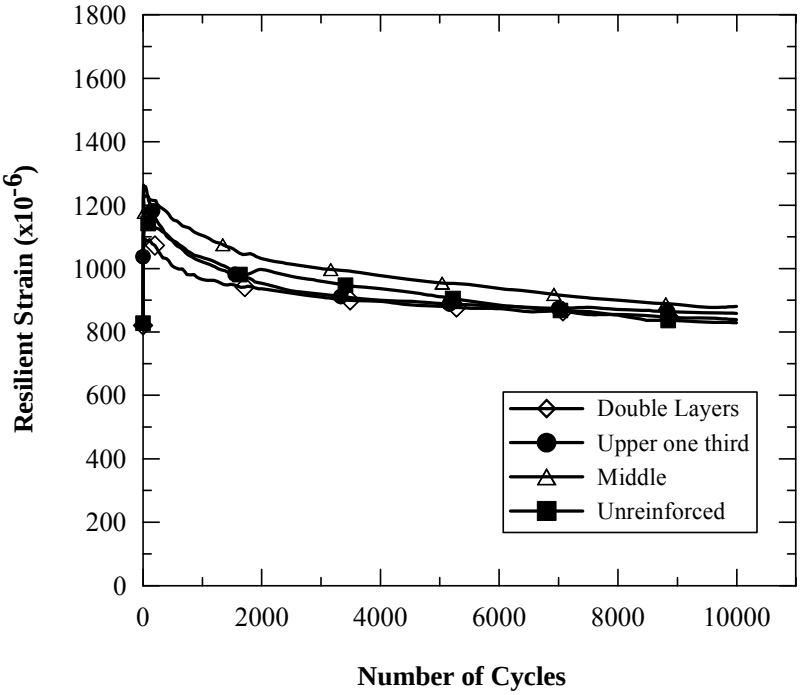

Figure 37
Resilient deformation curves of crushed limestone II samples reinforced with geogrid Type II

Numerical Modeling of Geogrid Reinforced

This section presents the results of the numerical modeling study that was conducted to capture the impacts of the base course layers' parameters reflected by the granular base thickness and subgrade strength as well as the stiffness and location of the geogrid reinforcement layer on the structural performance of geogrid reinforced flexible pavement systems.

Results of Finite Element Analysis

The following sections summarize the results of the finite element analysis conducted in crushed limestone I and II. The responses of different pavement sections computed from finite element analysis are used to evaluate the performance of those sections.

Stresses and Strain (Effect of Geogrid Reinforcement Placed at Bottom of Base Layer). Vehicular loads applied at the surface of a pavement section create a lateral spreading motion of the base course aggregate. As a result, tensile lateral strains are created in the base below the applied load as the material moves down and away from the load. Lateral movement of the base allows for vertical strains to develop, leading to a permanent deformation in the wheel path. One of the main reinforcement mechanisms attributed to geosynthetics in paved roads is the direct prevention of lateral spreading of base course aggregate, which is called lateral restraint mechanism *[48]*. Figure 38 through Figure 41 present the profiles of lateral strain computed at different distance from the center of the wheel load for sections 1a, 5a, and 5c of crushed limestone I reinforced with one layer of geogrid Type I and IV and sections 1a and 5c of crushed limestone II, reinforced with one layer of geogrid Type I and III, respectively. The figures show that the geogrid reinforcement constrained the lateral motion of aggregate up within the base course layer and down within the subgrade layer. The maximum reduction in the lateral strain was observed at the base-subgrade interface. It is clear that the geogrid effect was mainly below the wheel load area and almost vanished at a distance of 304 mm from the center of the wheel load. The geogrid lateral constrain effect was more dominant in sections built with thin base course layer on top of weak subgrade layers, such as section 1a. This demonstrates that the geogrid effect on reducing the lateral tensile strain is controlled by the thickness of the base course layer and the stiffness of subgrade. However, the figures show that the subgrade stiffness has greater influence in this case. The figures also demonstrate that higher stiffness geogrids provided much greater reduction in lateral tensile strain.

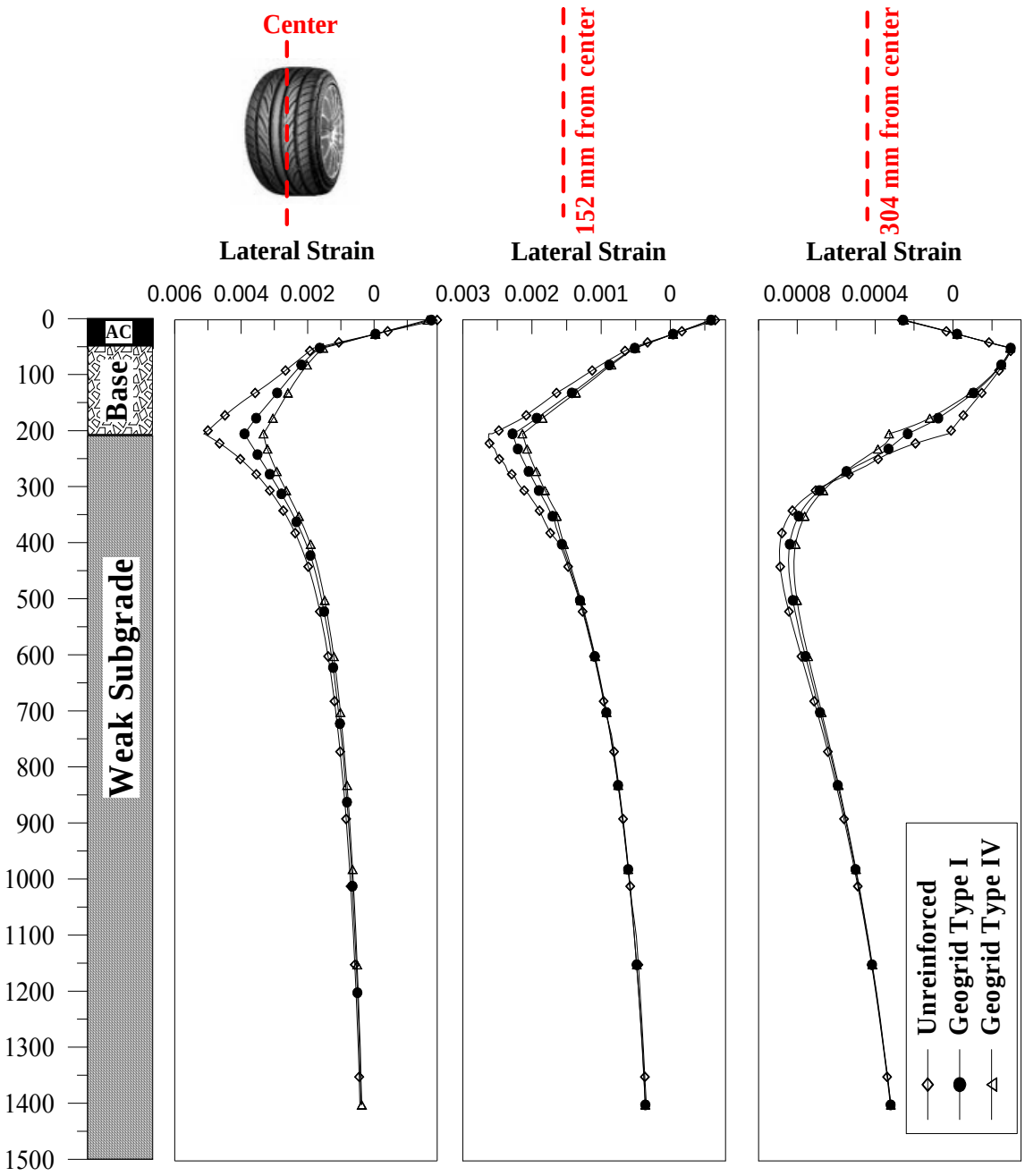

Figure 38
Lateral strain profile for unreinforced section 1a and reinforced with geogrid layer placed at the bottom of the base layer for crushed limestone I

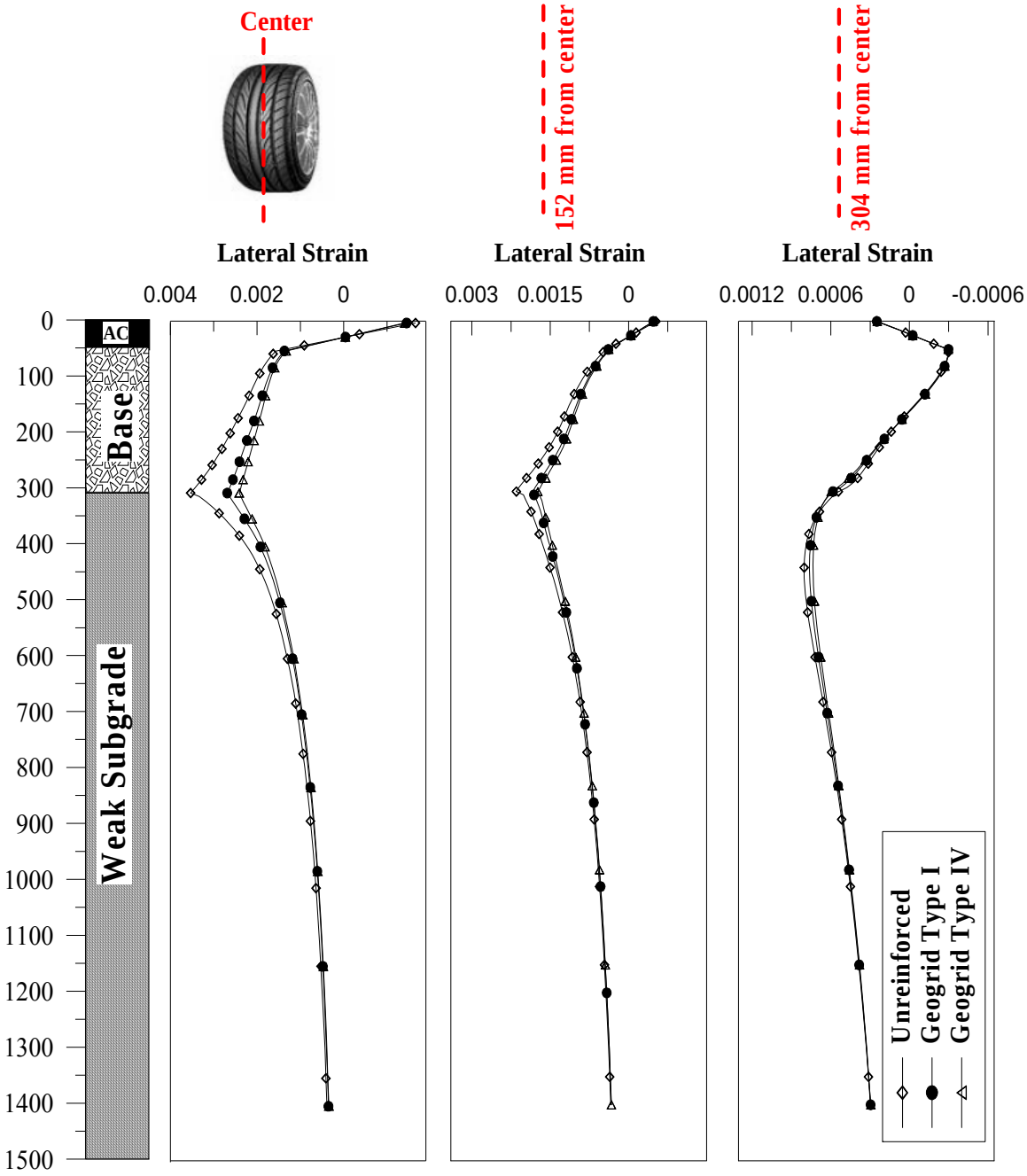

Figure 39
Lateral strain profiles for unreinforced section 5a and reinforced with geogrid layer placed at the bottom of the base layer for crushed limestone I

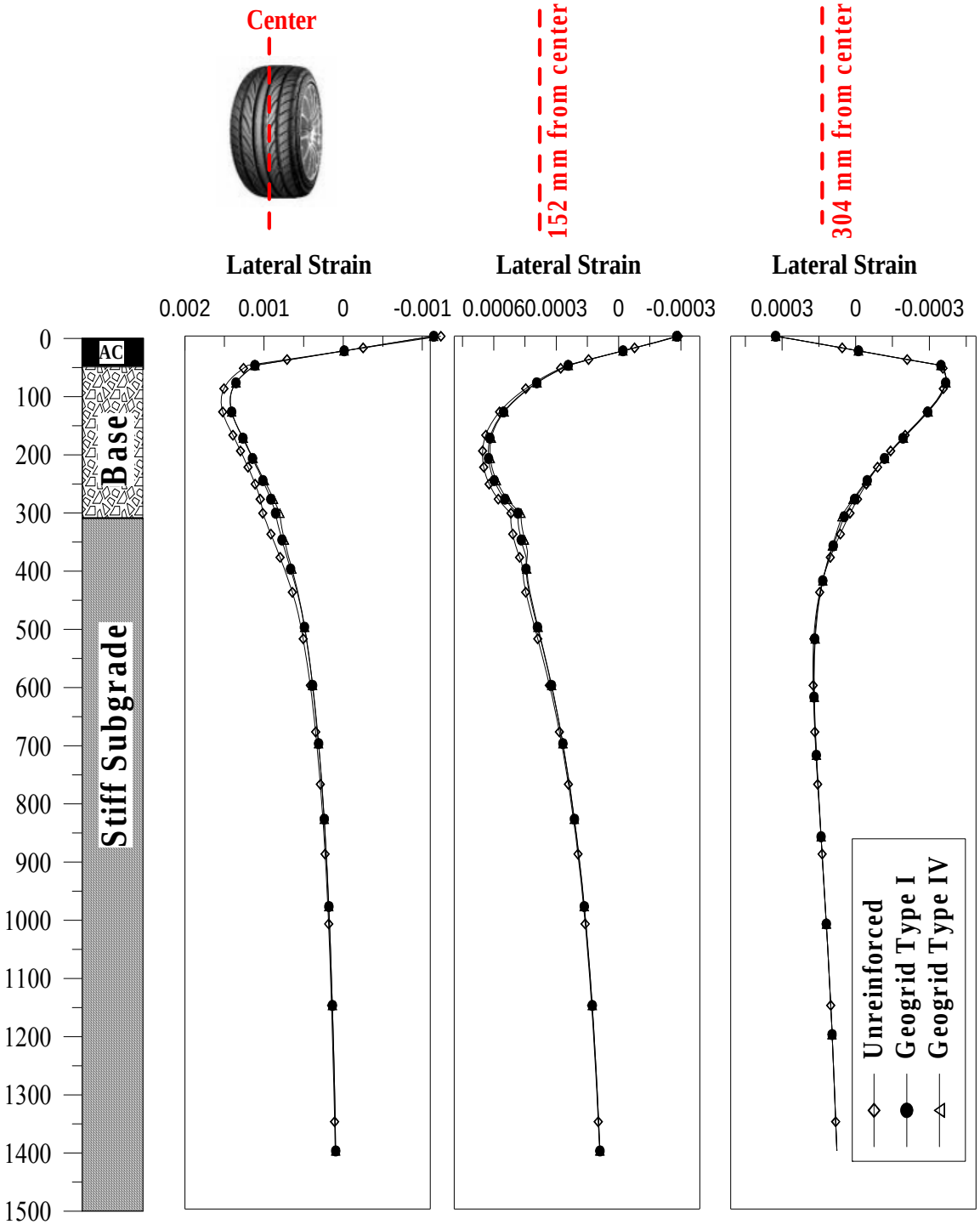

Figure 40
Lateral strain profile for unreinforced section 5c and reinforced with geogrid layer placed at the bottom of the base layer for crushed limestone I

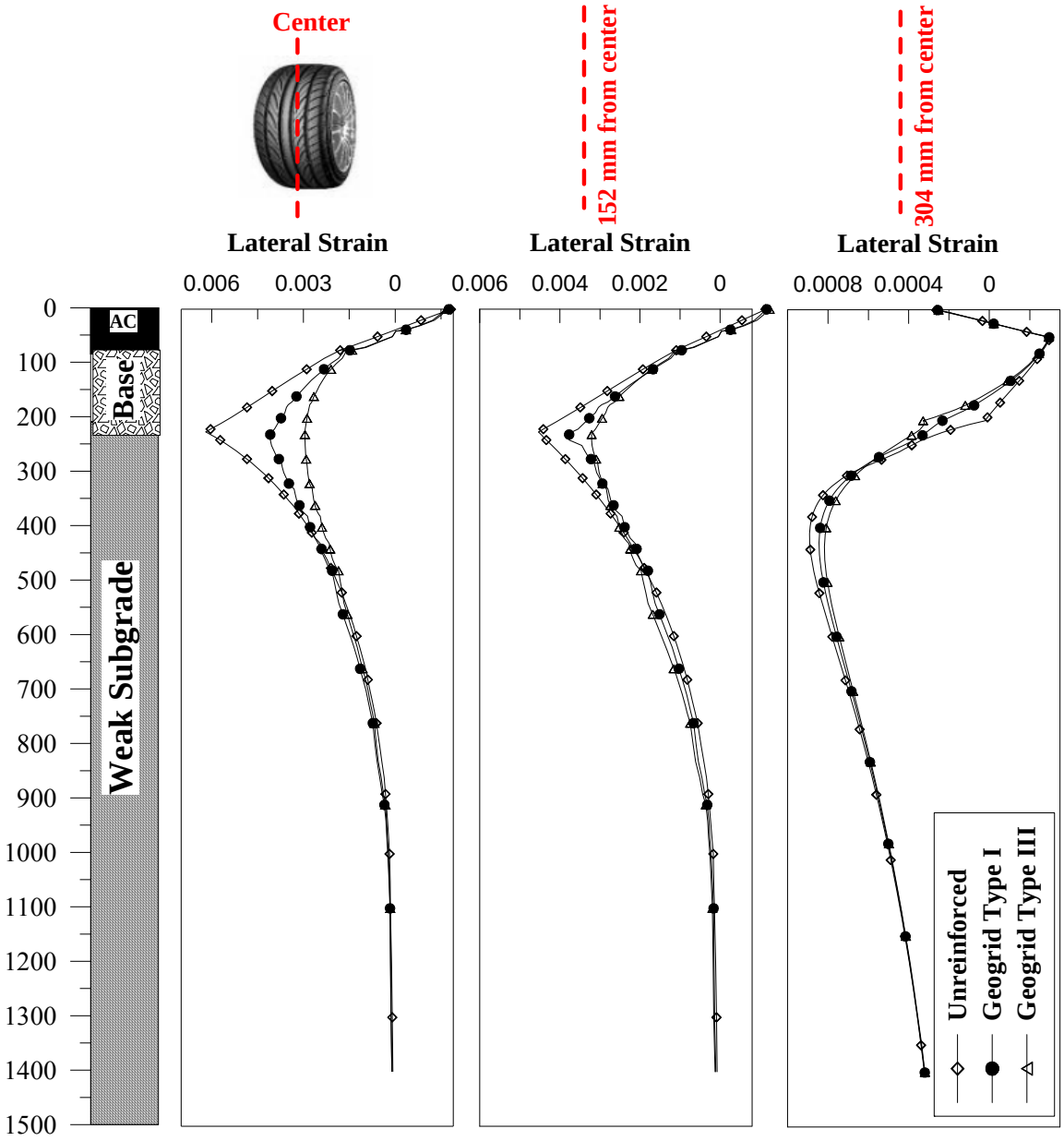

Figure 41
Lateral strain profile for unreinforced section 1a and reinforced with geogrid layer placed at the bottom of the base layer for crushed limestone II

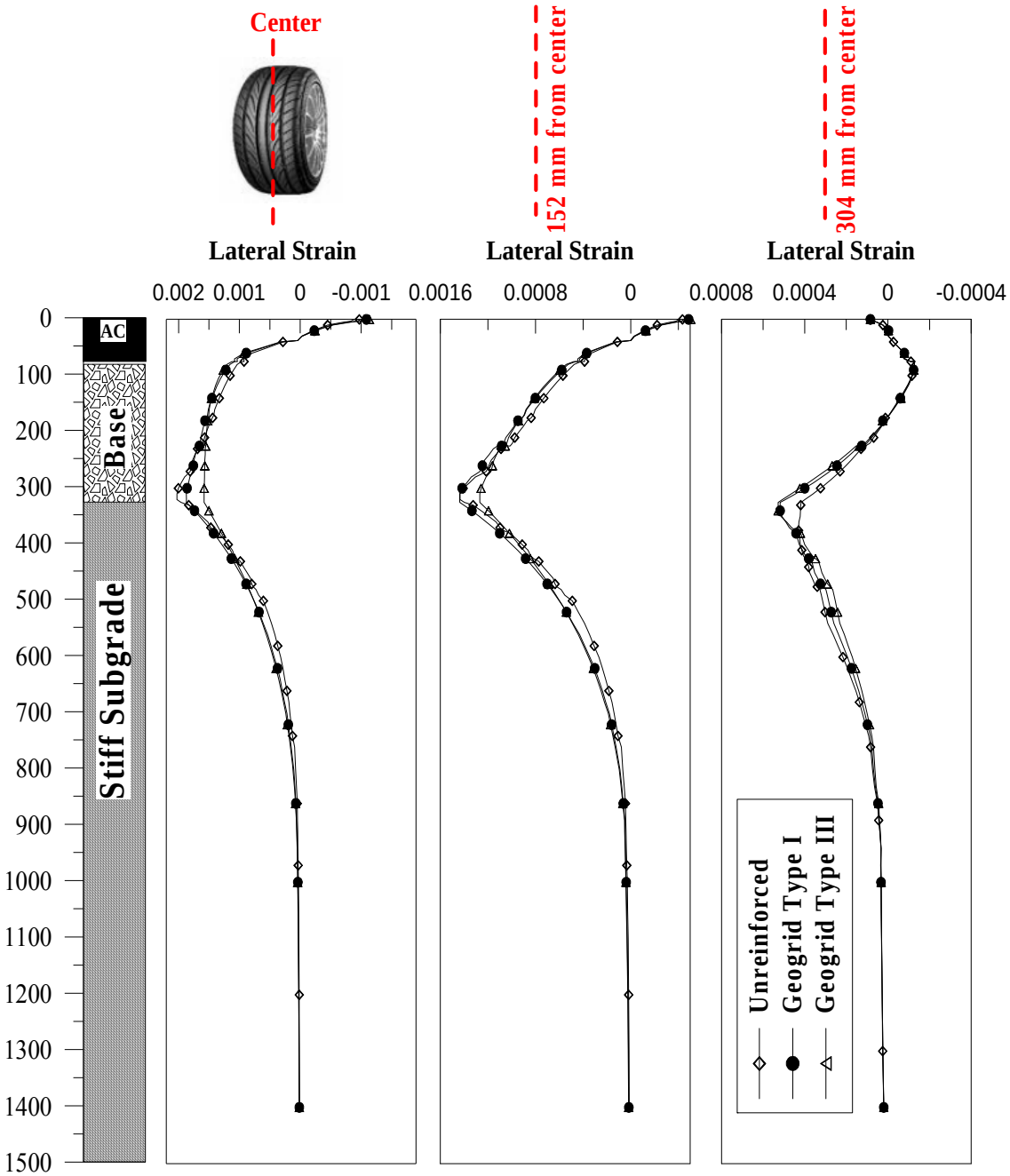

Figure 42
Lateral strain profile for unreinforced section 5c and reinforced with geogrid layer placed at the bottom of the base layer for crushed limestone II

The vertical strains profiles predicted from the finite element analysis at different locations within the subgrade layer for unreinforced and reinforced crushed limestone I sections 1a, 5a, and 5c and crushed limestone II sections 1a and 5c are shown in Figure 43 through Figure 47, respectively. The geogrid layer resulted in a significant reduction in the vertical strain at the top of subgrade. However, this reduction is influenced by the

base course thickness and subgrade stiffness, such that a greater reduction is noticed for weaker subgrade and thinner base course layers. Furthermore, the geogrid influence on the vertical strain was experienced within zone that extends to a depth of about 304 mm below the top of the subgrade layer. However, the greatest influence was encountered at the top of the subgrade. The figures also clearly demonstrate the effect of geogrid stiffness on the induced vertical strain, such that stiffer geogrids exhibited lower vertical strain at top of the subgrade.

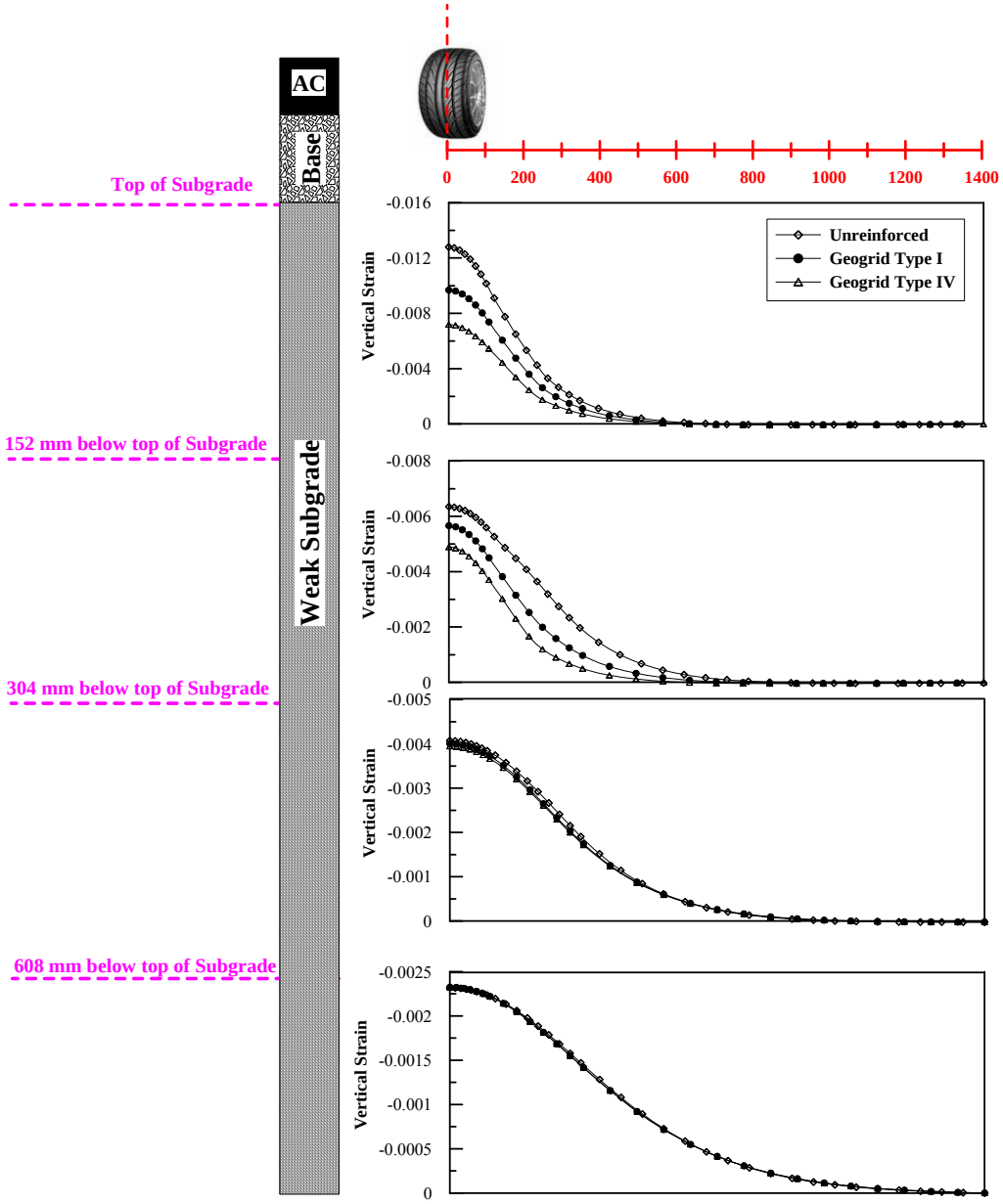

Figure 43
Vertical strain profiles within subgrade layer for section 1a of crushed limestone I with one geogrid layer place at the bottom of the base layer

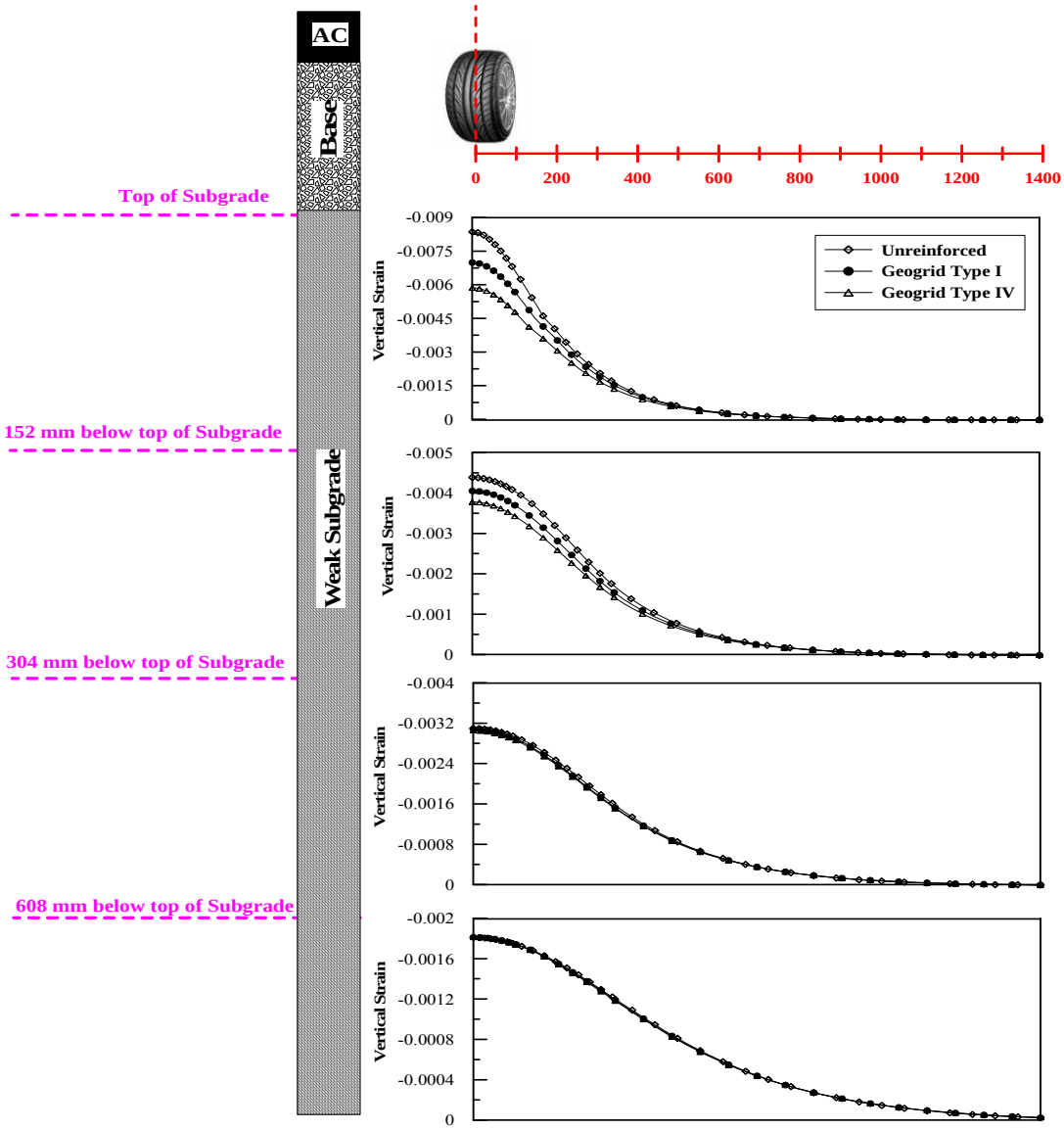

Figure 44
Vertical strain profiles within subgrade layer for section 5a of crushed limestone I with one geogrid place at the bottom of the base layer

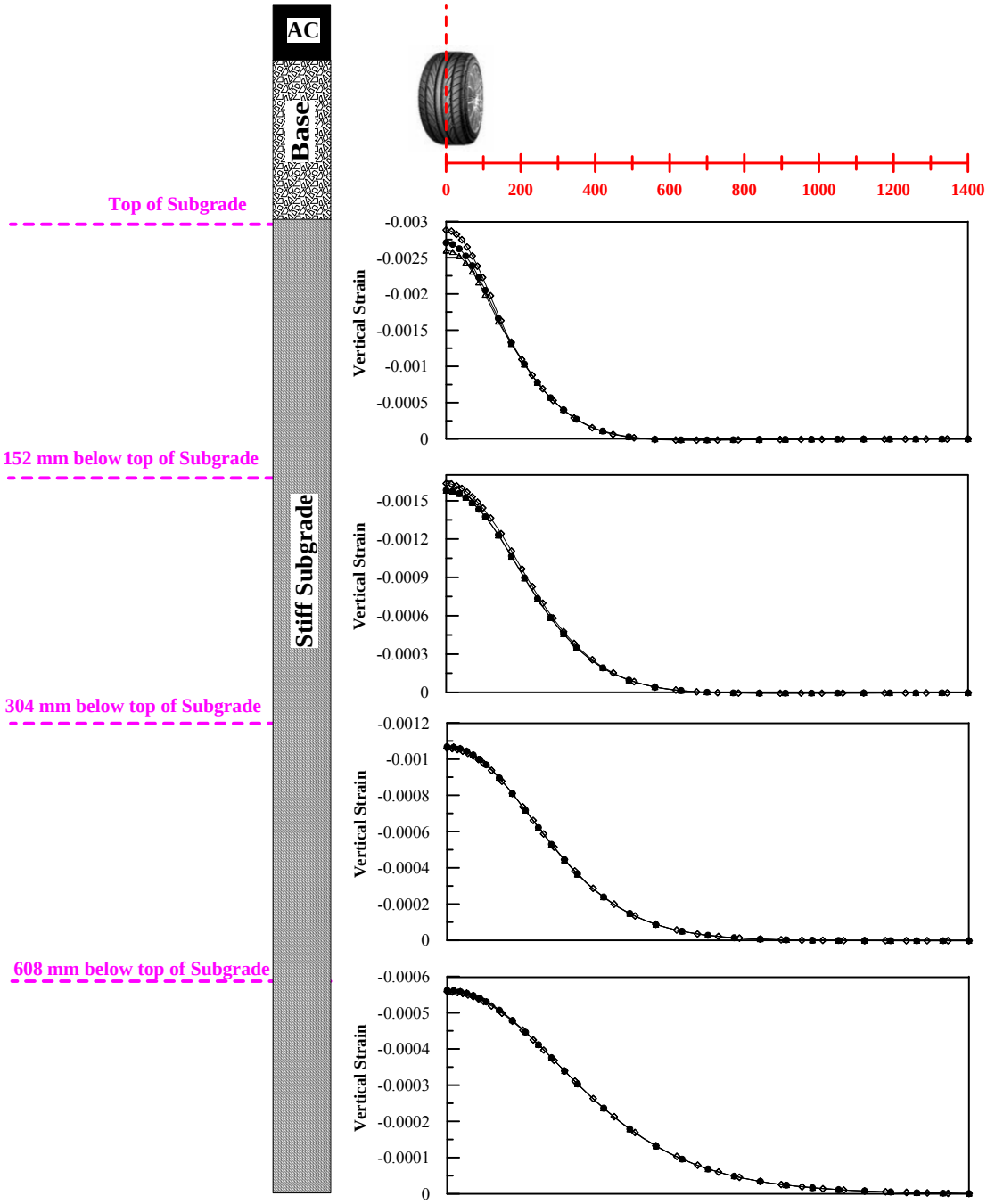

Figure 45
Vertical strain profiles within subgrade layer for section 5c of crushed limestone I with one geogrid place at the bottom of the base layer

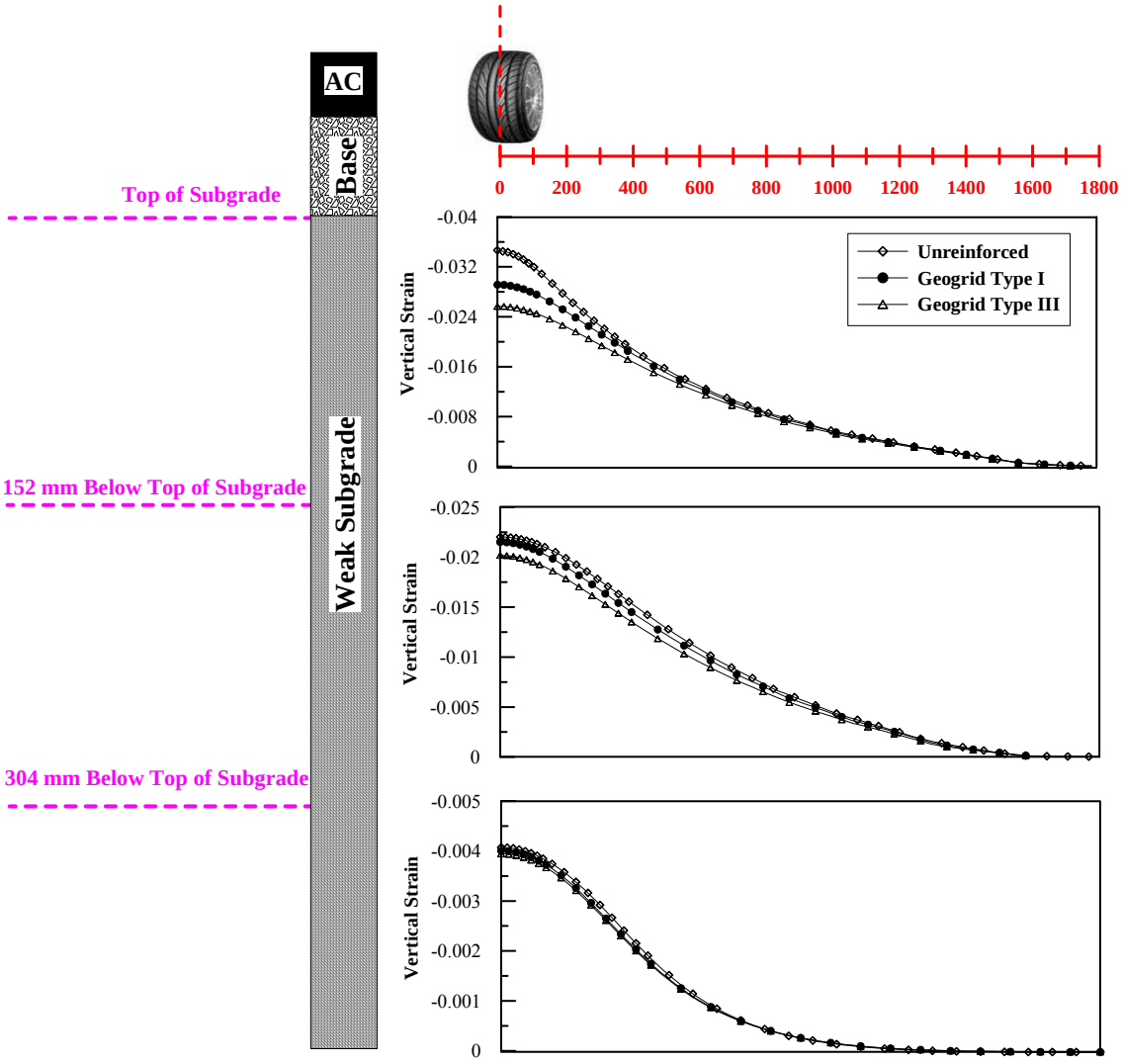

Figure 46
Vertical strain profiles within subgrade layer for section 1a of crushed limestone II with one geogrid place at the bottom of the base layer

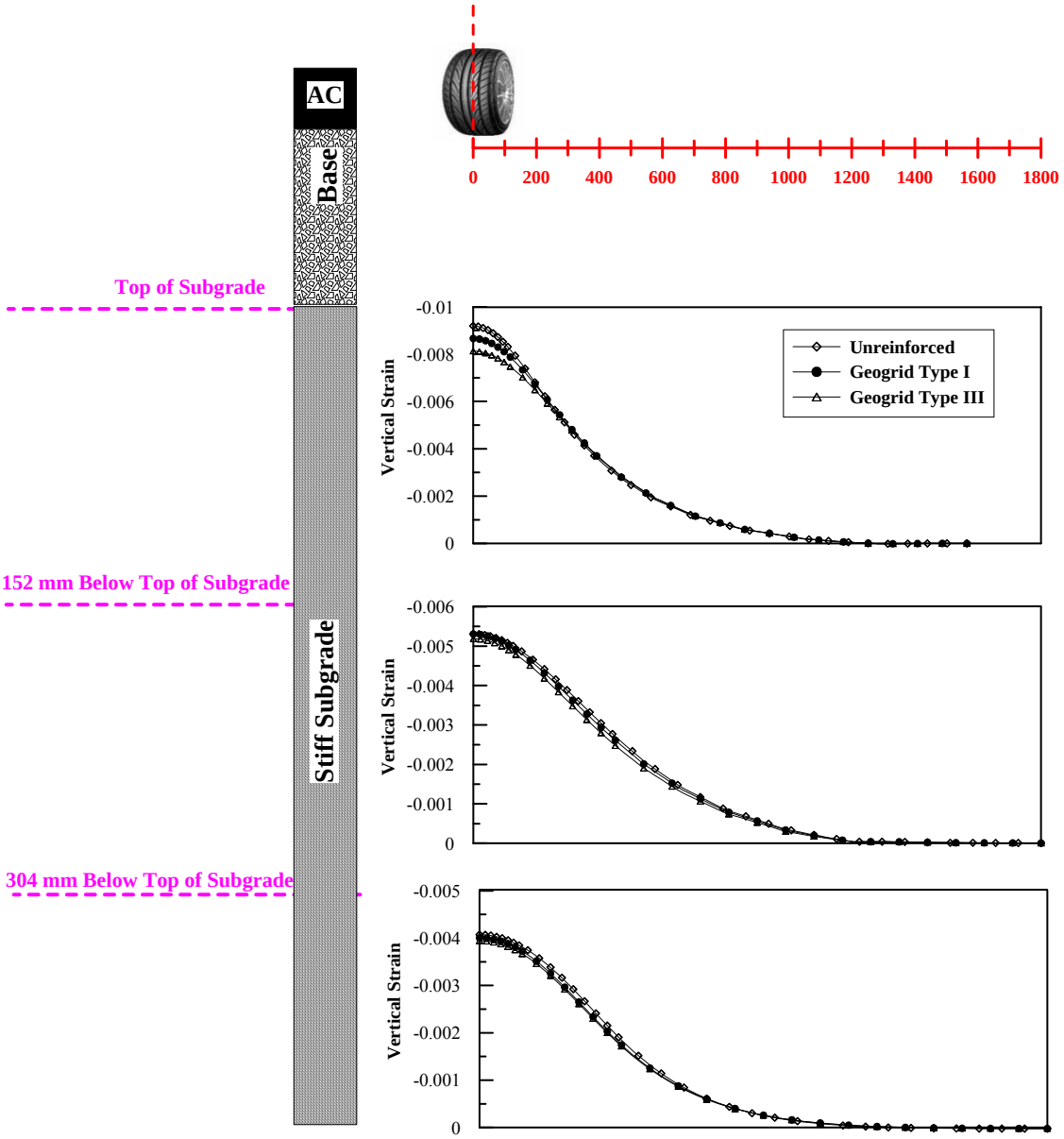

Figure 47
Vertical strain profiles within subgrade layer for section 5c of crushed limestone II with one geogrid place at the bottom of the base layer

Figure 48 and 49 show the vertical stress profile at the top of the subgrade layer for sections 1a, and 5a, respectively. It is noted that slight/no improvement in the vertical stresses was detected at the top of subgrade layer due to the geogrid reinforcement. Figure 50 and 53 present the plastic strain distribution at the top of subgrade for section 1a and 5a of crushed limestone I and sections 1a and 5c of crushed limestone II, respectively. It can be seen that the plastic strains obtained for the unreinforced section was much greater than those obtained for reinforced sections. This indicates that although

the unreinforced section had larger vertical strains, the elastic portion of this strain that contributes to the stress is much less. This suggests that the geogrid layer influence is more pronounced on the development of the plastic strains than the resilient strain.

Many studies indicated that the geogrid reinforcement benefits can be attributed to the reduction of shear strain at top the subgrade soil *[2]*, *[48]*, and *[38]*. Figure 54 and 55 present the shear strain distributions at the top of the subgrade layer for sections 1a and 5a, respectively, while Figure 56 and 57 present the shear strain distribution at the top of the subgrade layer for sections 1a and 5c, respectively. The geogrid resulted not only in decreasing the shear strains at the top of the subgrade layer, but also in providing a better distribution of these strains. This is expected since the shear strain transmitted from the base course layer to the subgrade would decrease as shearing of the base transmits tensile load to the geogrid reinforcement.

Stresses and Strain (**Effect of Geogrid Location).** Figure 58 presents the lateral strain profiles computed at different distances from the center of the wheel load for section 1a reinforced with a geogrid Type IV layer placed at the different locations. In general, there is slightly more reduction in the lateral strain at the AC-base course layer interface when placing the geogrid layer at the upper one-third locations compared to the other location; however, the bottom location had greater reduction within lower parts of the base course layer. Beyond a distance of 300 mm from the wheel load center, the geogrid location had no effect on the lateral strains, mainly since the geogrid layer did not have any contribution to the lateral strain beyond this point. Figure 59 shows the vertical profile strain computed at different depths within the subgrade layer for section 1a reinforced with a geogrid Type IV layer placed at different locations considered. It is noted that sections reinforced with a geogrid layer placed at the bottom of the base course had much greater reduction in vertical strain when compared to other locations.

Figure 60 presents the profile of vertical plastic strain obtained at the top of the subgrade layer for section 1a reinforced at the different locations considered. It can be seen that among all the locations considered, the bottom location had the most efficient effect in reducing the vertical plastic strain. A similar observation was also noted in Figure 61 which shows the bottom geogrid location had the most efficient effect in reducing the shear strain distribution at the top of the subgrade layer for section 1a reinforced with a geogrid Type IV layer placed at different locations.

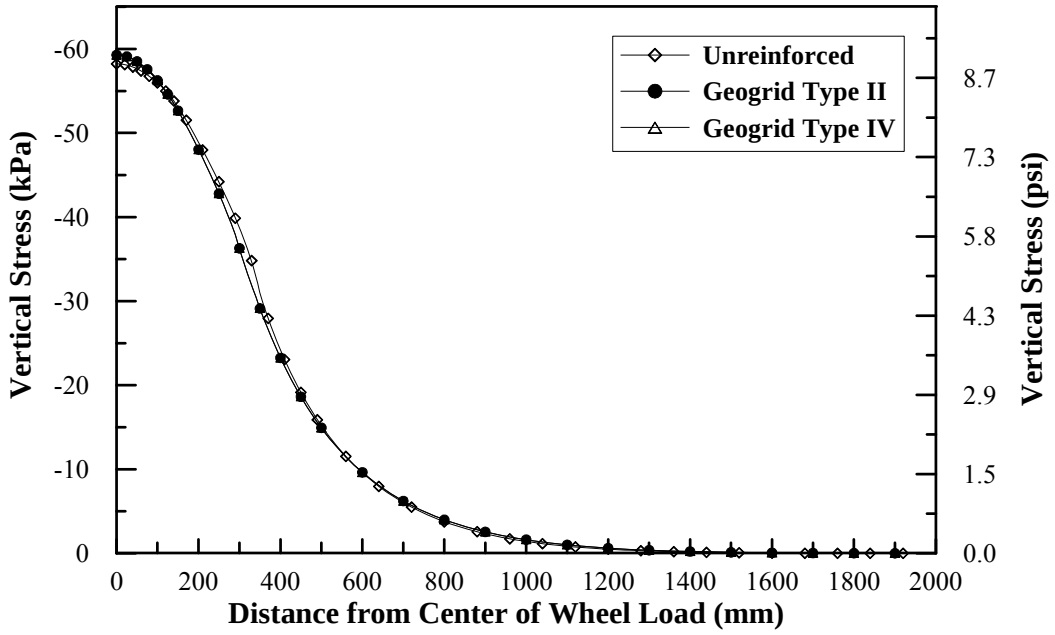

Figure 48
Vertical stress profile at top of subgrade layer for section 1a of crushed limestone I with one geogrid layer placed at the bottom of the base layer

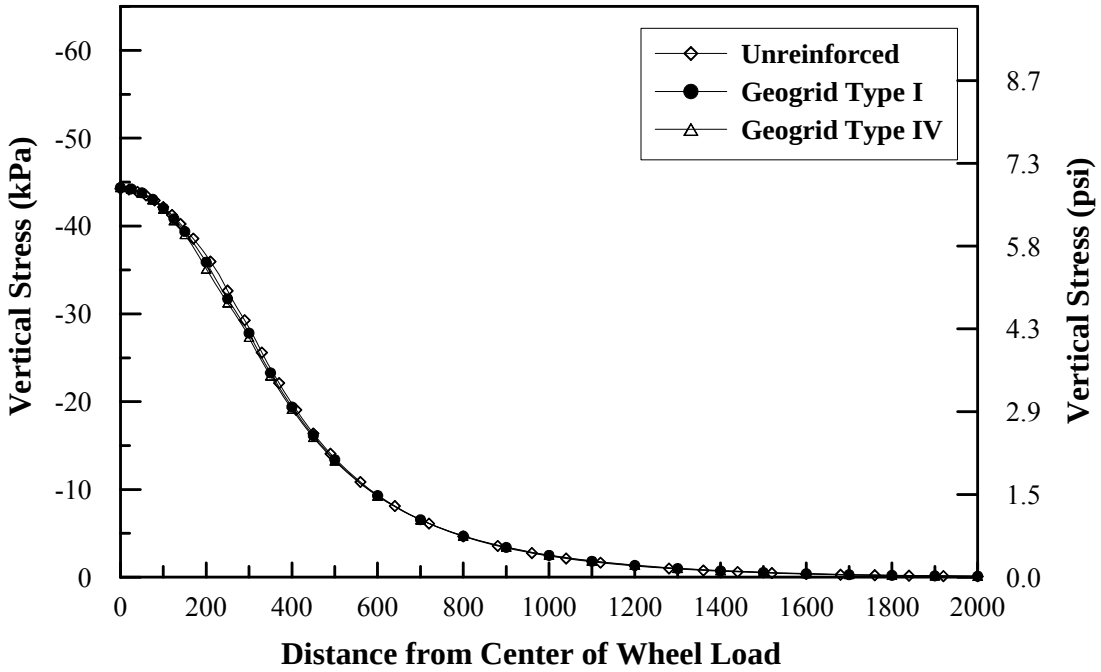

Figure 49
Vertical stress profile at top of subgrade layer for section 5a of crushed limestone I with one geogrid layer placed at the bottom of the base layer

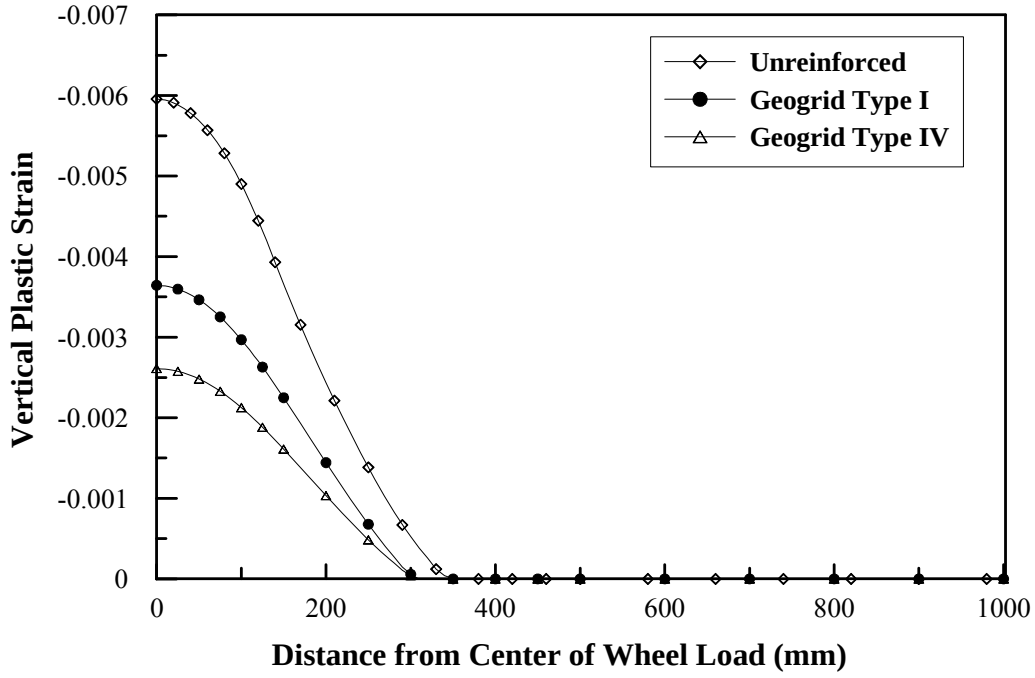

Figure 50
Vertical plastic strain profile at top of subgrade layer for section 1a of crushed limestone I with one geogrid layer placed at the bottom of the base layer

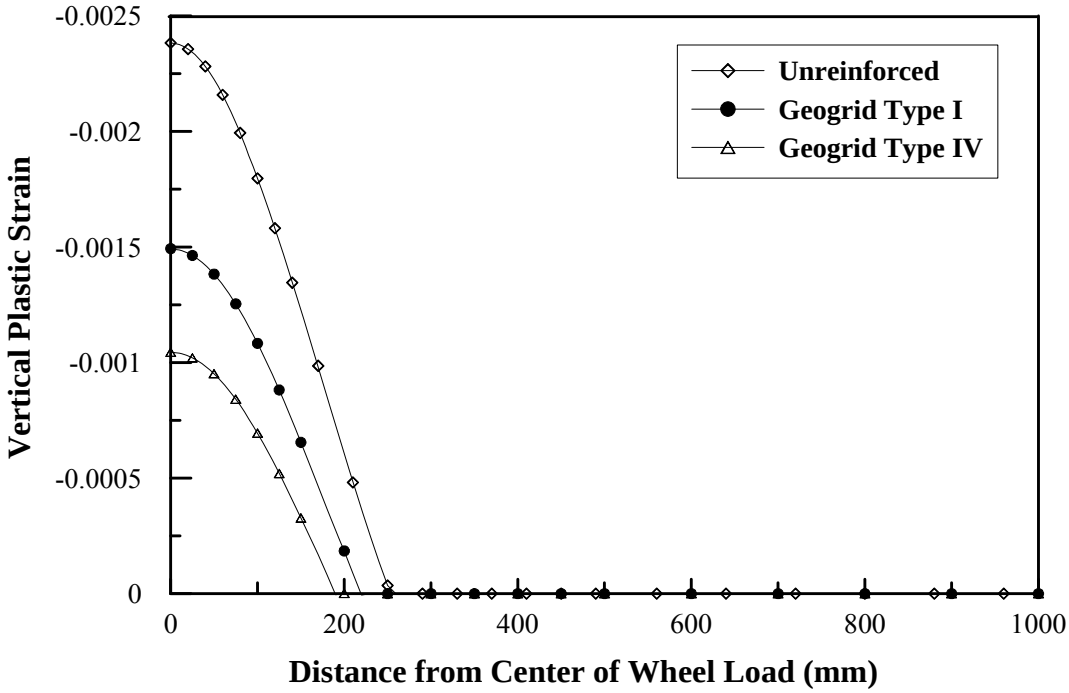

Figure 51
Vertical plastic strain profile at top of subgrade layer for section 5a of crushed limestone I with one geogrid layer placed at the bottom of the base layer

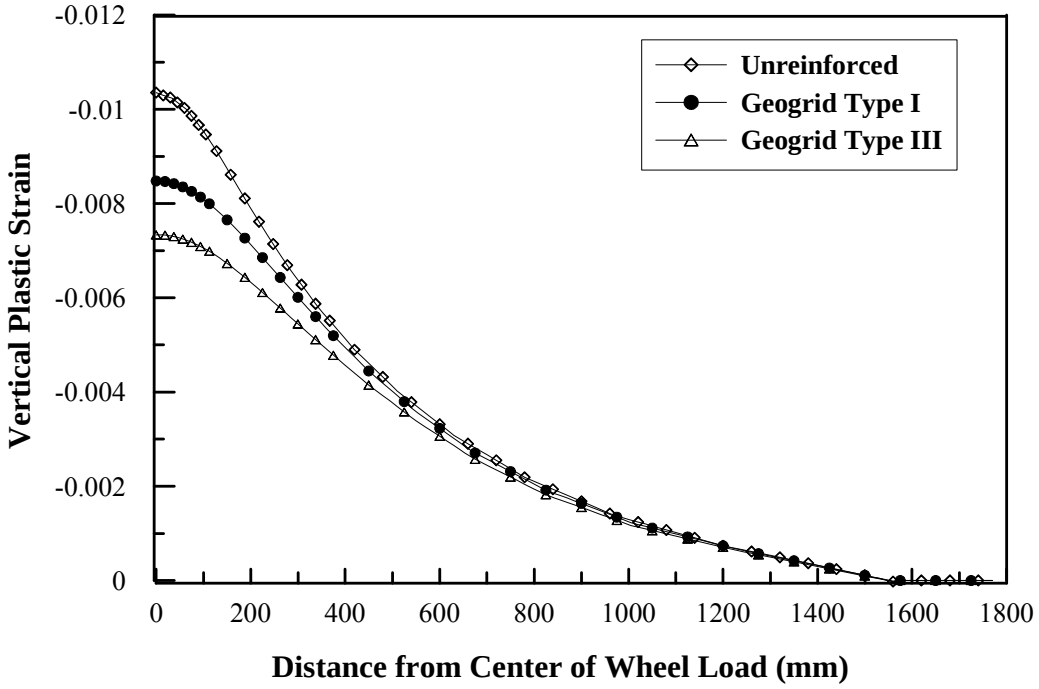

Figure 52
Vertical plastic strain profile at top of subgrade layer for section 1a of crushed limestone II with one geogrid layer placed at bottom of the base layer

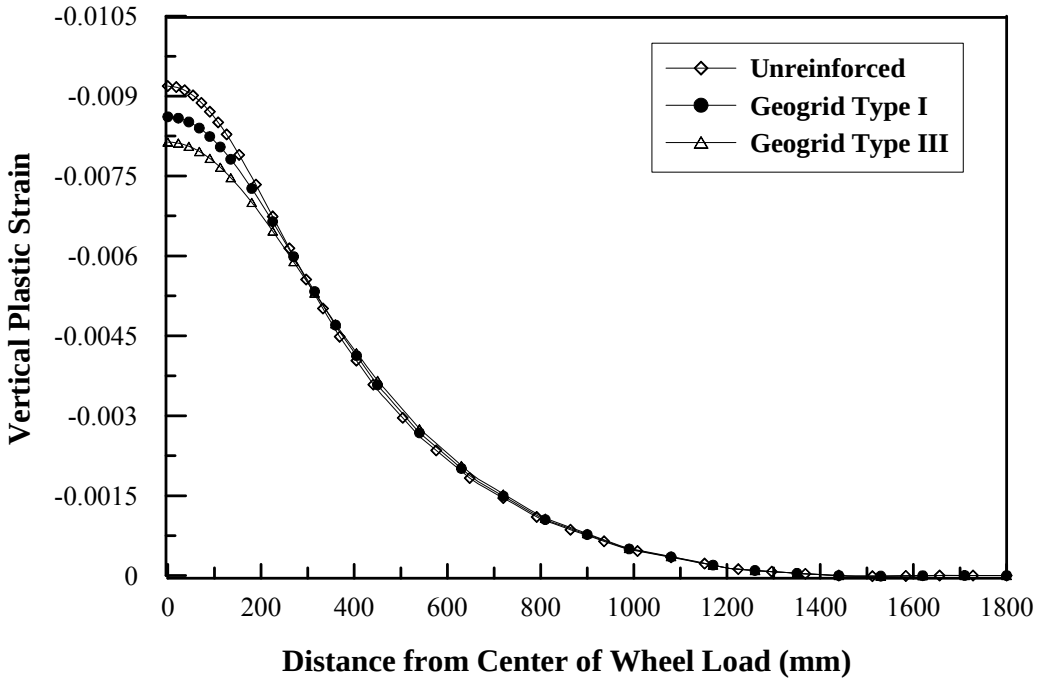

Figure 53
Vertical plastic strain profile at top of subgrade layer for section 5c of crushed limestone II with one geogrid layer placed at bottom of the base layer

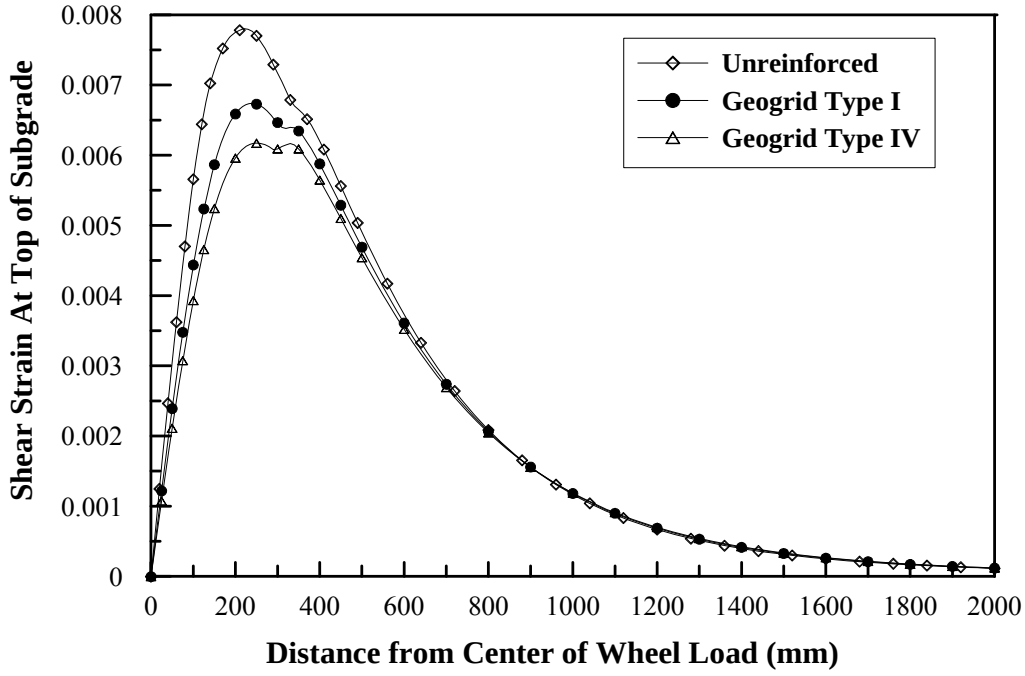

Figure 54
Shear strain profile at top of subgrade layer for section 1a of crushed limestone I with one geogrid layer placed at the bottom of the base layer

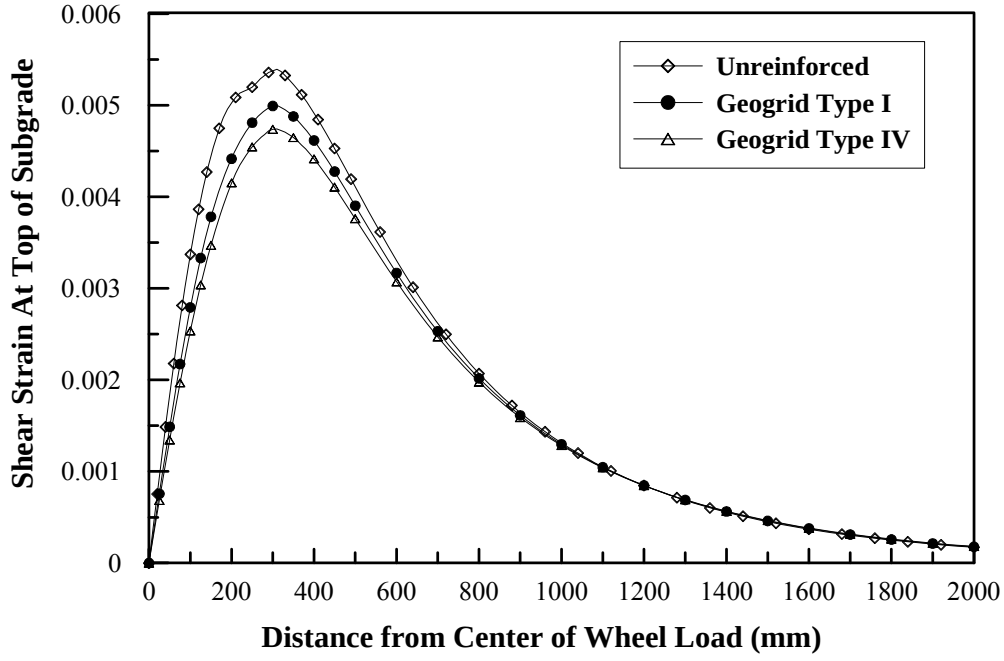

Figure 55
Shear strain profile at top of subgrade layer for section 5a of crushed limestone I with one geogrid layer placed at the bottom of the base layer

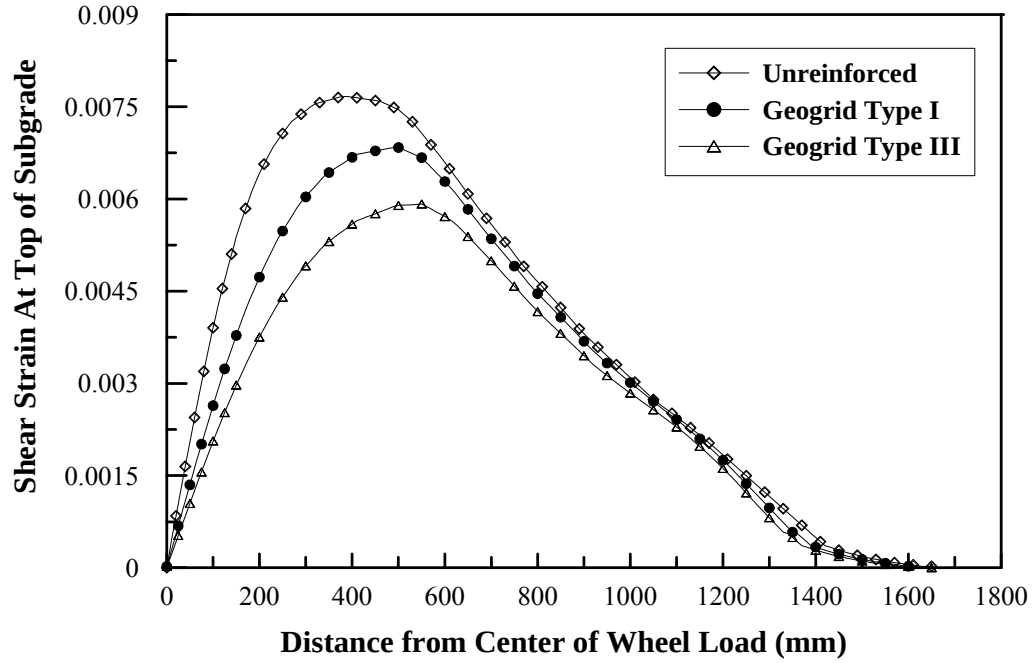

Figure 56
Shear strain profile at top of subgrade layer for section 1a of crushed limestone II with one geogrid layer placed at the bottom of the base layer

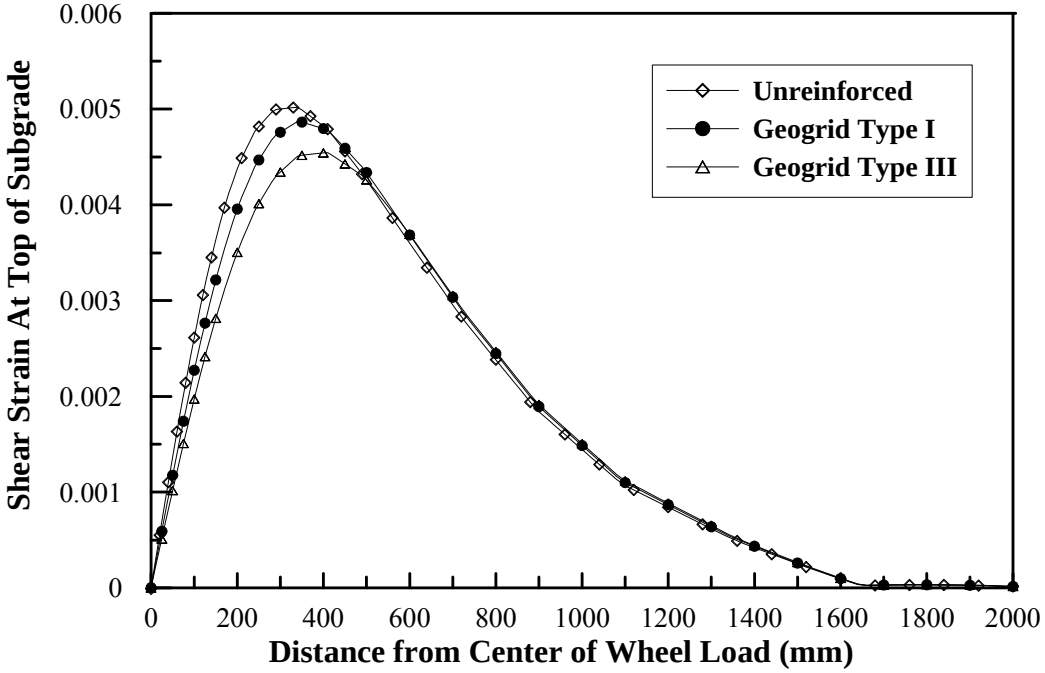

Figure 57
Shear strain profile at top of subgrade layer for section 5c of crushed limestone II with one geogrid layer placed at the bottom of the base layer

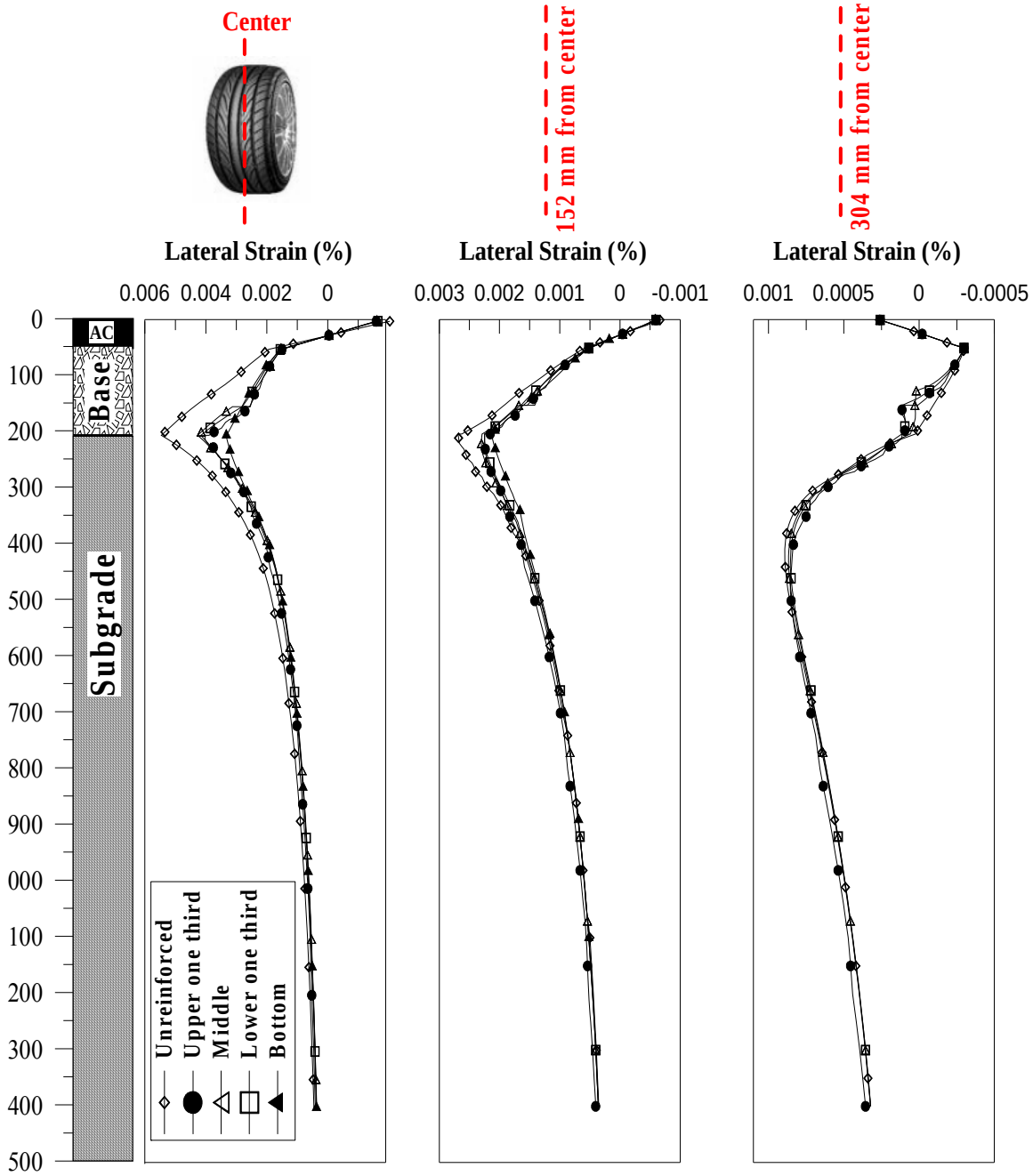

Figure 58
Lateral strain profile for unreinforced section 1a and reinforced with geogrid Type IV layer placed at different locations

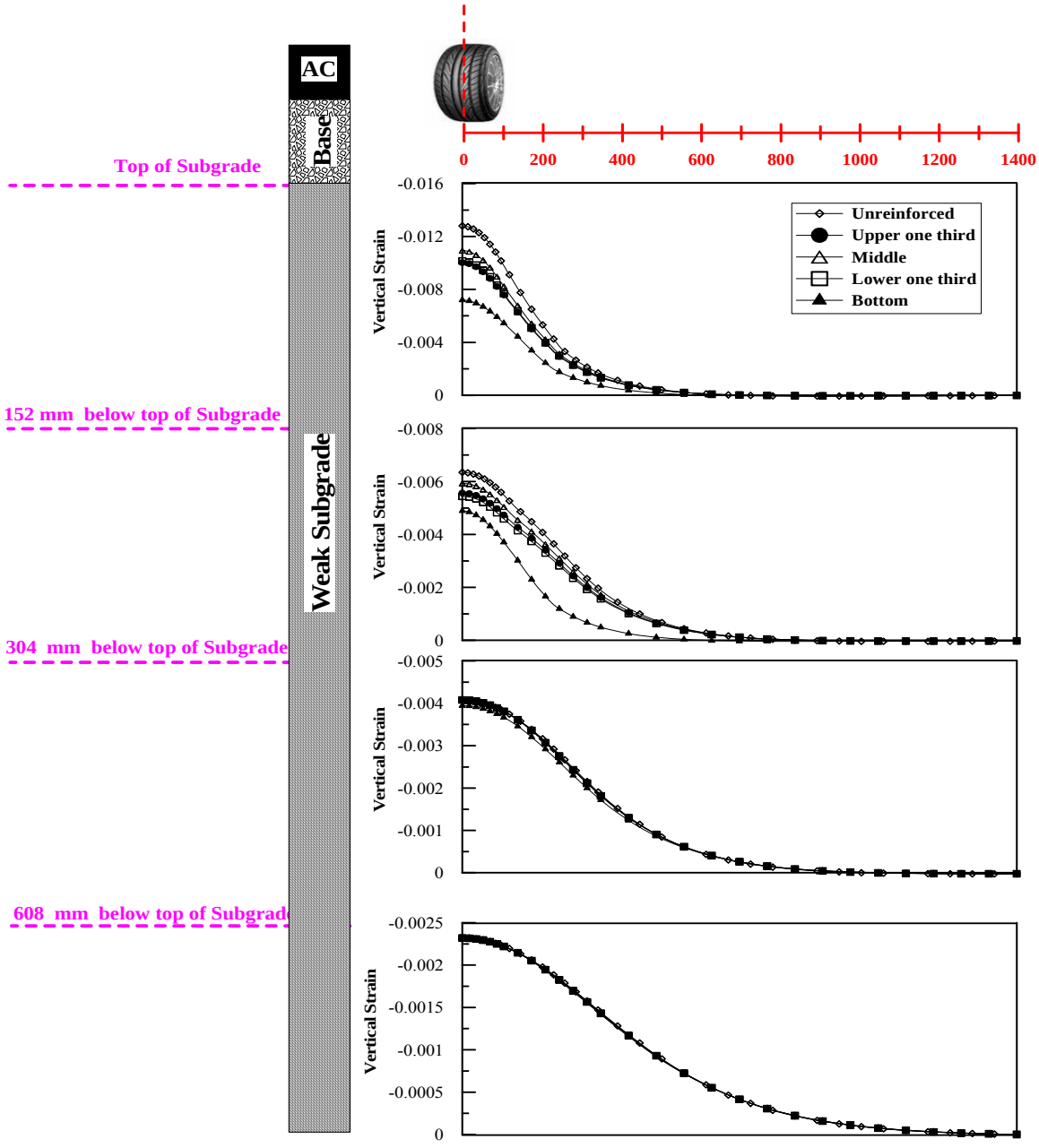

Figure 59
Vertical strain profiles within subgrade layer for unreinforced section 1a and reinforced with a layer of geogrid Type IV placed at different locations

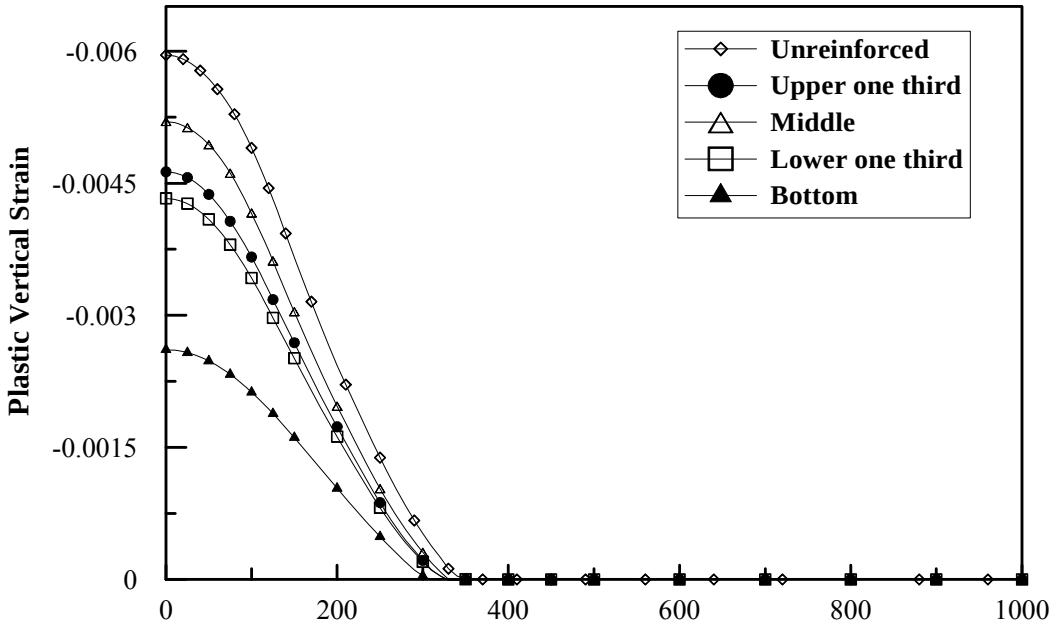

Figure 60
Vertical plastic strain profile at top of subgrade layer for unreinforced section 1a and reinforced with a layer of geogrid Type IV placed at different locations

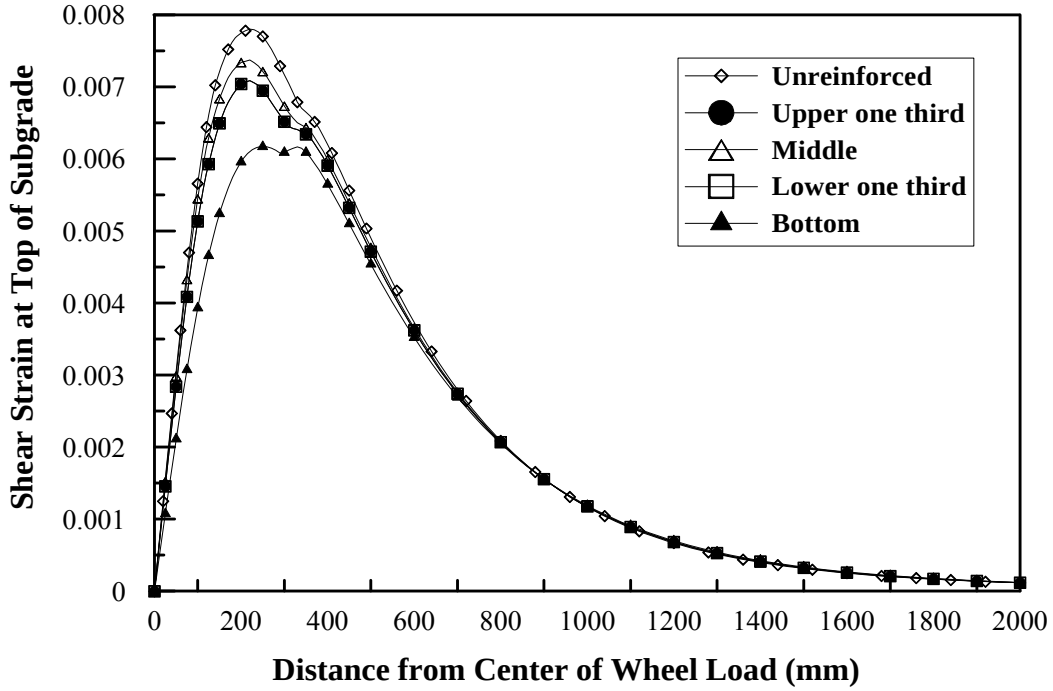

Figure 61
Shear strain profile at top of subgrade layer for unreinforced section 1a and reinforced with a layer of geogrid Type IV placed at different locations

Permanent Deformation

Less shear strain, coupled with less vertical and lateral strains results in a less severe state of loading leading to lower permanent deformation accumulation. Figure 62 depicts an example of the permanent deformation curves computed for unreinforced and geogrid reinforced sections using crushed limestone I. The permanent deformation curves obtained for unreinforced and geogrid reinforced section 2b using crushed limestone II are shown in Figure 63. It can be clearly seen that the geogrid reinforcement reduced the permanent deformation for the different reinforced sections. However, the magnitude of reduction depended on the geogrid stiffness, subgrade strength, and base course thickness.

Evaluation of the Geogrid Reinforced Sections Using a Mechanistic Empirical Approach

The improvement of the inclusion of the geogrid layer within the base course layer was also evaluated using the mechanistic empirical approach. In this approach, the response parameters computed from the finite element analysis results are used to determine the pavement structure distresses based on empirical models. Two types of distresses were considered to control the flexible pavement performance, namely, permanent deformation (rutting) and fatigue cracking. The permanent deformation of pavement structures was determined by first dividing each pavement layer into sub-layers. Damage models are then used to relate the vertical compressive strain, computed from the finite element analysis, at the mid-depth of each sub-layer and the number of traffic applications to layer plastic strains. The overall permanent deformation is then computed using equation (7) as a sum of permanent deformation for each individual sub-layer.

$$PD = \sum_{i}^{NS} \varepsilon^{i}_{p} \cdot h^{i} \qquad (7)$$

where, PD = pavement permanent deformation, NS = number of sub-layers, ε^{i}_{p} = total plastic strain in sub-layer I, and h^{i} = Thickness of sublayer i.

Three main damage models were used in this study, namely, one for the asphalt concrete material [equation (8)], one for the base [equation (10)], and one for subgrade materials [equation (11)]. The parameters of these models were determined through national calibration efforts using the Long-Term Pavement Performance (LTPP) database and laboratory tests conducted on the different pavement materials used.

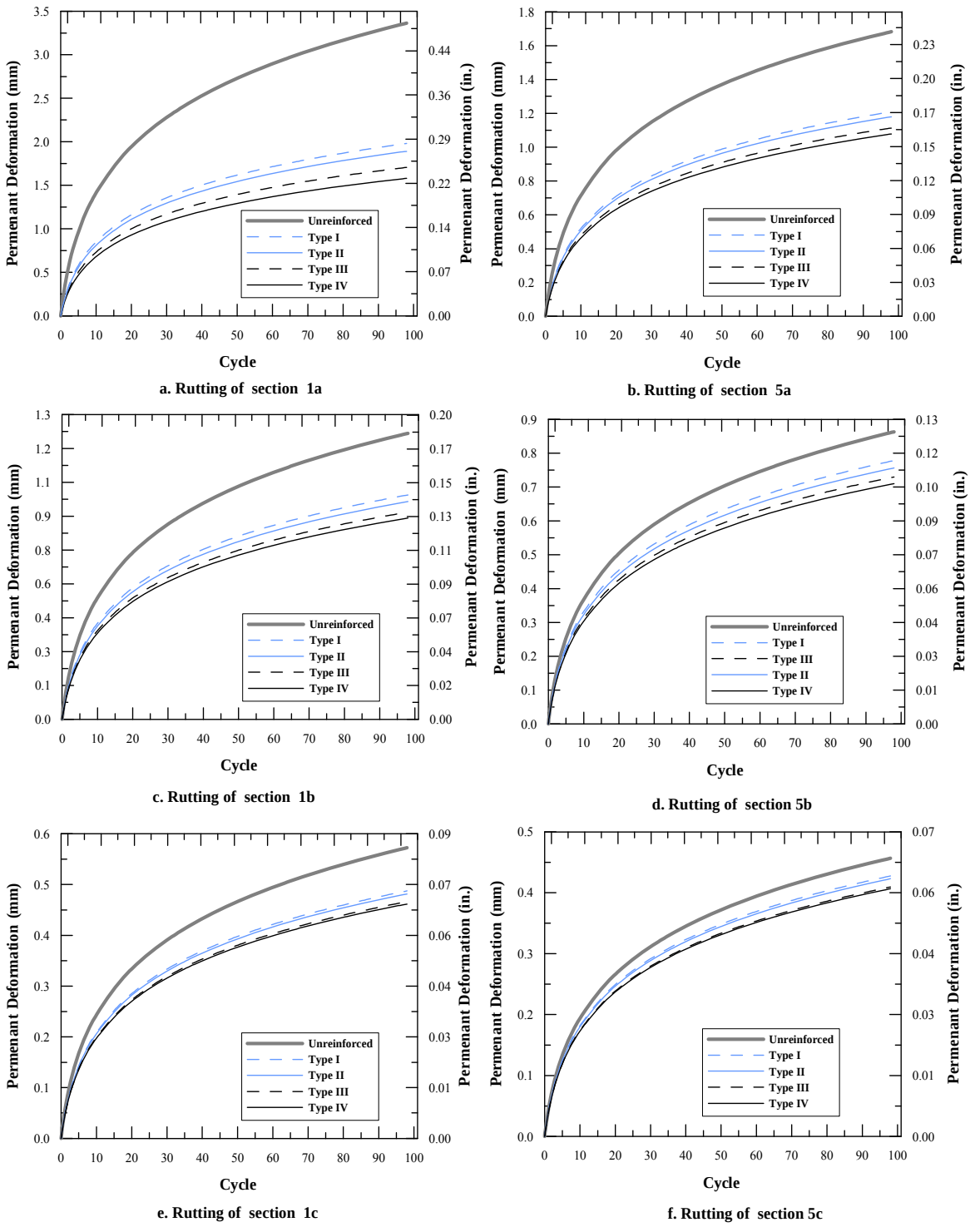

Figure 62
Rutting curves of different pavement sections for crushed limestone I

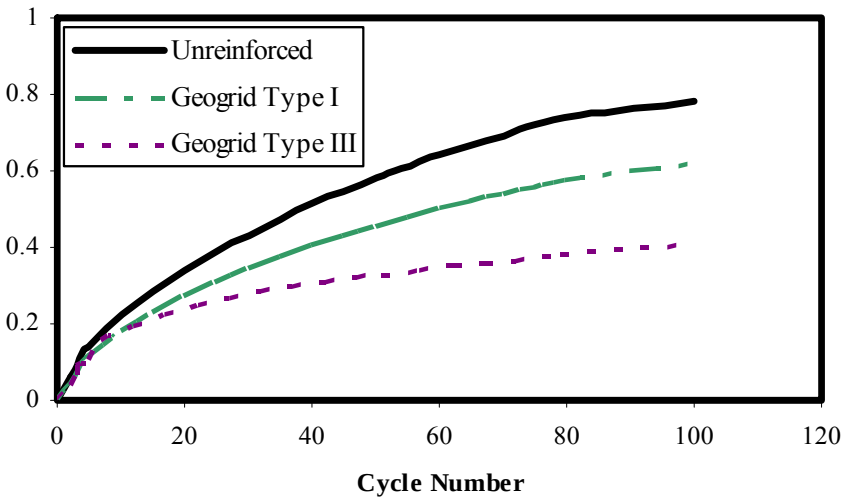

Figure 63
Rutting curves of section 2b of crushed limestone II

$$\frac{\varepsilon_p}{\varepsilon_v} = k_1 10^{-3.4488} T^{1.5606} N^{0.473844} \qquad \text{(Asphalt concrete layer)} \qquad (8)$$

where, ε_p = accumulated plastic strain at N repetitions of load, ε_v = vertical strain of the asphalt material, N = number of load repetitions, T = pavement temperature, and k_1 = function of total asphalt layer(s) thickness and depth to computational point, to correct for the variable confining pressures that occur at different depths and is expressed as:

$$k_1 = (C_1 + C_2 * \text{depth}) * 0.328196^{\text{depth}} \qquad (9)$$

where, $C_1 = -0.1039 * h_{ac}^2 + 2.4868 * h_{ac} - 17.342$, $C_2 = 0.0172 * h_{ac}^2 - 1.7331 * h_{ac} - 27.428$, and h_{ac} = is the asphalt layer thickness.

$$\frac{\varepsilon_p}{\varepsilon_v} = \beta_{GB}\left(\frac{\varepsilon_o}{\varepsilon_r}\right) \cdot e^{-\left(\frac{\rho}{N}\right)^{\beta}} \qquad \text{(Base course layer)} \qquad (10)$$

$$\frac{\varepsilon_p}{\varepsilon_v} = \beta_{SG}\left(\frac{\varepsilon_o}{\varepsilon_r}\right) \cdot e^{-\left(\frac{\rho}{N}\right)^{\beta}} \qquad \text{(Subgrade layer)} \qquad (11)$$

where, β_{GB} = is national model calibration factor for unbound base course material and is equal to 1.673; β_{SG} = is national model calibration factor for subgrade material and is equal to 1.35; ε_0, β, and ρ = material parameters; and ε_r = resilient strain imposed in laboratory test to obtain material properties.

The other major distress type occurring in flexible pavement that will be evaluated in this section is load associated fatigue cracking. Several model forms are available in the literature to characterize the fatigue damage in asphalt layers. The most commonly used model form to predict the number of load repetitions to fatigue cracking is a function of the tensile strain and mix stiffness (modulus). The model used in this study for the prediction of the number of repetitions to fatigue cracking was the national field calibrated model adopted in the MEPDG that was determined by numerical optimization and other modes of comparison and is expressed as follows:

$$N_f = 0.00432 \cdot k_1 \cdot \mathrm{C}\left(\frac{1}{\varepsilon_t}\right)^{3.9492}\left(\frac{1}{\mathrm{E}}\right)^{1.283} \quad (12)$$

where, N_f= traffic repetitions to AC fatigue, ε_t = resilient horizontal tensile strain from the response model taken as the maximum tensile value with the AC layer, C= a laboratory to field adjustment factor, E= AC complex modulus used in response model (psi), and k_1 = a correction factor to adjust for AC layer thickness (h_{ac}) effects and can be expressed in the following form:

$$k_1 = \frac{1}{0.000398 + \frac{0.003602}{1 + e^{(11.02 - 3.49 \cdot h_{ac})}}} \quad (13)$$

Effect of Different Parameters on Permanent Deformation

The effect of geogrid stiffness, subgrade strength, and base thickness on the performance of sections reinforced with a geogrid layer placed at the bottom of the base course layer evaluated using the mechanistic empirical approach those previously described. Nine sections (sections 1a-c, 3a-c, and 5a-c in) combining the bracketing combination of three base course thicknesses, three subgrade stiffness, and five geogrid types, namely, geogrid Types I, II, III, IV, and V were used in this evaluation. Figure 64 and Figure 64 present the traffic benefit ratio (TBR) values obtained for the different sections of crushed limestone I, while Figure 66 and Figure 66 present the TBR values obtained for the different sections of crushed limestone II. The TBR corresponds to the ratio of the number of load cycles to achieve a rut depth of 25 mm in a reinforced section to that of an unreinforced section. The N_R/N_U values obtained for the different sections are presented in Figure 68 and Figure 69 for crushed limestone I and in Figure 70 and Figure 71 for crushed limestone II. Here, N_R/N_U corresponds to the ratio of the traffic repetitions to reach AC fatigue for a reinforced section to that of unreinforced section.

In general, the results showed that for a given geogrid location, the reduction in permanent deformation depends on three factors: geogrid stiffness, subgrade strength, and base course thickness. Pavement sections on weak subgrades with medium to thin base layer thickness demonstrate appreciable reduction on rutting due to geogrid reinforcement with the thin base layer thickness showing the greater values of improvement. However, negligible to modest reinforcement effects on rutting was obtained for sections having firm subgrades or thick base layer thickness. These results are consistent with observations reported in previous studies. They are also consistent with conventional wisdom that geogrid reinforcement has less benefits for sections having a firm subgrade or thick base layer. The results also showed that the increase of the geogrid stiffness resulted in greater reduction in the permanent deformation of a reinforced section, hence increasing the number of load repetitions needed to reach the maximum allowable rutting value of 25 mm. The reason for this is that the higher geogrid stiffness, the lower the deformation and strain needed to mobilize the geogrid strength.

The results also demonstrated that geogrid reinforcement had a modest to high improvement on fatigue life, which is a great promise of reinforcement for controlling fatigue cracking. However, these results have not been validated in test sections due to the fact that most test sections reported in the literature have failed by rutting. It is noted that the increase in geogrid stiffness influenced the improvement in the fatigue life of section-1a only, which is the pavement section with a thin base layer built on top of weak subgrade soil. Furthermore, the increase in base course thickness had a much less adverse effect on the fatigue life improvement, especially for the moderate and stiff subgrades. However, some differences in the geogrid benefits were observed between sections built on top of weak subgrade to those built on top of moderate and stiff subgrades.

The mechanistic empirical approach was also used to evaluate the performance of sections 1a and 5c reinforced with geogrid Type IV placed at the middle, upper one-third, and lower one-third locations. Figure 72 and Figure 73 present the TBR and N_R/N_U values obtained for these sections, respectively. The results show that in terms of rutting the maximum benefit is seen when the geogrid reinforcement is at the bottom of the base for the section with thin base course thickness and weak subgrade soil, while placing the geogrid within the base course layer had a better performance when the base layer had the greatest contribution to the total permanent deformation of the pavement structure as in section 5c. For fatigue, elevating the reinforcement provides more benefits.

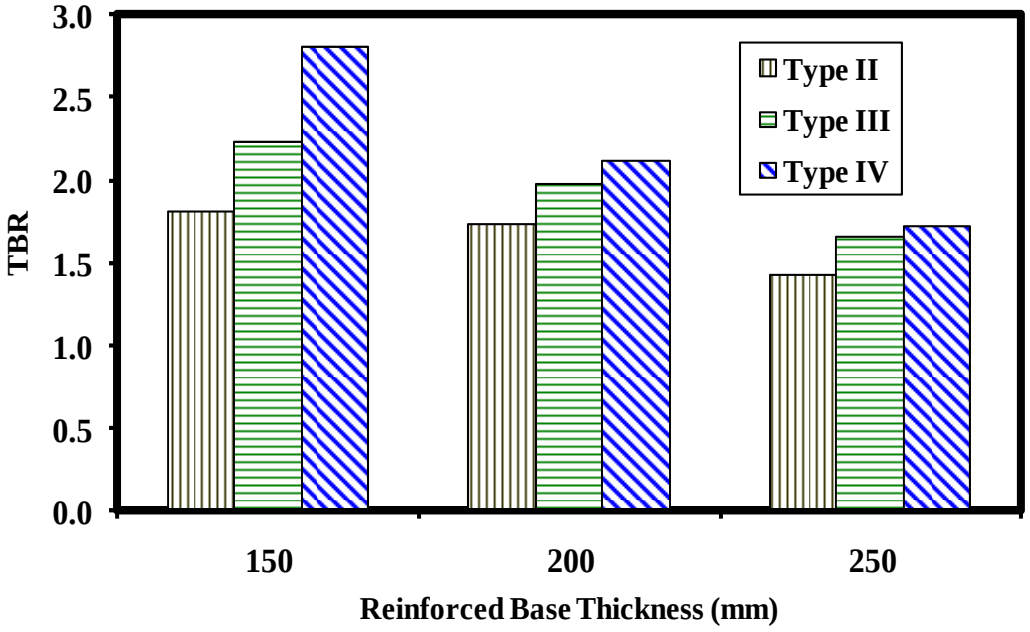

Figure 64
TBR of reinforced section with weak subgrade for crushed limestone I

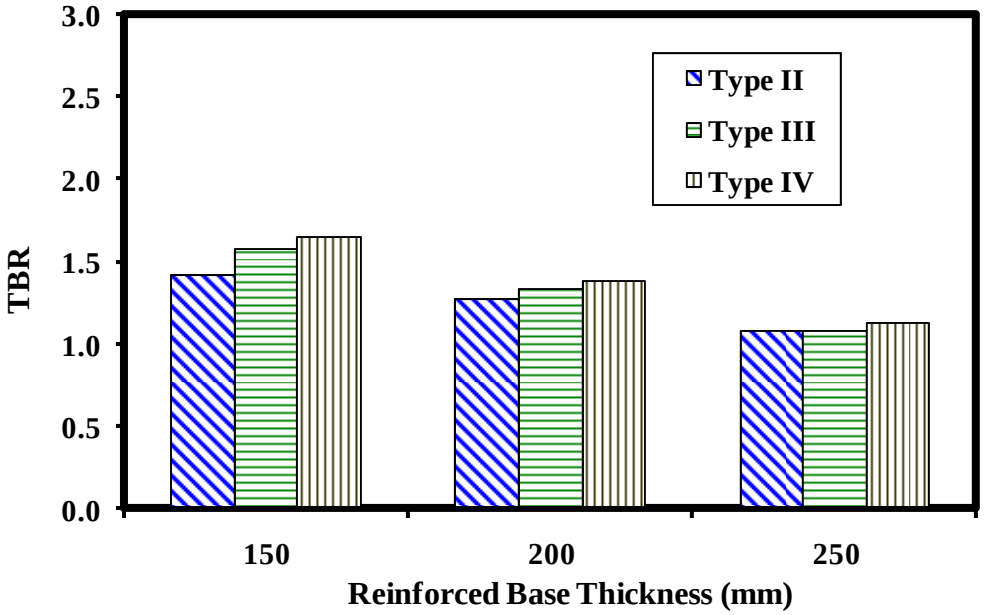

Figure 65
TBR of reinforced section with stiff subgrade for crushed limestone I

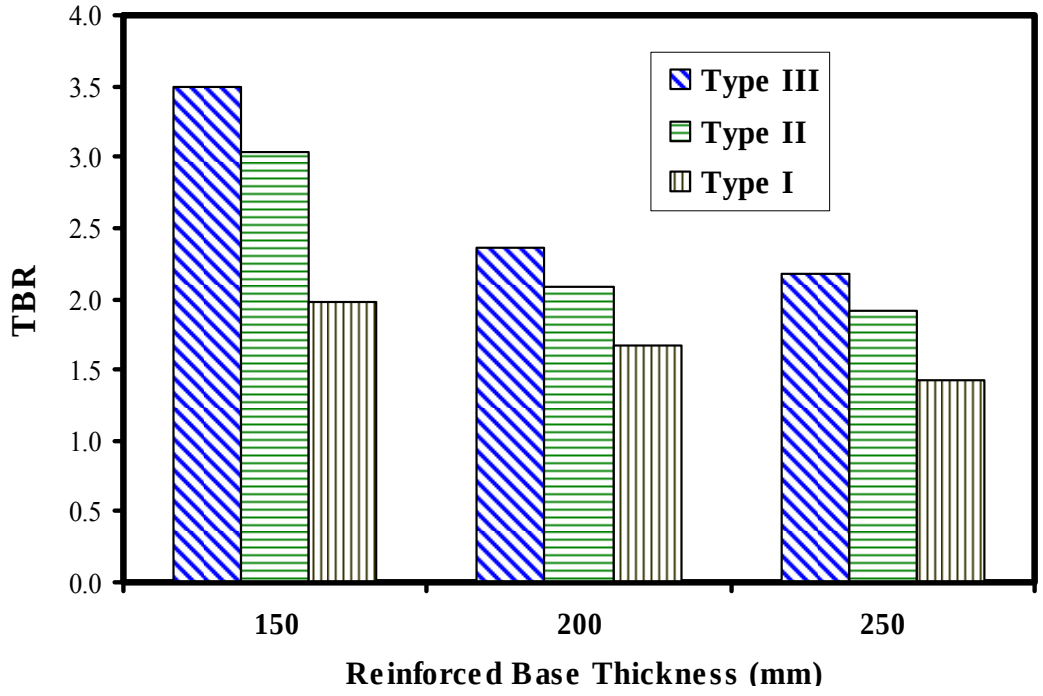

Figure 66
TBR of reinforced section with weak subgrade for crushed limestone II

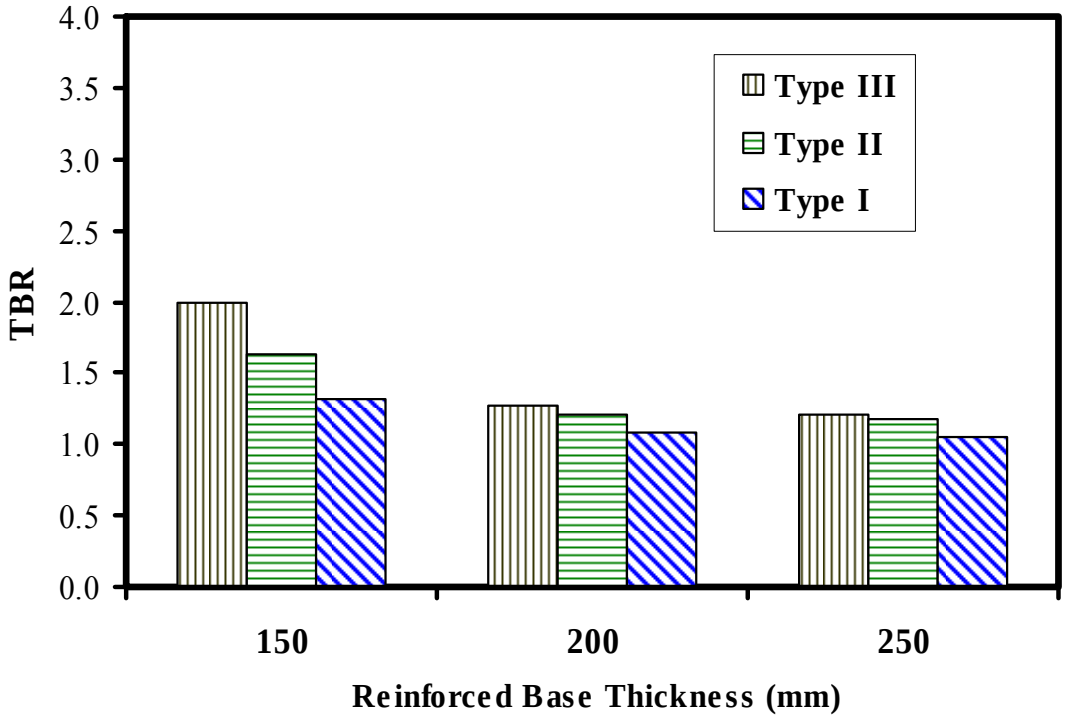

Figure 67
TBR of reinforced section with stiff subgrade for crushed limestone II

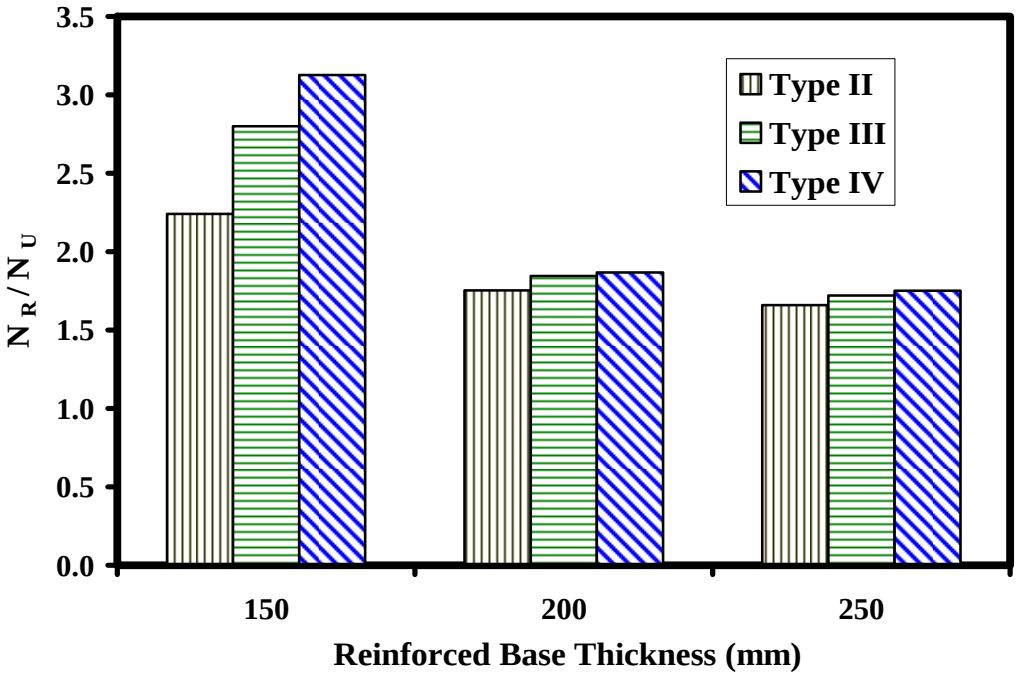

Figure 68
N_R / N_U of reinforced section with weak subgrade for crushed limestone I

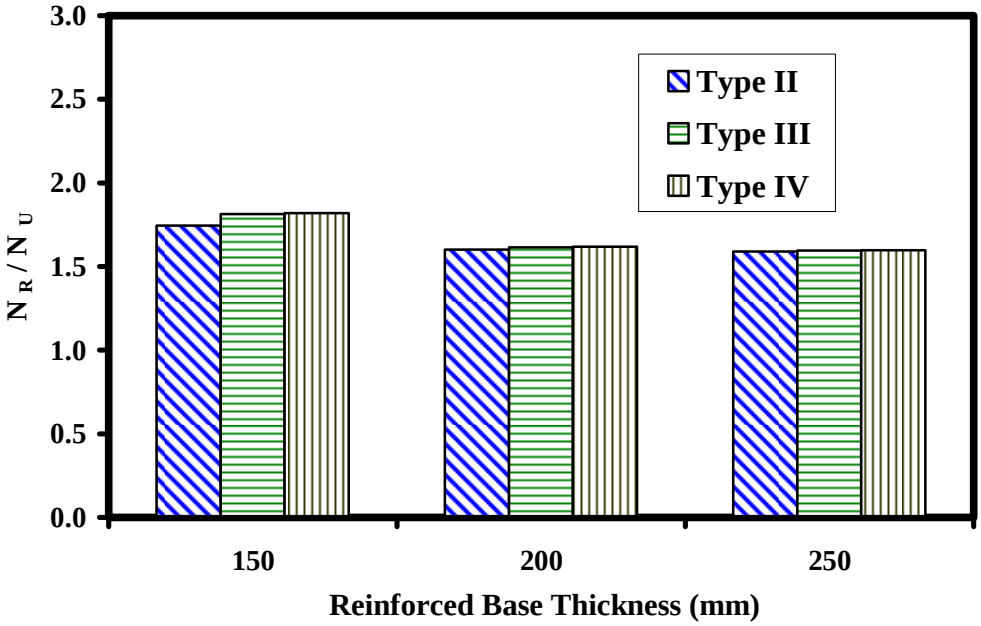

Figure 69
N_R / N_U of reinforced section with stiff subgrade for crushed limestone I

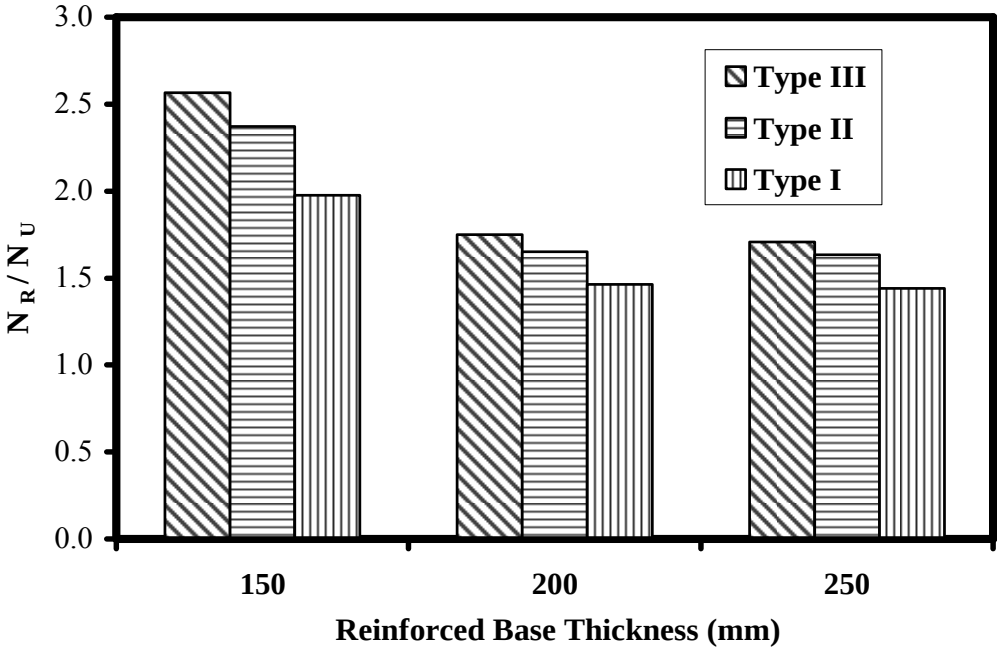

Figure 70
N_R / N_U of reinforced section with weak subgrade for crushed limestone II

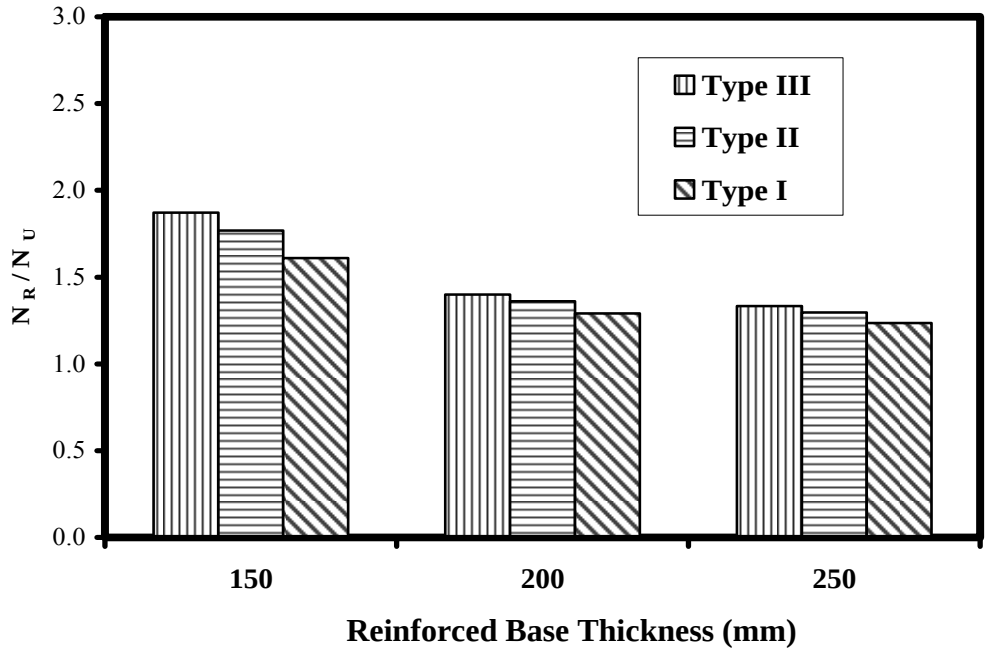

Figure 71
N_R / N_U of reinforced section with stiff subgrade for crushed limestone II

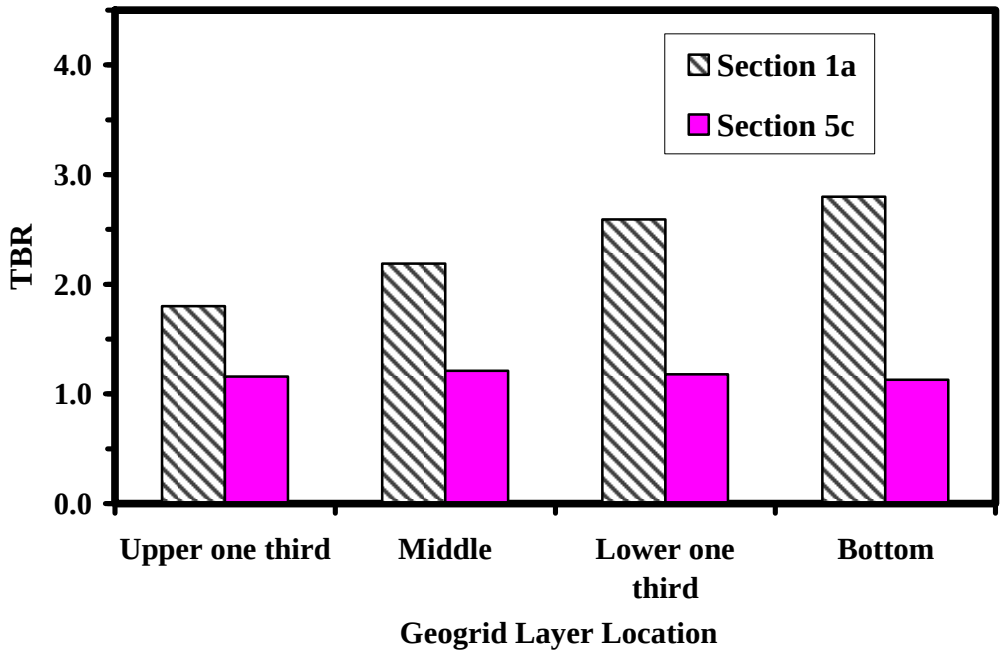

Figure 72
TBR of sections reinforced with geogrid layer placed at different locations

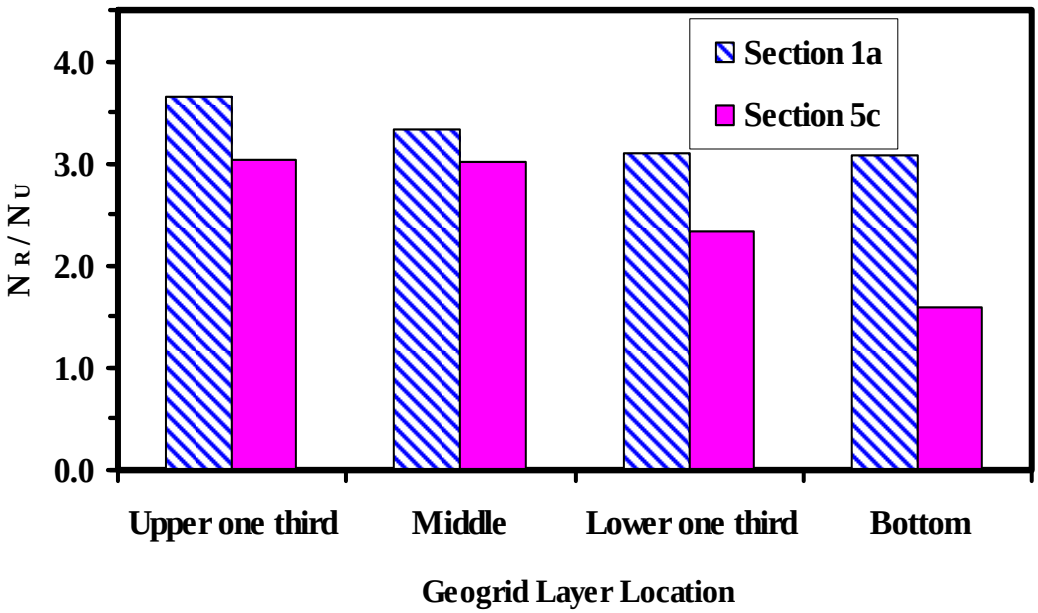

Figure 73
N_R / N_U of sections reinforced with geogrid layer placed at different locations

Development of TBR Model

A multiple regression analysis was conducted on the results of the finite element analysis to develop a prediction model of the TBR. Initially, a general model that includes all of the investigated variables and their interactions was selected (Equation 14). A stepwise variable selection procedure was conducted on the selected model to eliminate any insignificant variable. Based on the results of this procedure, only the normalized geogrid modulus, the interaction between the reinforced thickness and normalized geogrid modulus, the interaction between the subgrade strength and normalized geogrid modulus were found significant. The general TBR model is given as:

$$TBR = \beta_0 + \beta_1 X_1 + \beta_2 X_2 + \beta_3 X_3 + \beta_4 X_1 X_2 + \beta_5 X_1 X_3 + \beta_6 X_2 X_3 \quad (14)$$

where, X_1= the reinforced base layer thickness in mm; X_2= the geogrid modulus (kPa) used in the finite element models normalized to a modulus value of 135000 (kPa) for crushed limestone I and 428000 (kPa) for crushed limestone II; X_3 = subgrade CBR value; X_1X_2= the interaction between the effect of the reinforced thickness and normalized geogrid modulus; $X_1 X_3$= the interaction between the effect of the reinforced thickness and subgrade CBR value; and X_2X_3= the interaction between the normalized geogrid modulus and effect of the subgrade CBR value.

Based on the results of stepwise selection analysis, multiple regression analysis was conducted on finite element data to develop a TBR prediction model. Equation (15) and equation (16) present the TBR regression model obtained for crushed limestone I and crushed limestone II, respectively:

$$TBR_I = 1.0 + 1.08.X_2 - 0.00274.X_1.X_2 - 0.0239.X_2.X_3 \quad (15)$$

$$TBR_{II} = 1.0 + 1.3.X_2 - 0.00343.X_1.X_2 - 0.0305.X_2.X_3 \quad (16)$$

The TBR_I and TBR_{II} models had high R^2 of 0.94 and 0.95 and a low root mean squared error (RMSE) value of 0.098 and 0.172, respectively. This suggests that the models fits the data well. This is also illustrated in Figure 74 and Figure 75 which compare the TBR obtained using the finite element analysis and those predicted using the regression models. It can be observed that a good agreement was obtained between the predicted and measured values. Moreover, the model was able to provide good prediction of the TBR data that were not used in the development of the model.

Equations (15) and (16) suggest that the predicted TBR decreases with increasing the geogrid stiffness and decreasing the base layer thickness and the subgrade stiffness

strength. Furthermore, it is noted that the effect of the geogrid stiffness decreases with the increase in the base course layer thickness and the subgrade stiffness/strength.

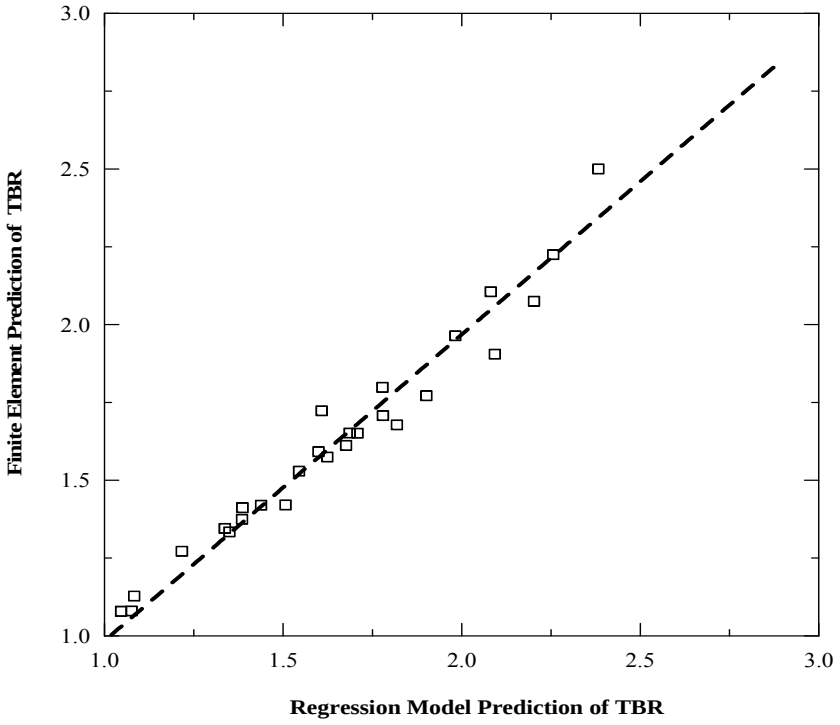

Figure 74
Prediction of TBR model

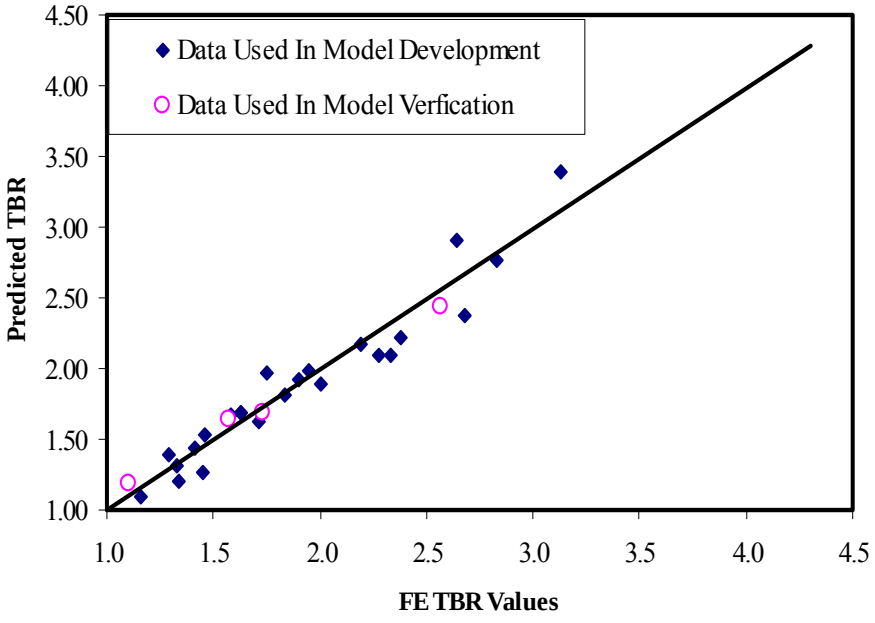

Figure 75
Prediction of TBR model

CONCLUSIONS

This report documents the findings of an extensive research study that was conducted to characterize the behavior of geogrid reinforced bases in flexible pavements. The objectives of this study were achieved through conducting an experimental testing and numerical modeling programs. The following sections summarize the findings and conclusions of each of these programs.

Experiential Testing Program

The experimental testing program in this study included performing different laboratory tests to characterize the performance of unreinforced and geogrid reinforced base course materials. Two base course materials were used in the laboratory tests: Kentucky limestone (crushed limestone I) taken from Martin Marietta quarry and Mexican limestone (crushed limestone II) taken from Vulcan quarry located near Baton Rouge. The properties of these base course materials are presented in Table 4. The test factorial included two types of base course materials and five types of geogrid reinforcements that are typically used in the construction of base course layers. The laboratory tests conducted in this study included drained compression triaxial test, resilient modulus repeated loading triaxial (RLT) test, and single-stage RLT tests. The drained compression triaxial test was used to evaluate the static strength properties and stress-strain response parameters of tested samples, while the different types of RLT were used to study the resilient and permanent deformations under conditions that simulate the physical conditions and stress states in base layers subjected to traffic loads. The effects of different factors associated with geogrid base course materials were investigated in this part of the study. Comprehensive statistical analyses were conducted on the data obtained from the different laboratory tests. Based on the results of the experimental testing program, the following conclusions can be drawn:

- The inclusion of geogrid reinforcement layer(s) improves the compressive strength and stiffness of base course materials under static loading. The geogrid improvement was not mobilized until certain strain levels were reached, which differed between the two crushed limestone materials investigated. For crushed limestone I, this strain limit was 1 percent; while for crushed limestone II it was 2 percent. This could be due to better interlocking between geogrid and crushed limestone I. Moreover, the geogrid improvement was more pronounced at higher strain levels.

- The improvement due to the geogrid in the compressive strength and stiffness response parameters under static loading were found to be a function of the geogrid location, geogrid type, and number of layers. At a certain geogrid location, stiffer geogrids exhibited greater benefits.

- For a specific geogrid stiffness/type, the highest improvement was always achieved when using two geogrid layers placed at the upper and lower third of the sample height. Whereas, the lowest improvement was encountered when placing the geogrid layer at the sample mid-height for crushed limestone I samples but varied for crushed limestone II material for the different response parameters.

- The inclusion of geogrid reinforcement layer(s) significantly reduces the accumulation of permanent deformation accumulation under cyclic loading of base course materials. The reduction in permanent deformation was minimal at early cycles of testing; however, the permanent deformation resistance increased significantly with the increase in load cycles.

- The reduction in permanent deformation was found to be a function of the geogrid stiffness, geogrid arrangement, and number of load cycles. However, the geogrid arrangement was found to be the dominant factor influencing this reduction.

- The dominant geogrid reinforcement mechanism that influences the reduction in permanent deformation is due to the geogrid—aggregates interlocking mechanism.

- The geogrid inclusion did not show an appreciable effect on the resilient deformation of reinforced samples.

Numerical Modeling Program

Finite element analyses were conducted to assess the benefits of using geogrids to reinforce the base course layer in a flexible pavement structure and to evaluate the effects of subgrade strength, thickness of the base course layer, and stiffness and location of the reinforcement layer on these benefits. Different constitutive models were used to describe the behavior of the pavement layers, which included Extended Drucker Prager, Modified Cam Clay, and Elastic–Perfectly Plastic models. In addition, a two-surface critical state elasto-plastic model proposed by Manzari and Daflias was implemented in the ABAQUS finite element software to describe the behavior of crushed limestone II *[62]*. The stresses, strains, and permanent deformation obtained from the results of finite element analysis were used to evaluate the effect of the different variables associated with geogrid

reinforced base layers. The improvement due to the geogrid reinforcement was also assessed using a mechanistic empirical approach. Two types of distresses were considered to control the flexible pavement performance, namely, permanent deformation (rutting), and fatigue cracking. Multiple regression analyses were conducted on the results of the finite element analyses to develop models that predict geogrid benefits as a function of the different variables investigated in this study. Based on the results of this numerical modeling program, the following conclusions can be drawn:

- The geogrid reinforcement reduced the lateral strains within the base course and subgrade layers. The maximum reduction in lateral strain was observed at the base subgrade interface. The geogrid effect was mainly below the wheel loading area, and it almost vanished at a distance of 304 mm from the center of the wheel load.

- The inclusion of the geogrid layer resulted in a significant reduction in the vertical strains at the top of subgrade. The geogrid influence on the vertical strain was experienced within a zone that extends to a depth of about 304 mm below the top of the subgrade layer. However, the greatest influence was encountered at the top of the subgrade.

- The improvement of geogrid layer was found to be more pronounced in reducing the plastic (permanent) strains than in reducing the resilient strains of pavement section, which help reduce the accumulated surface rutting.

- The geogrid layer resulted in decreasing the shear strains at the top of the subgrade layer and provided a better distribution of these strains.

- The geogrid benefits in improving the developed strains were more appreciable in sections with weak subgrades compared to those in sections with stiff subgrades. In addition, these benefits were reduced as the thickness of the base layer increased and were enhanced as the stiffness of the geogrid layer increased.

- More reduction in the lateral strain at AC-base course layer interface was achieved when placing the geogrid layer at the upper one-third location compared to the other locations. However, the bottom location was the most efficient in reducing the total and plastic vertical strain at the top of the subgrade layer.

- The geogrid reinforcement demonstrated appreciable reduction in the permanent deformation for pavement sections built on top of weak subgrade soils with medium to thin base layer thickness with the thin base layer thickness showing greater values

of improvement. However, negligible to modest reinforcement effects on rutting was obtained for sections having a firm subgrade or thick base layer thickness.

- The increase in the geogrid stiffness resulted in significant reduction of permanent deformation. However, the geogrid stiffness effect decreased with the increase in the thickness of the reinforced base course layer.

- In terms of rutting, the maximum benefit is attained when the geogrid reinforcement is placed at the bottom of the base for the section with thin base course thickness and weak to moderate subgrade soil, while placing the geogrid within the base course layer had a better performance when the base layer had the greatest contribution to the total permanent deformation of the pavement structure.

- The geogrid reinforcement had modest to high values of improvement in fatigue life of pavement structure, which shows great promise of reinforcement for controlling AC fatigue cracking. The closer the geogrid layer to the AC-base interface, the better the improvement in the fatigue life of reinforced pavement structures.

- The increase in geogrid stiffness only improved the fatigue life of pavement sections with thin base layers built on top of weak subgrade soil, while the increase in base course thickness had a much less adverse effect on the fatigue life improvement, especially for the moderate and stiff subgrade.

RECOMMENDATIONS

The results of extensive laboratory testing and finite element analyses on geogrid-reinforced base aggregate materials demonstrated the potential benefit of reinforcing the base aggregate layer for flexible pavements built on soft subgrades. Based on the results of this study, we have the following recommendations:

- The researchers recommend that LADOTD pavement design engineers start considering the reinforcement of base aggregate layers with geogrids for flexible pavements built on soft subgrades with resilient modulus $M_r < 2000$ psi (or CBR value < 1.5), especially in cases where it is difficult to stabilize/treat the soft subgrade soil with cement or lime and to create working platforms for constructing pavements and embankments on soft soils.

- The selection of geogrid elastic modulus in flexible pavement design should be based on traffic volume, thickness of base course layer, and subgrade resilient modulus. In any case, the researchers recommend the use of geogrids with elastic tensile modulus at 2 percent strain, $E_{2\%} \geq 250$ lb/ft.

- The researchers recommend placing the geogrid layer at the base-subgrade interface for pavements with a base thickness of less than 18 in. and at the middle of the base aggregate layer for base thicknesses equal or greater than 18 in.

- If the geogrid reinforcement is used to create a working platform for constructing on soft subgrade, one geogrid layer should be placed on top of soft subgrade immediately above the non-woven geotextile. Another geogrid layer is recommended to be placed at upper one third thickness of the base course layer.

- Additional research effort is needed to characterize the effect of geogrid-aggregate interlocking on the performance of the geogrid-reinforced base layer in flexible pavement structures and the extent of the influenced zone adjacent to the geogrid layer.

- It is also recommended that the benefits of geogrid-reinforcement of the base aggregate layer on the asphalt concrete fatigue life be verified and validated through conducting accelerated experimental tests and/or evaluating the performance of field test sections.

ACRONYMNS, ABBREVIATIONS, AND SYMBOLS

2D	Two-dimensional
A_0	Dilatancy parameter
AASHTO	American Association of State Highway and Transportation Officials
ABAQUS	A program for finite elements
AC	Asphalt Concrete
ALF	Louisiana Accelerated Loading Facility
ANOVA	Statistical analysis of variance
BCR	Base course reduction
C	A laboratory to field adjustment factor
CBR	California bearing ratio
C_m	A model parameter
CMD	Cross-machine direction
CRD	Completely random design
d	Cohesion of the material
E	AC complex modulus used in response model (psi)
$E_{s1\%}$	Secant elastic moduli at one percent strain level
$E_{s2\%}$	Secant elastic moduli at two percent strain level
ESAL	Equivalent single axle load
F_{max} and C_f	Fabric tensor parameters
G_s	Specific gravity
h_{ac}	Asphalt layer thickness
h^i	Thickness of sublayer i
IM-$E_{s1\%}$, IM-$E_{s2\%}$, IM-USS, and IM-RSS	Improvement factors
K_0	Bulk modulus
k_1	Function of total asphalt layer(s) thickness and depth to computational point
k_1	A correction factor to adjust for AC layer thickness (h_{ac}) effects
k_1, k_2, and k_3	material properties
k^b_c, k^b_e, k^d_c, and k^d_e	bounding and dilatancy (phase transformation) surface parameters
K	Ratio of the yield stress in triaxial tension to the yield stress in triaxial compression, controls the dependence of the yield surface on the value of the intermediate principal stress

LADOTD	Louisiana Department of Transportation and Development
LSM	Least Square Means
LTPP	Long-term pavement performance
LVDT	Linearly variable differential transducers
M	Initial yield surface parameter
m	Size of the yield surface, describes the isotropic evolution of the yield surface
M_c, M_e, λ, $e_{c,ref}$, and p_{ref}	Parameters defining the critical state of a soil
MEPDG	Mechanistic Empirical Pavement Design Guide
M_r	Resilient modulus
p_a	Atmospheric pressure (101.3 kPa)
MTS	Material testing system
MX	Machine direction
N	Number of load repetitions
NCHRP	National Cooperative Highway Research Program
N_f	Traffic repetitions to AC fatigue
N_R/N_U	Ratio of the traffic repetitions to reach AC fatigue for a reinforced section to that of unreinforced section.
NS	Number of sub-layers
OMC	Optimum moisture content obtained in Standard Proctor Test
p	Mean effective stress
PD	Pavement permanent deformation
q_m	Mises equivalent stress
r	third invariant of deviatoric stress
RLT	Repeated loading triaxial
RMSE	Root mean square error
RPS	Reduction in the vertical permanent strain
RSS	Residual shear strength
s	Deviatoric stress tensor
STC	Static triaxial compression
T	Pavement temperature
TBR	Traffic benefit ratio
USS	Ultimate shear strength
ν	Poisson's ratio
X_1	Reinforced base layer thickness in mm

X_2	Geogrid modulus (kPa) used in the finite element models normalized to a modulus value of 135000 (kPa) for crushed limestone I and 428000 (kPa) for crushed limestone II
X_3	Subgrade CBR value
X_1X_2	Interaction between the effect of the reinforced thickness and normalized geogrid modulus
$X_1 X_3$	Interaction between the effect of the reinforced thickness and subgrade CBR value
X_2X_3	Interaction between the normalized geogrid modulus and effect of the subgrade CBR value
Y_{ijk}	Dependent variable
α	Deviatoric back-stress ratio tensor, describes the kinematic hardening of the yield surface, which indicates the location of the center of the yield surface
β	Slope of the linear yield surface in the p-t stress plane, commonly referred to as the friction angle of the material
β_{GB}	National model calibration factor for unbound base course material, equal to 1.673
β_{SG}	National model calibration factor for subgrade material, equal to 1.35
γ_{max}	Maximum unit weight obtained in Standard Proctor Test
ε_0, β, and ρ	Material parameters
ϵ_{ijk}	Random sampling variation for observation k, at any location case and stiffness level ij
ϵ_{ijkl}	Random sampling variation
ε^i_p	Total plastic strain in sub-layer I
ε_p	Accumulated plastic strain at N repetitions of load
ε_r	Recoverable elastic strain
ε_r	Resilient strain imposed in laboratory test to obtain material properties
ε_t	Resilient horizontal tensile strain from the response model taken as the maximum tensile value with the AC layer
ε_v	Vertical strain of the asphalt material
μ	Overall mean
$\sigma 1$, $\sigma 2$, $\sigma 3$	Principal stress components
σ_{cyc}	Maximum cyclic stress
τ_{1i}	Effect of geogrid arrangement

$\tau_1\tau_{2ij}$	Effect of the interaction between the geogrid arrangement and type
$\tau_1\tau_{3ik}$	Effect of the interaction between the geogrid arrangement and number of load cycles
$\tau_1\tau_2\tau_{3ijk}$	Effect of the interaction between the geogrid arrangement, geogrid stiffness, and the number of load cycles
τ_{2j}	Effect of geogrid type/stiffness
$\tau_2\tau_{3ik}$	Effect of the interaction between the type/stiffness and number of load cycles τ_{3k} is the effect of number of load cycles
τ_{oct}	Octahedral shear stress
ϕ`	Friction angle

REFERENCES

1. NCHRP (2004). *Guide for Mechanistic-Empirical Design of New and Rehabilitated Pavement Structures.* NCHRP Final Report for NCHRP 1-37A Project. www.NCHRP 1-37A Designguide.com. Accessed July 20, 2005.
2. Berg, R. R.; Christopher, B.R.; and Perkins, S.W. (2000). "Geosynthetic reinforcement of the aggregate base course of flexible pavement structures." GMA White paper II, Geosynthetic Material Association, Roseville, MN, USA, 130 p.
3. Perkins, S.W., and Ismeik, M. (1997). "A Synthesis and Evaluation of Geosynthetic Reinforced Base Layers in Flexible Pavements: Part I," *Geosynthetics International*, Vol. 4, No. 6, pp. 549-605.
4. Ashby, M., and Jones, D. Engineering Materials 1, Pergamon Press, 1980.
5. Arnold, G. K., (2004). *Rutting of Granular Pavements,* Ph.D. dissertation, School of Civil Engineering, The University of Nottingham, The United Kingdom.
6. Mohammad, L.N.; Herath, A.; Rasoulian, M.; and Zhongjie, Z. (2006). "Laboratory Evaluation of Untreated and Treated Pavement Base Materials from a Repeated Load Permanent Deformation Test." *Transportation Research Record*, Vol. 1967, pp. 78-88.
7. Khogali, W. E., and Mohamed, E. H. (2004). "Novel Approach for Characterization of Unbound Materials." Transportation Research Record, Vol. 1874, pp. 38-46.
8. Puppala, A. J.; Chomtid, S.; and Bhadriraju V. (2005) "Evaluation of Plastic Strain Potentials in Subgrade Soils Using Repeated Load Triaxial Tests." *The 84th Transportation Research Board Annual Meeting. CD-ROM*, National Research Council, Washington, D.C.
9. Uzan, J. (1985). Characterisation of Granular Material. Transport Research Record No. 1022. Transportation Research Board, Washington D.C., USA. pp. 52-59.
10. Sweere, G.T.H. (1990). "Unbound Granular Bases for Roads," Ph.D. thesis, University of Delft, Delft, The Netherlands.
11. Brown, S.F., and Hyde, A.F.L. (1975). "Significance of Cyclic Confining Stress in Repeated-load Triaxial Testing of Granular Material." Transportation Research Record 537, Transportation Research Board, Washington, D.C., pp. 49-58.
12. Paute, J. L.; Hornych, P.; and Benaben, J.P. (1996). "Repeated Load Triaxial Testing of Granular Materials in the French Network of Laboratoires des Ponts et Chausse´es." Flexible Pavements, Proc., Eur. Symp. Euroflex 1993, A. G. Correia, ed., Balkema, Rotterdam, The Netherlands, pp. 53-64.
13. Lekarp, F., and Dawson, A. (1998). "Modelling Permanent Deformation Behavior of Unbound Granular Materials." Construction and Building Material.
14. Hicks, R.G. (1970). Factors Influencing the Resilient Properties of Granular Materials, Ph.D. thesis, University of California, Berkeley, CA.

15. Allen, J. J., and Thompson, M.R. (1974). “Resilient Response of Granular Materials Subjected to Time Dependent Lateral Stresses.” Transp. Res. Rec. 510, Transportation Research Board, Washington, D.C., pp. 1-13.

16. Lekarp, F. (1997). “Permanent Deformation Behaviour of Unbound Granular Materials,” Licentiate thesis, Royal Institute of Technology, Stockholm.

17. Haynes, J. G., and Yoder, E. J. (1963). “Effects of Repeated Loading on Gravel and Crushed Stone Base Course Materials Used in the AASHO Road Test.’’ Highway Research Record, Vol. 39.

18. Barksdale, R.D. (1972). “Laboratory Evaluation of Rutting in Basecourse Materials.” Proceedings of the 3rd International Conference on Structural Design of Asphalt Pavements, pp.161-174.

19. Thom, N.H., and Brown, S.F. (1987). “Effect of Moisture on the Structural Performance of a Crushed-limestone Road Base.’’ Transp. Res. Rec. 1121, Transportation Research Board, Washington, D.C., pp. 50-56.

20. Dawson, A.R.; Thom, N.H.; and Paute, J.L. (1996). “Mechanical Characteristics of Unbound Granular Materials as a Function of Condition.” Flexible Pavements, Proc., Eur. Symp. Euroflex 1993, A. G. Correia, ed., Balkema, Rotterdam, The Netherlands, pp. 35-44.

21. Heydinger A.G.; Xie, Q.L.; Randolph, B.W.; and Gupta, J.D. (1996). Analysis of Resilient Modulus of Dense and Open-graded Aggregates. Transportation Research Record 1547, Transportation Research Board, Washington, D.C., pp. 1-6.

22. Allen, J. (1973). “The Effect of Non-constant Lateral Pressures of the Resilient Response of Granular Materials,’’ Ph.D. thesis, University of Illinois at Urbana-Champaign, Urbana, IL.

23. Mayhew, H.C. (1983). Resilient Properties of Unbound Road Base Under Repeated Triaxial Loading. Lab. Rep. 1088, TRRL, Crowthorne, U.K.

24. Barksdale, R.D. (1991). *The aggregate handbook*. National Stone Association, Washington, D.C.

25. Trollope, E.H.; Lee, I.K.; and Morris, J. (1962). “Stresses and Deformation in Two-layer Pavement Structures under Slow Repeated Loading.” Proceedings, ARRB, Vol. 1, Part 2, pp. 693-718.

26. Robinson, R.G. (1974). “Measurement of the Elastic Properties of Granular Materials Using a Resonance Method.’’ TRRL Supplementary Rep. No. 111. UC, TRRL.

27. Kolisoja, P. (1998). “Large Scale Dynamic Triaxial Tests.” III. Delprosjektrapport 20, Arbeidsfelleskapet KPG, Oslo, Norway.

28. Niekerk, A.; Scheers, J.; Muraya, P.; and Kisimbi, A. (2000). The Effect of Compaction on the Mechanical Behaviour of Mix Granulate Basecourse Materials and on Pavement Performance. Unbound Aggregates in Roads-Proceedings of the International Symposium, UNBAR 5, Nottingham, UK, 21-23 June 2000, pp. 125-136.

29. Dunlap, W.A. (1966). “Deformation Characteristics of Granular Materials Subjected to Rapid Repetitive Loading,’’ Ph.D. thesis, Texas A&M University, College Station, TX.

30. Raad, L.; Minassian, G.; and Gartin, S. (1992). “Characterization of Saturated Granular Bases Under Repeated Loads.’’ Transportation Research Record, Vol. 1369, Transportation Research Board, Washington, D.C., pp. 73-82.

31. Plaistow, L.C. (1994). ‘‘Non-linear Behaviour of Some Pavement Unbound Aggregates,’’ MS thesis, Department of Civil Engineering, University of Nottingham, Nottingham, England.

32. Haas, R.; Walls, J.; and Carroll, R.G. (1988). “Geogrid Reinforcement of Granular Bases in Flexible Pavements,” *Transportation Research Record 1188*, pp. 19-27.

33. Moghaddas-Nejad, F., and Small, J.C. (1996). “Effects of Geogrid Reinforcement in Model Track Tests on Pavements,” *Journal of Transportation Engineering*, Vol. 122, No. 6, pp. 468-474.

34. Perkins, S.W.; Ismeik, M.; and Fogelsong, M.L. (1998). “Mechanical Response of Geosynthetic-Reinforced Pavement System to Cyclic Loading,” Proceedings of the Fifth International Conference on the Bearing Capacity of Roads and Airfields, Trondheim, Norway, Vol. 3, pp. 1503-1512.

35. Cancelli, A., and Montanelli, F. (1996). “In-ground Test for Geosynthetic Reinforced Flexible Paved Roads”, Proceedings of the Conference Geosynthetics ’99, Boston, MA, USA, Vol. 2, pp. 863-878.

36. Perkins, S.W. (1999). “Geosynthetic Reinforcement of Flexible Pavements: Laboratory Based Pavement Test Sections,” Federal Highway Administration Report FHWA/MT-99-001/8138, Montana Department of Transportation, 140 p.

37. Koerner, R.M. (1998). *Designing With Geosynthetics*, 4th Edition, Prentice-Hall Inc., Englewood Cliffs, NJ, 761 p.

38. Leng, J. and Gabr, M. (2003). “Characteristics of Geogrid-Reinforced Aggregate under Cyclic Load,” *Journal of Transportation Research Board,* No. 1786, National Research Council, Washington, D.C., pp. 29-35.

39. Rodriguez, A. R.; Castillo, H.D.; and Sowers, G.F. (1988). *Soil Mechanics in Highway Engineering*.

40. Binquet, J. A. and Lee, K. L. (1975). “Bearing Capacity Analysis on Reinforced Earth Slabs,” Journal of Geotechnical Engineering, ASCE, Vol. 101, pp. 1257-1276.

41. Barksdale, R.D.; Brown, S. F.; and Chan, F. (1989). “Potential Benefits of Geosynthetics in Flexible Pavement Systems,” *National Cooperative Highway research Program Report* No. 315, Transportation Research Board, National Research Council, Washington, D.C., 56 p.

42. Abu-Farsakh, M.Y.; Nazzal M.; and Mohammad, L., (2007). “Effect of Reinforcement on Resilient and Permanent Deformations of Base Course Material,” *Journal of the Transportation Research Board*, No. 2004, Soil Mechanics, pp. 120-131.

43. Nazzal, M.; Abu-Farsakh, M.Y.; and Mohammad L. (2007). "Laboratory Characterization of Reinforced Crushed Limestone under Monotonic and Cyclic Loading." *ASCE Journal of Materials in Civil Engineering,* Vol. 19, No. 9, pp. 772-783.
44. Gray, D.H. , and Al-Refeai, T. (1986). "Behavior of Fabric-Versus Fiber-Reinforced Sand." *Journal of Geotechnical Engineering*, Vol. 112, No. 8, pp. 804-820.
45. Ashmawy, A.K; Bourdeau, P.L.; Drnevich, V.P.; and Dysli, M., (1999) "Cyclic Response of Geotextile- Reinforced Soil," *Journal of Soils and Foundations*, Vol. 39, No. 1, February, pp. 43-52.
46. Moghaddas-Nejad, F., and Small, J.C. (2003). "Resilient and Permanent Characteristics of Reinforced Granular Materials by Repeated Load Triaxial Tests," *ASTM Geotechnical Testing Journal,* Vol. 26, No. 2, pp. 152-166.
47. Perkins, S.W.; Christopher, B.; Cuelho, E.L.; Eiksund, G.R.; Hoff, I.; Schwartz, C.W.; Svano, G.; and Want, A. (2004). "Development of Design Methods for Geosynthetic Reinforced Flexible Pavements." A report prepared for the U.S. Department of Transportation, Federal Highway Administration, FHWA/DTFH61-01-X-00068, 263 p.
48. Perkins, S.W. (2001) "Mechanistic-Empirical Modeling and Design Model Development of Geosynthetic Reinforced Flexible Pavements," Montana Department of Transportation, Helena, Montana, Report No. FHWA/MT-01- 002/99160-1A.
49. Dondi, G. (1994). "Three Dimensional Finite Element Analysis of a Reinforced Paved Road", Proc. Of the Fifth International Conference on Geotextiles, Geomembranes and Related Products, Singapore, pp. 95-100.
50. Abu-Farsakh, M.Y.; Nazzal, M.; and Mohammad, L.N., 2007 "Finite Element Analyses to Evaluate the Benefits of Geogrid Base Reinforcement in Flexible Pavement," *International Journal of Pavements*, Volume 6, Number 1-2-3, pp. 146-157.
51. Nazzal, M**.**D.; Abu-Farsakh, M.; and Mohammad, L. (2006) "Numerical Analyses of Geogrid Reinforced Flexible Pavements." *Proc., GeoCongress Conference*, Atlanta, GA.
52. *Tensar Geogrid Product Specifications* (2004). Tensar Earth Technologies, Atlanta, GA. *www.tensarcorp.com/uploadedFiles/SPECTRA_MPDS_BX_8.05.pdf*
53. AASHTO T307-99 (2003). "Standard Method of Test for Determining the Resilient Modulus of Soils and Aggregate Materials." *American Association of State Highways and Transportation Office*.
54. Hibbitt, K., and Hibbitt, S. (2004). *ABAQUS Standard User's Manuals*, Version 6.5, Pawtucket, RI.
55. SAS Institute Inc. SAS OnlineDoc® 9.1.2. Cary, NC, SAS Institute, Inc., 2004.
56. McGown, A.; Yeo, K.C.; and Yogarajah, I. (1990). "Identification of a Dynamic Interlock Mechanism." Performance of Reinforced Soil Structures," *Proc., International Reinforced Soil Conference*, Glasgow, pp. 377-379.

57. Perkins, S.W.; Ismeik, M.; and Fogelsong, M.L.; (1999), "Influence of Geosynthetic Placement Position on the Performance of Reinforced Flexible Pavement Systems," Proceedings of the Conference Geosynthetics '99, Boston, MA, Vol. 1, pp. 253-264.

58. Konietzky, H., Kamp, L., Groeger, T., and Jenner, C. (2004). "Use of DEM to Model the Interlocking Effect of Geogrids Under Static and Cyclic Loading." *In Numerical Modelling in Micromechanics via Particle methods*, Balkema, Rotterdam, pp. 3-11.

59. McGown, A.; Andrawes, K.Z.; Pradhan, S.; and Khan, A.J. (1998). "Limit State Design of Geosynthetic Reinforced Soil Structures, *Proceedings of 6th International Conference on Geosynthetics*, Atlanta, Vol. 1, pp.143-179.

60. Mcdowell, G.R.; Harireche, O.; Konietzky, H.; Brown, S.; and Thom, N. (2006). "Discrete Element Modeling of Geogrid-reinforced Aggregates". *Proceedings of the Institution of Civil Engineers. Geotechnical Engineering*, 159, pp. 35-48.

61. Werkmeister, S.; Dawson, A.; and Wellner, F. (2001). Permanent Deformation Behavior of Granular Materials and the Shakedown Concept. Transportation Research Board, 80th Annual Meeting, Washington D.C. January 7-11.

62. Manzari, M.T., and Dafalias, Y.F. (1997). A Critical State Two-surface Plasticity Model for Sands. *Geotechnique,* Vol. 47, No. 2, pp. 255-272.

APPENDIX A: NUMERICAL MODELS

Model Geometry

The analysis in this study was conducted using two-dimensional (2D) axisymmetric finite element numerical models. The numerical models included a conventional flexible pavement section consisting of three layers: asphalt concrete layer (AC), base course aggregate layer, and subgrade layer.

A typical finite element mesh that was used in the analysis is shown in Figure 76. The axi-symmetric mesh has a radius of 4500 mm and total depth of 4000 mm. The radius of the mesh was selected based on the distance at which the vertical and horizontal strains became insignificantly small in all layers. However, the depth of the mesh was chosen to be at the depth at which the maximum induced vertical stress in the subgrade became insignificantly small (< 0.01 percent of the applied tire pressure).

Conventional kinematic boundary conditions were adopted, such that the horizontal movement along the left and right boundaries and the vertical movement along the bottom boundary were restrained by using roller supports. Such boundary conditions have been successfully used by Zaghloul and White (1993) and Kuo et al. (1995).

Eight-noded biquadratic axisymmetric quadrilateral elements were used for the subgrade, base, and asphalt concrete layers, while a three-noded quadratic axisymmetric membrane element with thickness of 1 mm was used for the geogrid reinforcement.

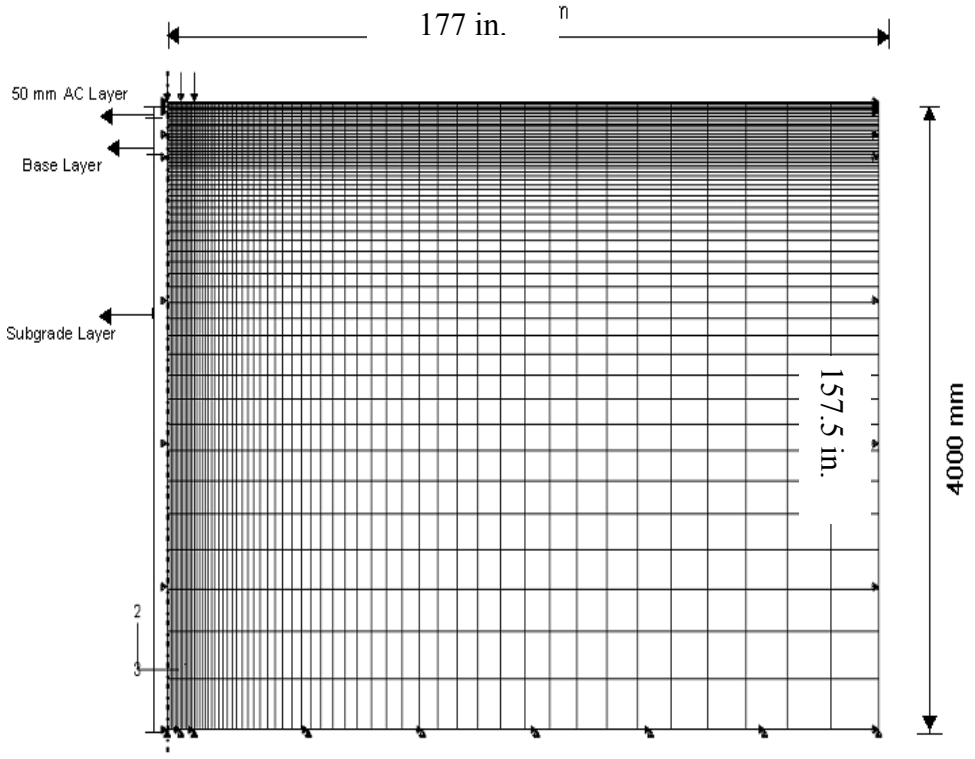

Figure 76
Mesh used in finite element analysis

To determine the suitable element size for the 2D axisymmetric model, a series of finite element analyses were performed with decreasing element sizes. Mesh sensitivity was studied to determine the level of fine mesh needed for a stable finite element analysis. Based on this analysis, approximately 360, 1180, and 2480 elements were used for the AC, base course, and subgrade layer, respectively.

Interface Model

Full bonding was assumed between the different pavement layers. This assumption is acceptable for the case of a paved system where the allowed surface rutting of such a system surface is small and the slippage is not likely to occur unless excessive rutting takes place (Barksdale and Itani, 1989; Espinoza, 1994).

The geogrid was assumed to have full interlocking with materials surrounding it. However, the full interlocking interface model was compared to other interface models used in previous studies as will be discussed later in this chapter.

Load Model

The loading model in this study included applying gravity loads in the first load step of the analysis then applying 100 cycles of a loading representative of a 80 kN (18 kips) single axle wheel loading, which is the standard load known as equivalent single axle load (ESAL) recommended by AASHTO (1993). The wheel load was simulated by applying the contact pressure on a circular area with a radius of 152 cm (6 in.) at the surface. To account for compaction induced loads and to suppress the initial stage of permanent deformation, the first four cycles were assumed to simulate the compaction stage; therefore, their results were not considered in the analysis.

Material Constitutive Models

Asphalt Concrete (AC) Layer

Initially, a simple linearly elastic model was selected. However, after the initial use of this material model in the finite element model, it was observed that the rebound of this elastic layer after the applied load was returned to zero vertical tensile stresses on the top of the base layer. For this reason, the model was extended to include a plasticity component. The plasticity was introduced by a specification of an ultimate yield stress corresponding to a perfect plasticity hardening law. The parameters used for the AC layer is presented in Table 21.

Base Course Layer

The Drucker-Prager model with isotropic hardening was used to represent the constitutive behavior of crushed limestone I. The Drucker-Prager plasticity model is an isotropic elasto-plastic model that has been used in many studies in literature to represent the behavior of granular base course aggregates and cohesive subgrade soils. The model is written in terms of all three stress invariants. It provides for a possibly noncircular yield surface in the deviatoric plane to match different yield values in triaxial tension and compression, and is associated inelastic flow in the deviatoric plane and separate dilation and friction angles. The linear Drucker-Prager model given as follows:

$$F = J - p\tan(\beta) - d = 0 \tag{17}$$

$$J = \frac{1}{2} q_m \left[1 + \frac{1}{K} - \left(1 - \frac{1}{K} \right) \left(\frac{r}{q_m} \right)^3 \right] \tag{18}$$

where, p= mean effective stress, q_m = the Mises equivalent stress, β = the slope of the linear yield surface in the p-t stress plane and is commonly referred to as the friction angle of the material, r= the third invariant of deviatoric stress, d= the cohesion of the material, and K= the ratio of the yield stress in triaxial tension to the yield stress in triaxial compression and, thus, controls the dependence of the yield surface on the value of the intermediate principal stress.

The Drucker-Prager model parameters were calibrated using drained triaxial tests conducted on crushed limestone I material at its standard Proctor optimum conditions. The summary of those parameters are presented in Table 21. Figure 77 compares the stress-strain behavior predicted using the extended Drucker-Prager model and those measured in the triaxial tests. It is noticed that for the crushed limestone I, the model prediction matched the experimental test results closely.

The constitutive behavior of crushed limestone II was represented using the two surface critical state model. The model formulation proposed by Manzari and Dafalias (1997) combines the concept of bounding surface, where a plastic modulus is determined from the distance between the stress state and an image stress state on the bounding surface and incorporates the influence of the state parameter $\psi = e - e_c$ on the volumetric response. The bounding surface formulation takes place in a deviatoric stress-ratio space and the parameter ψ is used to define the volumetric response of cohesionless soils. A distinct feature of the model is its capabilities to describe hardening and softening response based on its state and drainage condition. Moreover, using a single set of model parameters the model captures the response of granular materials with different void ratios and confining pressures. A schematic representation of the two-surface model in the n-plane is shown in Figure 78. The yield surface function for this model can be expressed as follows:

$$f(\sigma, \alpha, m) = [r_{ij} : r_{ij})]^{1/2} - \sqrt{3/2}\, mp = 0 \tag{19}$$

$$r_{ij} = (s_{ij} - p\alpha_{ij}) \tag{20}$$

where, s_{ij} is the deviatoric stress tensor; α_{ij} is the deviatoric back-stress ratio tensor that describes the kinematic hardening of the yield surface, which indicates the location of the center of the yield surface; and m is the size of the yield surface, that describes the isotropic evolution of the yield surface.

The model has isotropic and kinematic hardening rules. The evolution equation for the size (m), which represents the isotropic hardening rule, is given as:

$$\dot{m} = C_m(1+e_o)\cdot\dot{\varepsilon}_v^p \tag{21}$$

$$\Rightarrow \dot{m} = \Delta\lambda\cdot C_m(1+e_o)\cdot D \tag{22}$$

where, C_m is a model parameter; e_o is the initial void ratio; $\dot{\varepsilon}_v^p$ is the volumetric plastic strain rate; and D is the dilatancy coefficient.

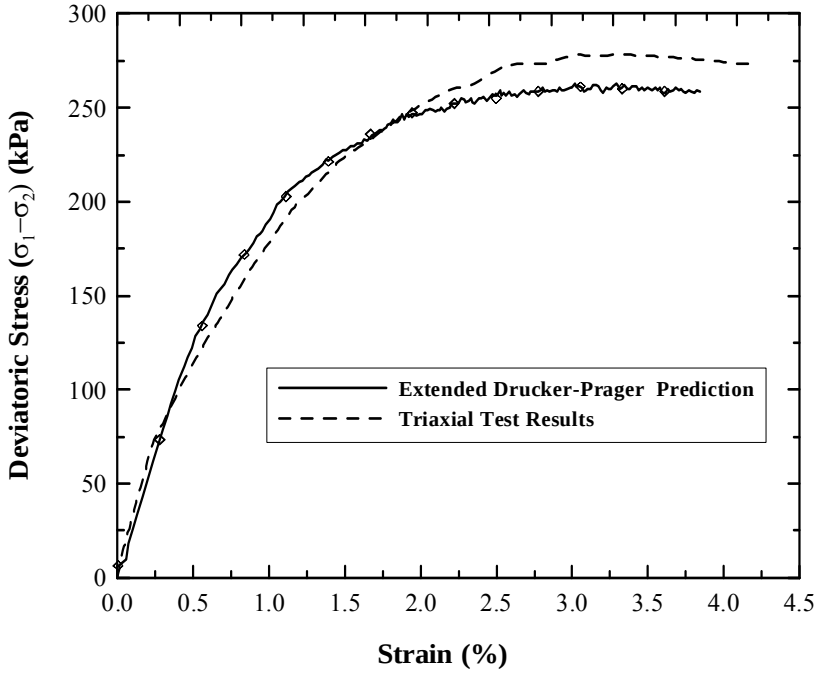

Figure 77
Extended Drucker-Prager prediction of crushed limestone I behavior

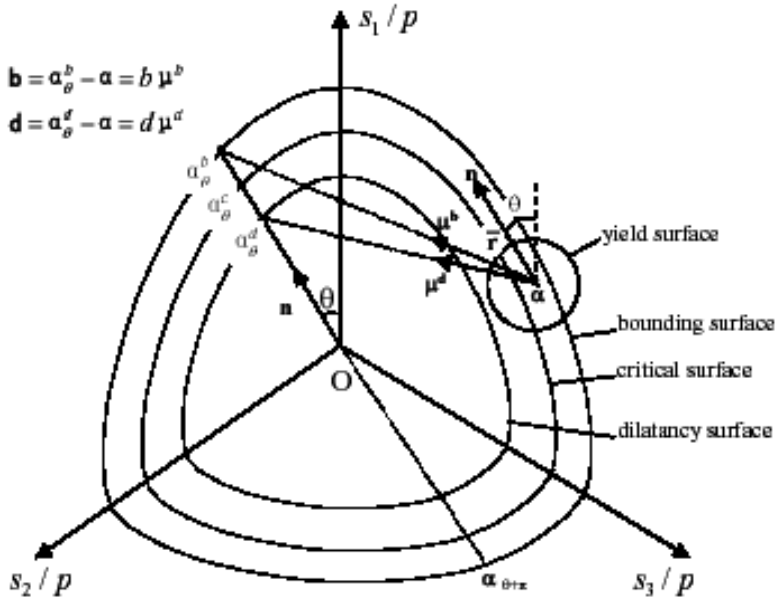

Figure 78
Illustration of yield, bounding, critical, and dilatancy surfaces (Manzari and Dafalias, 1997)

Table 21
AC, base, subgrade, and geogrid material parameters

Material	Friction Angle	Cohesion (psi)	Elastic Modulus (psi)	ν	CBR	Yield Stress (psi)
AC	—	—	500250	0.35	—	112
Crushed Limestone I Base	48	3.8	6525	0.35	—	—
Weak Subgrade	6	1.45	1015	0.35	1.5	—
Moderate	14	2.9	2175	0.35	6	—
Stiff Subgrade	28	3.2	5075	0.35	13	—
Geogrid Type I	—	—	19575	0.25	—	—
Geogrid Type II	—	—	22910	0.25	—	—
Geogrid Type III	—	—	36975	0.25	—	—
Geogrid Type IV	—	—	40600	0.25	—	—

The kinematic hardening rule is chosen to be similar to the non-linear kinematic rule by Armstrong and Fredrick (1966) with the added advantage of function h. The function h is

chosen based on the original proposition by Dafalias and Popov (1976) for two-surface models.

$$\dot{\alpha}_{ij} = \sqrt{3/2} \cdot h \left[\sqrt{(2/3)} \cdot \alpha_\theta^b \cdot \dot{e}_{ij}^{\,p} - \dot{\bar{e}}^{\,p} \cdot \alpha_{ij} \right] \tag{23}$$

$$\dot{\bar{e}}^{\,p} = \left[(2/3) \dot{e}_{ij}^{\,p} : \dot{e}_{ij}^{\,p} \right]^{1/2} \tag{24}$$

$$\dot{e}^{p} = \Delta\lambda \, . n_{ij} \tag{25}$$

A set of 21 parameters is required to completely define the elasto-plastic two-surface critical state model. These parameters can be grouped into four categories:

1. Elastic parameters: The elastic parameters include the Bulk modulus (K_0), Poisson's ratio (ν), and b parameter that define the non-linear elastic behavior. These parameters are, in general, independent of the applied stress path. Since the elastic parameters must be determined from a purely elastic response, they are obtained from small strain triaxial tests.

2. Critical state parameters: Parameters in this category define the critical state of a soil. They are M_c, M_e, λ, $e_{c,ref}$, and p_{ref} . M_c, M_e represent the slope of the critical state lines in compression and extension in q − p space, respectively. These parameters can be related to friction angle (ϕ`) using and the following equations:

$$M_C = \frac{6\sin(\phi`)}{3-\sin(\phi`)} \tag{26}$$

$$M_e = \frac{6\sin(\phi`)}{3+\sin(\phi`)} \tag{27}$$

   The critical state in *e* versus ln (p) space is defined in terms of λ, $e_{c,ref}$, and p_{ref}. λ represents the slope of the critical state line; $e_{c,ref}$ and p_{ref} represent a reference point in this line. These parameters are considered to be constants for a given soil regardless of initial stress state and loading condition.

3. Model specific parameters: This category includes parameters that are specific for the two-surface elastoplastic model. These are:
   a. bounding and dilatancy (phase transformation) surface parameters, k^b_c, k^b_e, k^d_c, and k^d_e
   b. initial yield surface parameter, m

c. hardening parameters, c_m and h_0
d. dilatancy parameter, A_0
e. fabric tensor parameters, F_{max} and C_f

4. Suction parameters: this category includes three parameters needed to normalize the unsaturated behavior of the base course material.

The aforementioned parameters were calibrated for the crushed limestone II material by examining results from drained or undrained triaxial tests. Table 22 presents a summary of the calibrated model parameters used in the finite element analysis. Figure 79 compares the results obtained from triaxial tests conducted on crushed limestone II material to those predicted using the two surface critical surface model. It can be seen that the model predictions were in good agreement with the experimental results.

Table 22
Two surface model parameter for crushed limestone II base material

Elastic Parameters	
K_0	15 ksi
ν	0.3
b	0.72
Critical state Parameters	
M_c/M_e	1.91/1.14
λ	0.0165
$e_{cs,ref}$, pref	0.52, 21 kPa
Model Parameters	
$k^b c/k^b e$	4.5/1.74
$k^d c /k^d e$	2.3/0.72
h_0	800
c_m	0.01
m	0.19
A_0	0.36
F_{max}	100
C_f	100
Suction Parameters	
n_1	0.0263
n_2	1.975
n_3	2.363

Subgrade Layer

The subgrade was modeled using the Drucker-Prager model in the finite element analysis that was conducted using the crushed limestone I as a base material. In this analysis, three sets of the Drucker-Prager model parameters were selected for subgrade materials from previous work to represent weak, moderate, and stiff subgrades. The selected parameters are also presented in Table 21. While in the finite element analysis that was conducted using crushed limestone II, the subgrade was modeled using a modified Cam Clay model. The yield function of the modified Cam Clay model corresponding to a particular value p_c of the consolidation pressure has the form shown in equation (28). Three sets of the modified Cam Clay model parameters were selected to describe the behavior of subgrade materials from previous work to represent weak, moderate, and stiff subgrades. The selected parameters are presented in Table 23.

$$f = q^2 - M_c^2 p (pc - p) = 0 \tag{28}$$

Table 23
Modified Cam Clay model parameter for different subgrade soils

Subgrade	G (kPa)	M	λ	κ	e_0	CBR
Soft	750	0.65	0.225	0.11	1.35	1.5
Medium	2900	1	0.11	0.084	0.95	7
Stiff	5075	1.56	0.022	0.005	0.54	15

Geogrid Layer

A linear elastic model was used for the behavior of geogrid material. Such a model proved to be efficient when used by other researchers (e.g., Dondi, 1994; Ling and Liu, 2003; and Perkins, 2001), especially since the induced strain in the geogrid is very small and is considered within the elastic range. Four geogrid types with different equivalent elastic moduli were used. A summary of the properties of the geogrid types investigated in this study are shown in Table 21.

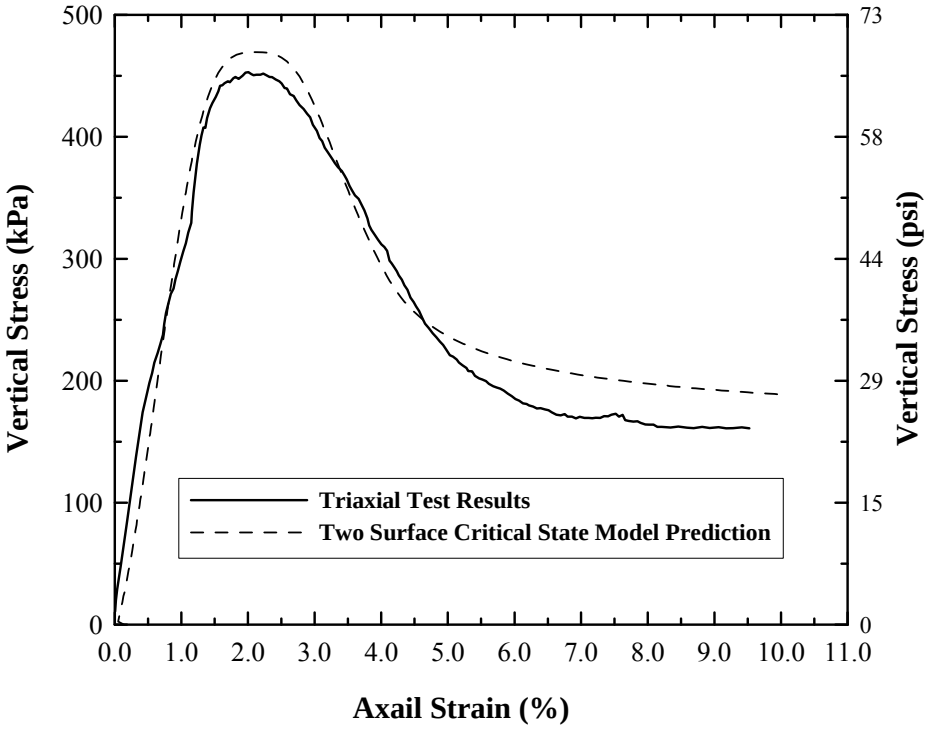

Figure 79
Verification of two surface critical state model using monotonic triaxial

APPENDIX B: TEST RESULTS

Results of Drained Triaxial Tests

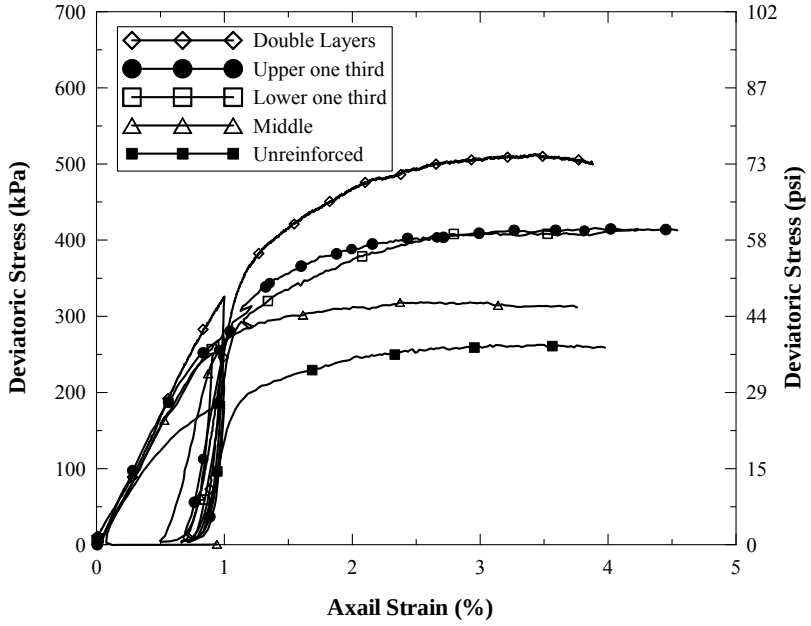

Figure 80
Stress-strain curves for crushed limestone I samples reinforced with geogrid Type II

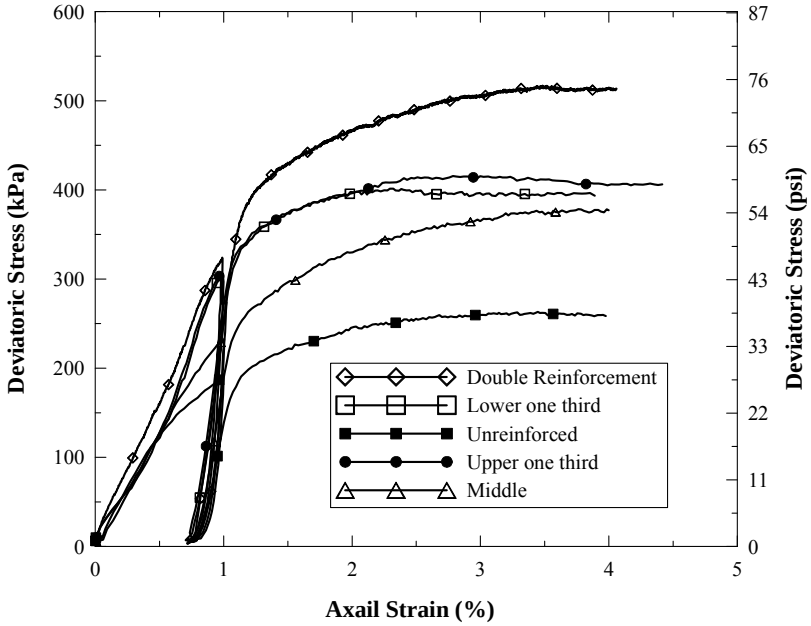

Figure 81

Stress-strain curves for crushed limestone I samples reinforced with geogrid Type III

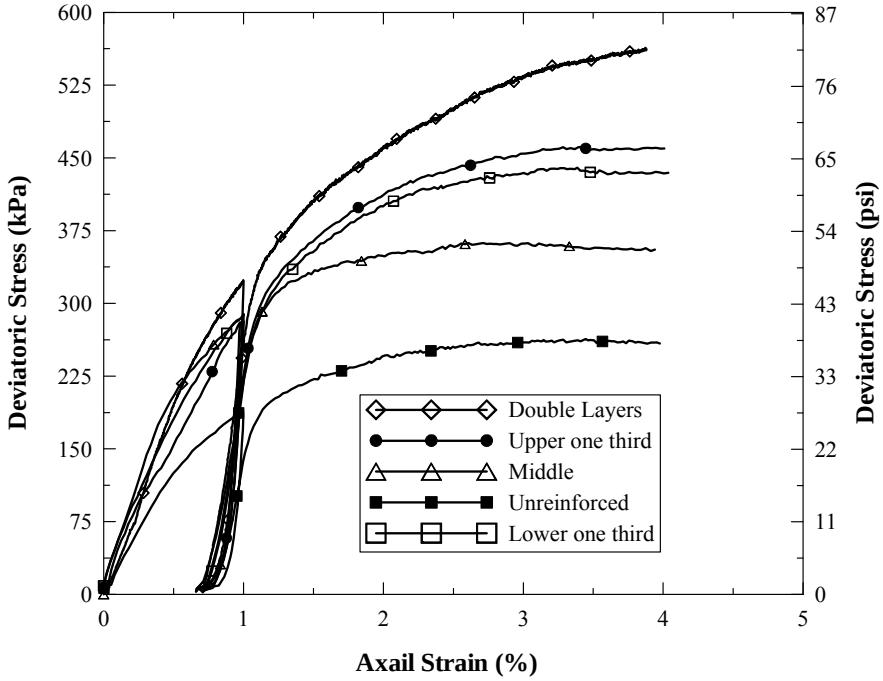

Figure 82
Stress-strain curves for crushed limestone I samples reinforced with geogrid Type IV

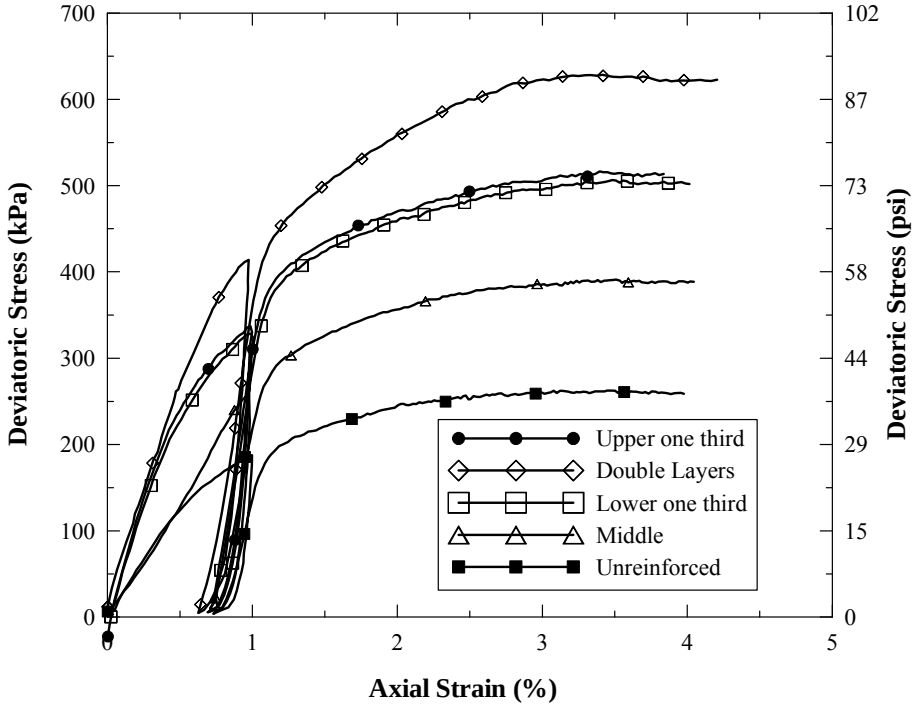

Figure 83
Stress-strain curves for crushed limestone I samples reinforced with geogrid Type V

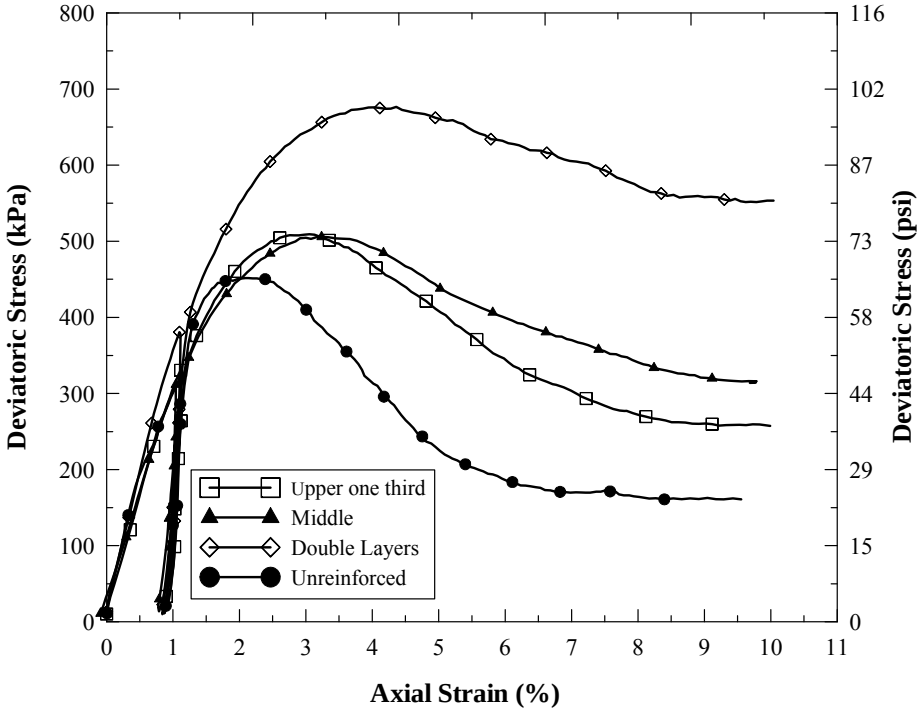

Figure 84
Stress-strain curve for crushed limestone II samples reinforced with geogrid Type IV

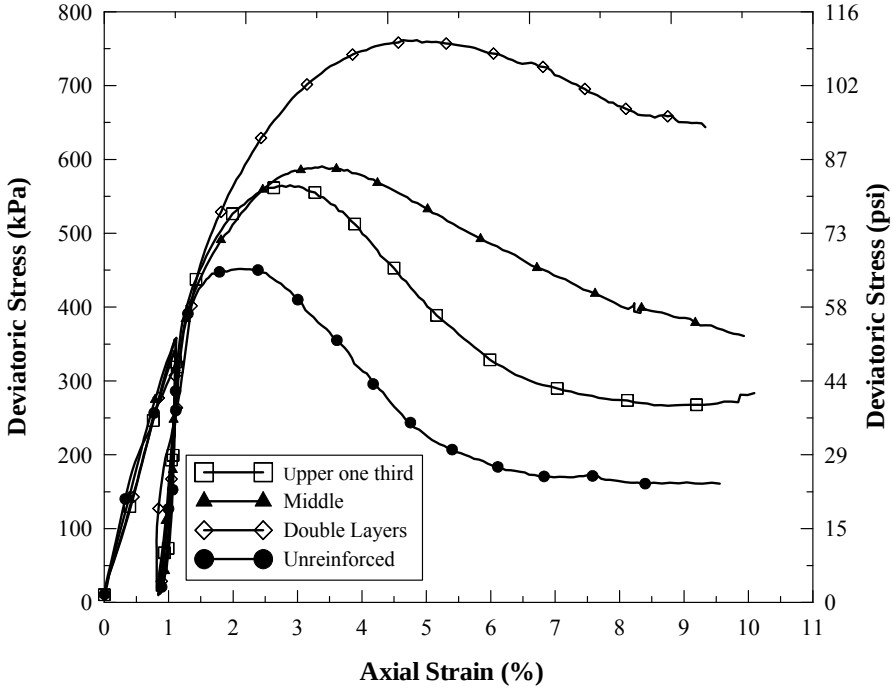

Figure 85
Stress-strain curve for crushed limestone II samples reinforced with geogrid Type V

Results of Permanent Deformation Tests

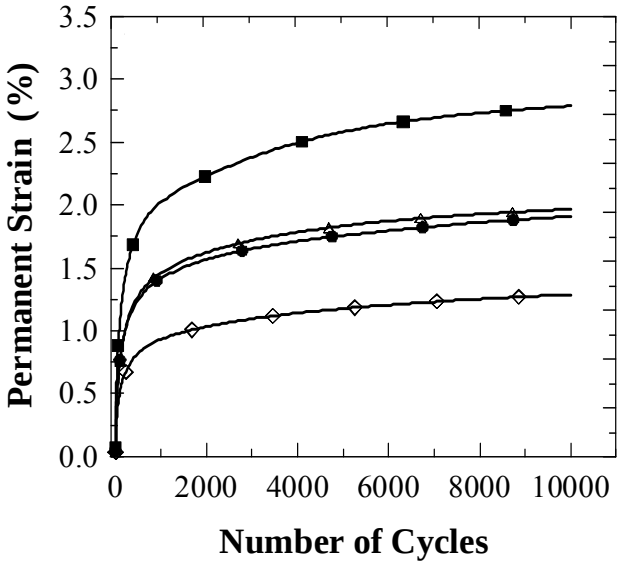

Figure 86
Permanent deformation curves for crushed limestone I samples reinforced with geogrid Type IV

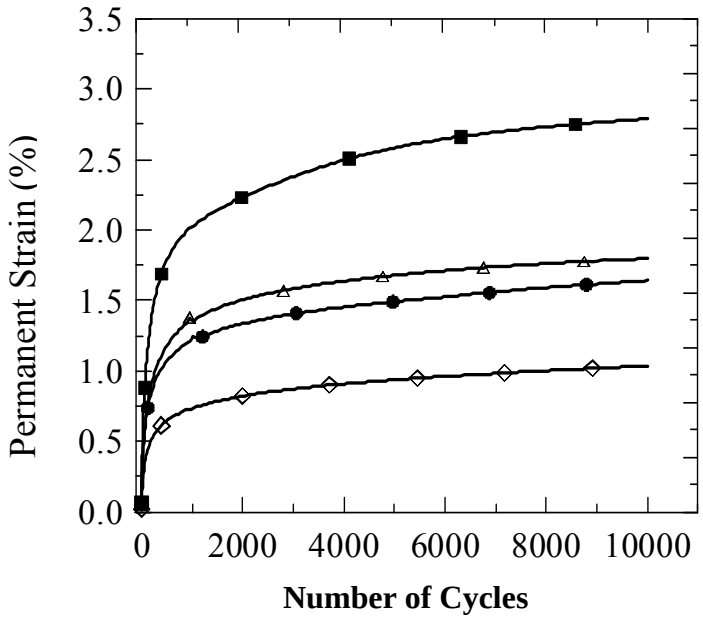

Figure 87
Permanent deformation curves for crushed limestone I samples reinforced with geogrid Type V

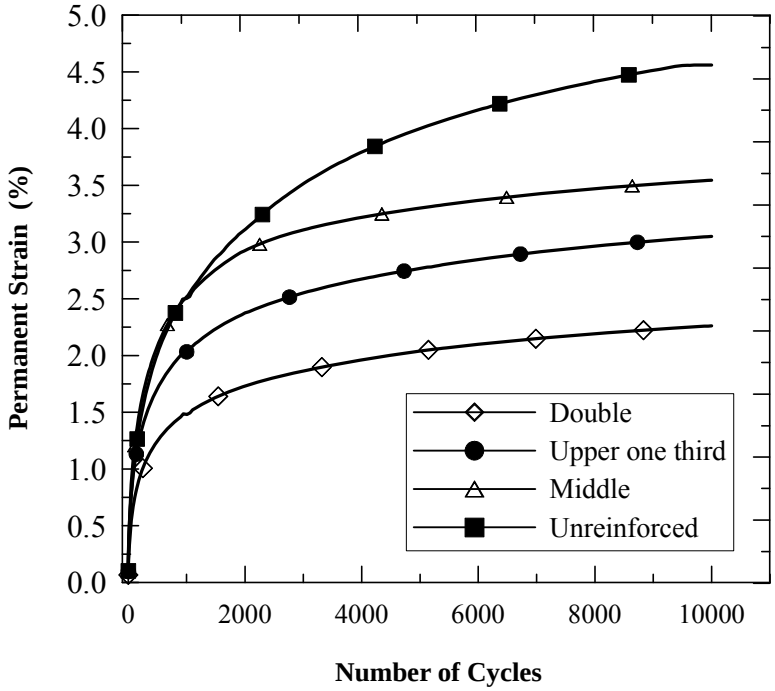

Figure 88
Permanent deformation curves for crushed limestone II samples reinforced with geogrid Type IV

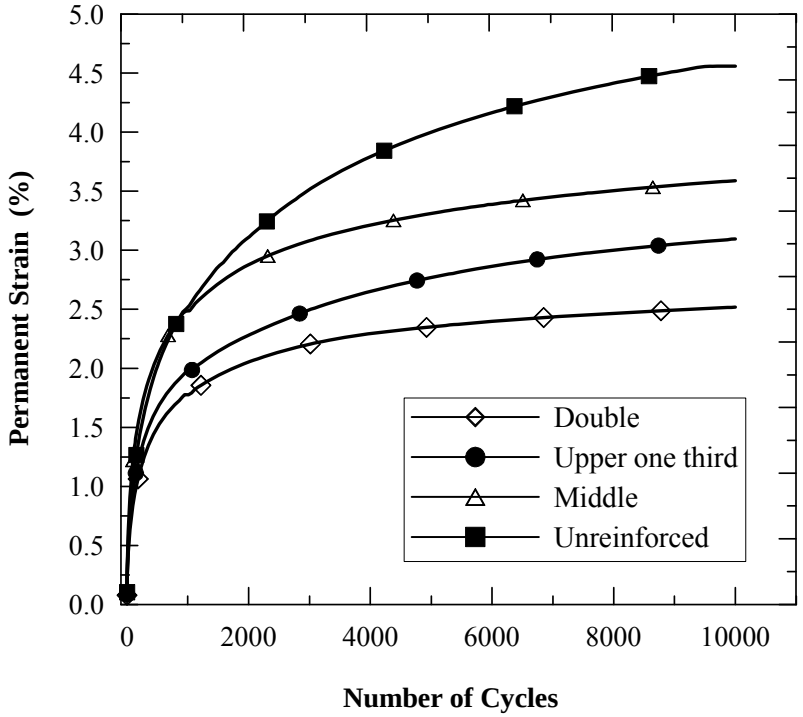

Figure 89
Permanent deformation curves for crushed limestone II samples reinforced with geogrid Type V